

## REPORT DOCUMENTATION PAGE

Form Approved  
OMB No. 0704-0188

2

Public reporting burden of this collection of information is estimated to average 1 hour per response, including the time for reviewing instructions, searching existing data sources, gathering and maintaining the data needed, and reviewing the collection of information. Send comments regarding this burden estimate or any other aspect of this collection of information, including suggestions for reducing the burden, to Washington Headquarters Services, Directorate for Information Operations and Reports, 1215 Jefferson Davis Highway, Suite 1204, Arlington, VA 22202-4302, and to the Office of Management and Budget, Paperwork Project, Washington, DC 20503.

AGENCY USE ONLY (Leave Blank)

2. REPORT DATE

27 July 1990

3. REPORT TYPE AND DATES COVERED

PhD Thesis Jun86-Jul90 final

TITLE AND SUBTITLE

Experimental Observations of Microwave Emission from  
a 35 GHz Cyclotron Autoresonant Maser

5. FUNDING NUMBERS

na

AUTHOR(S)

Anthony C. DiRienzo

PERFORMING ORGANIZATION NAME(S) AND ADDRESS(ES)

US Army  
Student Detachment  
Fort Ben Harrison, IN 462168. PERFORMING ORGANIZATION  
REPORT NUMBER

na

9. SPONSORING/MONITORING AGENCY NAME(S) AND ADDRESS(ES)

US Army  
Student Detachment  
Ft. Ben Harrison, IN 4621610. SPONSORING/MONITORING AGENCY  
REPORT NUMBER

na

11. SUPPLEMENTARY NOTES

12a. DISTRIBUTION/AVAILABILITY STATEMENT

See DoDD 5230.24 "Distribution Statements on Technical  
Documents"**DISTRIBUTION STATEMENT A**

Approved for public release

Distribution Unlimited

12b. DISTRIBUTION CODE

13. ABSTRACT (Maximum 200 words)

Measurements of microwave emission from a 35 GHz cyclotron autoresonance maser single-pass amplifier are reported. The maser operates in an axial magnetic field of 6 kilogauss and uses a mildly relativistic electron beam (1.5 MeV, 130 A) of 30 ns duration. Electrons are imparted perpendicular velocity by means of a bifilar helical wiggler. Peak power from the CARM is 12.2 MW, which corresponds to an efficiency of 6.3% with a linear growth rate of 50 dB/m. The experiment operates in the fundamental TE<sub>11</sub> mode of a circular waveguide. During amplifier operation a 17 kW signal is injected from a 35 GHz magnetron. When the CARM is operated as a superradiant amplifier (amplification of background noise), evidence of multimoding is observed. Numerical simulations that utilize the results of beam dynamics calculations as input into the CARM simulations are in good agreement with experimental results.

14. SUBJECT TERMS

High Power Microwaves, Cyclotron Maser, Cyclotron Autoresonance  
Maser

15. NUMBER OF PAGES

134

16. PRICE CODE

17. SECURITY CLASSIFICATION  
OF REPORT  
unclassified18. SECURITY CLASSIFICATION  
OF THIS PAGE  
unclassified19. SECURITY CLASSIFICATION  
OF ABSTRACT  
unclassified20. LIMITATION OF ABSTRACT  
UL

AD-A225 206

**EXPERIMENTAL OBSERVATIONS OF MICROWAVE  
EMISSION FROM A 35 GHZ CYCLOTRON  
AUTORESONANCE MASER**

by

**Anthony C. DiRienzo**

B.S., United States Military Academy, 1972  
S.M., Massachusetts Institute of Technology, 1980  
M.A., Georgetown University, 1985

Submitted to the Department of Physics  
in partial fulfillment of the requirements for the degree of

**Doctor of Philosophy**

at the

**MASSACHUSETTS INSTITUTE OF TECHNOLOGY**

**July 1990**

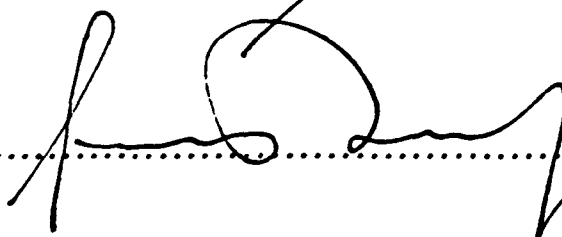
© Massachusetts Institute of Technology 1990

Signature of Author .....



Department of Physics  
July 27, 1990

Certified by .....



George Bekefi  
Professor of Physics  
Thesis Supervisor

Accepted by .....

George F. Koster  
Chairman, Departmental Graduate Committee

# EXPERIMENTAL OBSERVATIONS OF MICROWAVE EMISSION FROM A 35 GHZ CYCLOTRON AUTORESONANCE MASER

by

Anthony C. DiRienzo

Submitted to the Department of Physics  
on July 27, 1990, in partial fulfillment of the  
requirements for the degree of  
Doctor of Philosophy

## Abstract

Measurements of microwave emission from a 35 GHz cyclotron autoresonance maser single-pass amplifier are reported. The maser operates in an axial magnetic field of  $\sim 6$  kG and uses a mildly relativistic electron beam (1.5 MeV, 130 A) of 30 ns duration. Electrons are imparted with perpendicular velocity by means of a bifilar helical wiggler. Peak power from the CARM is 12.2 MW, which corresponds to an efficiency of 6.3% with a linear growth rate of 50 dB/m. The experiment operates in the fundamental  $TE_{11}$  mode of a circular waveguide. During amplifier operation a 17 kW signal is injected from a 35 GHz magnetron. When the CARM is operated as a superradiant amplifier (amplification of background noise), evidence of multimoding is observed. Numerical simulations that utilize the results of beam dynamics calculations as input into the CARM simulations are in good agreement with experimental results.

**KEYWORDS:** High Power Microwaves, Cyclotron Maser, Cyclotron Autoresonance Maser

Thesis Supervisor: George Bekefi  
Title: Professor of Physics



Accession	
NTIS	DTIC
DTIC	DTIC
DTIC	DTIC
By <i>Per form 50</i>	
Date	
Dist	
<i>A-1</i>	

## Acknowledgements

I would like to thank Professor George Bekefi, my advisor, for his guidance and thoughtfulness. I consider myself most fortunate to have been his student for these several years. His wealth of knowledge and vast experience has shown to me the great benefit of a lifelong diligence and enjoyment in the study of physics. He is firm when necessary, always friendly, and concerned foremost for the welfare of his students. His ability to immediately see to the core of a particular problem, then direct the solution to the problem in a manner that gives satisfaction to all, is the key to his success. It has been an honor to be his student.

Ivan Mastovsky deserves special thanks. Without his technical expertise, very little would be accomplished in the laboratory. His experience in the workings of the most minutest part of the experimental apparatus, coupled with his unhesitating willingness to help, is a primary cause of any successful experiment in our group. I have been most fortunate to have worked these years with Ivan and consider him my friend as well.

Several members of the research group have assisted in this experiment. Chaim Leibovitch worked for nearly a year on the initial setup and calibration of the experiment and contributed to the first reporting of a CARM amplifier. Manoel Conde assisted in the taking of data. Eric Grossbeck spent countless hours running simulations of both the beam dynamics and the CARM interaction and significantly contributed to the understanding of the CARM. He also assisted in the taking of the final experimental data.

I would like to especially thank Dr. Chiping Chen for his formulation of the numerical simulations of the CARM interaction. He has taken the simulation process one step closer to a true model of a very complex problem. He has also willingly spent long hours insuring my understanding of the simulations that he has formulated.

Toni Fischer has made my stay at MIT most interesting. Our discussions on anything but physics (i.e. politics) often were the high point of the day. A thanks for the support and assistance of the other members of the research group: Professor Jonathan Wurtele, Rick Stoner, Dr. Eli Jerby, Ed Fitzgerald, John Weigel, Bruce Danly, Ken Pendergast and many others.

It is important to thank the United States Army for its farsightedness in the support that it grants to those officers in doctoral programs. Hopefully the Army will long reap the benefits of this program.

Lastly, it goes without saying that none of this would have been accomplished without the love and support of my wife and partner, Lauren. More important than proofreading was her unending encouragement for me in this effort. I am indebted to her most of all.

# Contents

<b>1</b>	<b>Introduction</b>	<b>10</b>
<b>2</b>	<b>Experimental Apparatus</b>	<b>22</b>
2.1	Introduction . . . . .	22
2.2	Detailed Description of the Apparatus . . . . .	24
2.2.1	The Marx Accelerator . . . . .	24
2.2.2	The Diode . . . . .	27
2.2.3	The Solenoid System . . . . .	35
2.2.4	The Microwave Input and Detection System . . . . .	40
2.2.5	The Wiggler Magnet . . . . .	49
2.2.6	The Electron Beam Current Monitors . . . . .	58
<b>3</b>	<b>Beam Transport</b>	<b>61</b>
3.1	Introduction and Outline . . . . .	61
3.2	Ideal Electron Trajectories - One Dimensional Model . . . . .	62
3.3	Realistic Electron Trajectories - Three Dimensional Model . . . . .	66
3.3.1	Off Axis Trajectory Effects . . . . .	67
3.3.2	Effects of Wiggler Termination . . . . .	69
3.3.3	Effect of Space Charge on the Beam . . . . .	69
3.4	Numerical Simulations . . . . .	71
3.4.1	Group I Orbit Simulations . . . . .	71

3.4.2	Group II Orbit Simulations . . . . .	77
3.5	Conclusion . . . . .	80
<b>4</b>	<b>Cyclotron Autoresonance Maser Theory</b>	<b>85</b>
4.1	Introduction and Outline . . . . .	85
4.2	The Linear Characteristics of the CARM Interaction . . . . .	86
4.2.1	Pinch Point Analysis . . . . .	90
4.3	Numerical Simulations . . . . .	91
4.3.1	Simulation Results . . . . .	95
4.4	Conclusions . . . . .	105
<b>5</b>	<b>Experimental Results</b>	<b>107</b>
5.1	Introduction . . . . .	107
5.2	The CARM Interaction Utilizing the Group I Orbits . . . . .	109
5.3	The CARM Interaction Utilizing Group II Orbits . . . . .	116
<b>6</b>	<b>Conclusion and Summary</b>	<b>125</b>

# List of Figures

1-1	Schematic of the CARM interaction . . . . .	12
1-2	Vector relationships of two orbiting electrons . . . . .	16
2-1	Schematic of the CARM apparatus . . . . .	23
2-2	The Marx accelerator and Blumlein transmission line . . . . .	26
2-3	The diode . . . . .	29
2-4	Phase space plot of the beam as it exits the diode . . . . .	31
2-5	Transmitted current versus $B_z$ and $B_z^2$ . . . . .	33
2-6	Inductive voltage subtraction method . . . . .	36
2-7	Diode voltage and current. . . . .	37
2-8	Axial magnetic field profile . . . . .	39
2-9	Microwave transport and detection system . . . . .	41
2-10	Microwave input coupler . . . . .	42
2-11	The transmitting horn . . . . .	44
2-12	Radiating horn mode patterns . . . . .	46
2-13	Crystal detector calibration curve . . . . .	48
2-14	Band pass filter calibration . . . . .	50
2-15	Wiggler field harmonic content . . . . .	52
2-16	Wiggler field profiles, $\lambda_w=4.06$ cm with $b = .9$ and $2.6$ cm. . . . .	54
2-17	Wiggler magnet schematic and circuit . . . . .	55
2-18	Measured field profile of the $4.06$ cm period wiggler . . . . .	56
2-19	Measured field profile of the $7.00$ cm period wiggler . . . . .	57

2-20	Current viewing probe and typical current signal pulse . . . . .	60
3-1	Electron orbit in an ideal axial and wiggler magnetic field. . . . .	64
3-2	Axial velocity versus axial magnetic field. . . . .	65
3-3	Thermal paper method of determining $\alpha$ . . . . .	68
3-4	$\alpha$ versus wiggler strength for the Group I wiggler. . . . .	72
3-5	Growth of $\alpha$ and energy spread in the group I wiggler . . . . .	74
3-6	Three superimposed beam spots . . . . .	75
3-7	Increased spatial dispersion of the beam as the operating field nears magnetoresonance . . . . .	76
3-8	$\alpha \equiv \beta_{\perp}/\beta_{\parallel}$ versus wiggler strength for the group II wiggler ( $B_z(\text{critical})=5.6$ kG, $\gamma=4$ , and $\lambda_w=7.0$ cm). . . . .	78
3-9	$\alpha \equiv \beta_{\perp}/\beta_{\parallel}$ as a function of $z$ for $B_z=6.1$ kG and $B_w=490$ G for the group II wiggler. . . . .	79
3-10	Three superimposed beam spots for the group II wiggler . . . . .	81
3-11	Growth of $\alpha$ vs $z$ for $B_z=5.8$ kG and $B_w=490$ G, group II wiggler. .	82
3-12	Three spot representation for $B_z=5.8$ kG and $B_w=490$ G. . . . .	83
4-1	Geometry of interaction . . . . .	87
4-2	Pinch point analysis . . . . .	92
4-3	Effect of energy spread on the growth rate and efficiency of the CARM. .	96
4-4	Effect of $\alpha$ on the growth rate and efficiency of the CARM. . . . .	98
4-5	Effect of detuning (changing $\Delta$ ) on the efficiency and growth rate of the CARM. . . . .	99
4-6	Gain bandwidth . . . . .	100
4-7	Effect of beam current on efficiency and growth rate of the CARM. .	102
4-8	CARM power as a function of interaction length $z$ . . . . .	103
4-9	$\gamma$ vs $\psi$ for various locations in the interaction region. . . . .	104
4-10	Effect on output power of axial field tapering . . . . .	106



5-1	CARM power as a function of axial magnetic field. . . . .	110
5-2	CARM power as a function of wiggler strength. . . . .	111
5-3	Power as a function of interaction length for group I wiggler orbits .	113
5-4	Superradiant power for the group I orbit CARM. . . . .	114
5-5	Higher order waveguide modes available for coupling to the beam. .	117
5-6	Angle scan of amplifier mode radiation . . . . .	118
5-7	Superradiant mode angular scan . . . . .	119
5-8	Power versus axial magnetic field for the group II CARM. . . . .	121
5-9	Power versus wiggler strength for the group II CARM. . . . .	122
5-10	Power versus interaction length for the CARM utilizing group II wig- gler orbits . . . . .	123
5-11	Power versus $z$ for group II orbit CARM using a plexiglass window.	124

# List of Tables

2.1	Beam Parameters . . . . .	34
2.2	Characteristics of the Group I and Group II Wiggler . . . . .	58
3.1	Wiggler Field Results . . . . .	84
4.1	Simulation Parameters . . . . .	97
5.1	Experimental Parameters and Results . . . . .	108
5.2	Waveguide Modes and Cutoff Frequencies . . . . .	115
5.3	Coupling Between Available Waveguide Modes . . . . .	115

# Chapter 1

## Introduction

The cyclotron autoresonance maser (CARM) has received considerable interest in recent years as a potential source of high power microwave radiation. This work describes the first successful testing [1,2,3,4,5] of a device that utilizes the CARM interaction to produce microwave radiation at 35 GHz in a single pass amplification of both background noise and an input signal. There are several planned devices at frequencies above and below 35 GHz [6,7] and recently a device operating as an oscillator at 6-20 GHz has been reported [8].

In the late 1970s theoretical work, primarily by Soviet physicists, began to emerge concerning the ability to couple the energy of a relativistic rotating electron beam to an electromagnetic wave [9,10,11,12,13]. This stimulated cyclotron radiation produced significant power in 1981 [11,12] and work on the cyclotron maser interaction began in earnest [14,15,16,17,18,19,20,21,22,23,24,25]. The gyrotron, the cyclotron autoresonance maser (CARM), and the gyro-travelling wave amplifier (gyro-TWA) [26] are devices that rely on the cyclotron motion of the beam. The experiment described in this work involves the CARM interaction in which there is a large component of the beam velocity that is parallel to the wave.

The components of the CARM are an electron beam, a method of imparting a specific amount of perpendicular velocity to the beam and an axial magnetic field

in which the spinning electron beam can rotate at the required cyclotron frequency. The CARM can act as an amplifier of some input wave or of background noise or can be constructed as an oscillator in which some of the radiation produced in the interaction is maintained in the interaction cavity and some is permitted to exit. The experiment described in this work involves the study of a single pass CARM amplifier.

In this experiment, perpendicular velocity is imparted to the electron beam by means of a helical wiggler magnet that produces a magnetic field transverse to the beam axis. This causes the beam to corkscrew about the axis with a specific amount of perpendicular velocity. Having received sufficient perpendicular velocity, the beam exits the wiggler region and is allowed to rotate in the CARM interaction region. Since rotating electrons undergo accelerated motion, and since accelerating electrons radiate, the frequency of the radiation emitted by the electrons in the CARM interaction region is a function of the strength of the axial magnetic field there.

The relationship of the electromagnetic wave, the cyclotron motion of the electron beam, and the orientation of the magnetic field are shown schematically in figure 1-1(a). The wave is a right hand circularly polarized wave and the cyclotron motion of the beam is also right-handed.

The CARM interaction in a waveguide is the result of the resonant coupling of the Doppler upshifted beam cyclotron mode with an electromagnetic wave;

$$\omega = \frac{s\Omega_{c0}}{\gamma} + k_{\parallel}v_{\parallel} \quad (1.1)$$

where  $\omega$  is the frequency of the radiation,  $\Omega_{c0} = eB/mc$  is the nonrelativistic cyclotron frequency of the beam in the surrounding magnetic field,  $\gamma = (1 - (\vec{v} \cdot \vec{v}/c)^2)^{-1/2}$  is the relativistic energy factor, and  $s$  is the harmonic number of the beam mode,  $k_{\parallel}$  is the axial wavenumber of the electromagnetic wave and  $v_{\parallel}$  is the component of the beam velocity parallel to the axial magnetic field. In the case of propagation in a waveguide, the dispersion characteristic of the electromagnetic

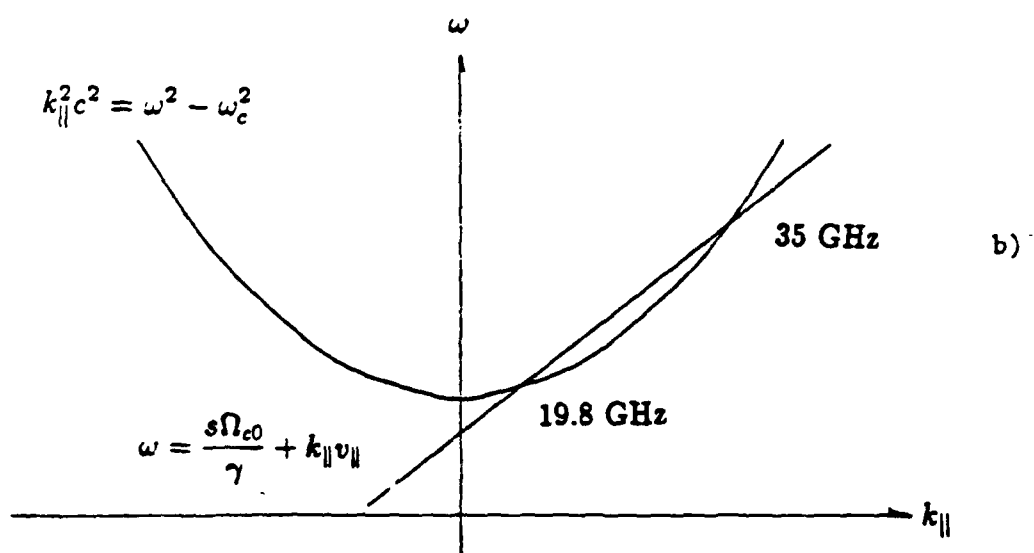
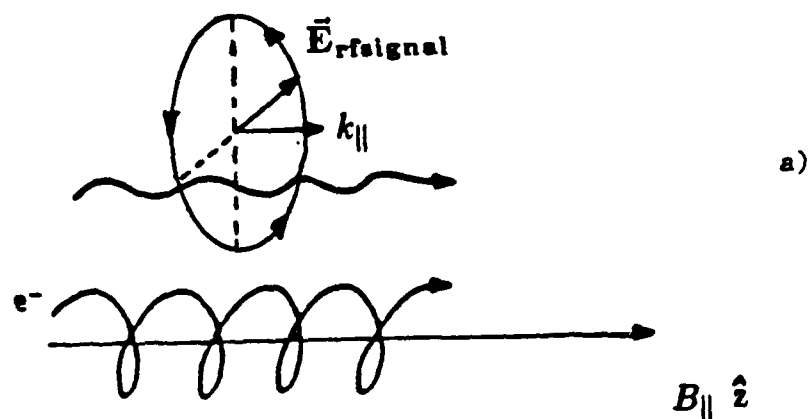


Figure 1-1: (a) Relative directions of the electromagnetic wave, beam and surrounding magnetic field in a CARM device. Both the wave and the beam motion are right-handed. (b) Intersection of waveguide mode and beam cyclotron mode showing the Doppler shifted intersection points.

wave is given by

$$\omega^2 = k_{\parallel}^2 c^2 + \omega_c^2 \quad (1.2)$$

where  $\omega_c$  is the cutoff frequency for the particular mode in the waveguide. This interaction is shown schematically in figure 1-1(b). Note that there are two intersections of the beam mode with the waveguide mode. If the lower intersection were to occur at  $k_{\parallel} \simeq 0$  that interaction would be called the gyrotron interaction. If the beam line were to intersect the waveguide mode tangentially, the interaction would be called a gyro-TWA. If there was an intersection at a negative  $k_{\parallel}$  value, the interaction would be classified as a counterwave oscillator. The intersections shown in figure 1-1(b) are the Doppler upshifted and downshifted modes. Eliminating  $k_{\parallel}$  between equations 1.1 and 1.2 yields the radiation frequency

$$\omega \simeq \Omega_{c0} \frac{\gamma_{\parallel}^2}{\gamma} (1 \pm \beta_{\parallel} [1 - (\frac{\omega_c \gamma}{\Omega_{c0} \gamma_{\parallel}})^2]^{1/2}) \quad (1.3)$$

where the positive sign refers to the sought-after Doppler upshifted frequency. This experiment involves the study of the upshifted mode, which in this case is designed to be 35 GHz.

The benefit obtained from this Doppler upshift is one of the prime motivations for study of the CARM interaction. To reach the same frequency, the gyrotron would have to operate either at a higher harmonic ( $s$ ) or at a higher axial magnetic field ( $B_z$ ) while the CARM can be operated in the fundamental ( $s=1$ ) mode. Operation at fundamental frequencies usually results in higher efficiencies.

Equation 1.1 can be rearranged to obtain the well-known CARM resonance condition

$$\omega = \frac{s\Omega_{c0}}{\gamma(1 - \beta_{\parallel}/\beta_{ph})} \quad (1.4)$$

where  $\beta_{ph} = \omega/c k_{\parallel}$  is the normalized axial phase velocity of the wave. It can be seen from equation 1.4 that as  $\beta_{ph} \rightarrow 1$  there is the possibility of a large Doppler upshift from the relativistic cyclotron frequency. In this work only the fundamental cyclotron mode ( $s=1$ ) will be considered.

As the electrons lose energy to the wave, equation 1.1 shows that the frequency  $\omega$  may well change and that loss of synchronism between the particle motion and the electromagnetic wave may occur. However, under the particular conditions discussed below, the increase in the value of  $s\Omega/\gamma$  can just compensate the decrease in the term  $k_{\parallel}v_{\parallel}$  of equation 1.1. Hence the term autoresonance.

The energy and momentum conservation can be expressed as follows

$$\Delta E = \frac{h\omega}{2\pi} \quad (1.5)$$

$$\Delta \vec{p}_{\parallel} = \frac{h\vec{k}_{\parallel}}{2\pi}. \quad (1.6)$$

The momentum is not conserved in the perpendicular direction due to the presence of the external centripetal force of the axial magnetic field. These two equations can be combined as

$$\frac{dE}{dp_{\parallel}} = \frac{2\pi h\omega}{2\pi h k_{\parallel}} = \frac{\omega}{k_{\parallel}} = v_{ph} = \text{constant} \quad (1.7)$$

where  $v_{ph}$  is the axial phase velocity of the wave. The energy exchange in the above equation can also be expressed in terms of the electron beam parameters as

$$\frac{dE}{dp_{\parallel}} = \frac{d(\gamma m_0 c^2)}{d(\gamma \beta_{\parallel} m_0 c)} = \frac{v_{ph} c}{c} = \beta_{ph} c = \text{constant}. \quad (1.8)$$

Integrating this equation results in

$$\gamma(1 - \beta_{\parallel}\beta_{ph}) = \text{constant}. \quad (1.9)$$

The beam cyclotron mode equation (1.1) can be rewritten as

$$\gamma(1 - \frac{\beta_{\parallel}}{\beta_{ph}}) = \frac{\Omega_{c0}}{\omega} = \text{constant}. \quad (1.10)$$

Equations 1.9 and 1.10 can be satisfied simultaneously only if

$$\beta_{ph} = 1. \quad (1.11)$$

Thus autoresonance can be satisfied only for wave propagation in free space where  $v_{ph} = c$ . In a waveguide, where the experiments described in this work were performed, autoresonance can only be approached but never fully satisfied since here  $\beta_{ph} > 1$ .

In the present experiment, the value of  $\beta_{ph}$  is 1.054. Even if the autoresonance condition is satisfied exactly, the spatial growth rate of the CARM interaction is very small, as will be shown in chapter 4. Therefore, in practical devices, operation away from  $\beta_{ph} = 1$  is usual.

For the CARM interaction to have a net flow of energy from the electron beam to the wave, there must exist a mechanism that encourages more electrons to be in a position of releasing energy to the wave than are extracting energy from the wave. This positioning is commonly called bunching. Bunching can occur in both the azimuthal and axial directions. Numerical simulations that graphically show the electron bunching are presented in chapter 4 (figure 4-9).

The azimuthal bunching mechanism is a two-step process that occurs simultaneously in the actual device. The first step is the action of the electric field vector that bunches the electrons in phase (relative to the rf wave) such that the electrons are no longer uniformly spread about the cyclotron orbit. The second step is the positioning of the bunch of electrons in a phase relative to the electric field vector such that the bunch of electrons lose energy to the wave.

Referring again to equation 1.1, the first step of the azimuthal bunching mechanism can be seen in the terms containing  $\gamma$  and  $v_{||}$ . For two electrons shown in figure 1-2(a) that orbit in the same direction but at different positions about a field line  $B_z \hat{z}$ , it is apparent that the  $\vec{v}_\perp$  for each electron is oppositely oriented. The electric field vector  $\vec{E}$  of the wave rotates at an angular frequency  $\omega$  while the electrons rotate at the relativistic cyclotron frequency  $\Omega_{c0}/\gamma \equiv \Omega_c$ . For the Doppler upshifted mode,  $\omega > \Omega_c$ . The energy equation

$$m_0 c^2 \frac{d\gamma}{dt} = -e \vec{v} \cdot \vec{E} \quad (1.12)$$



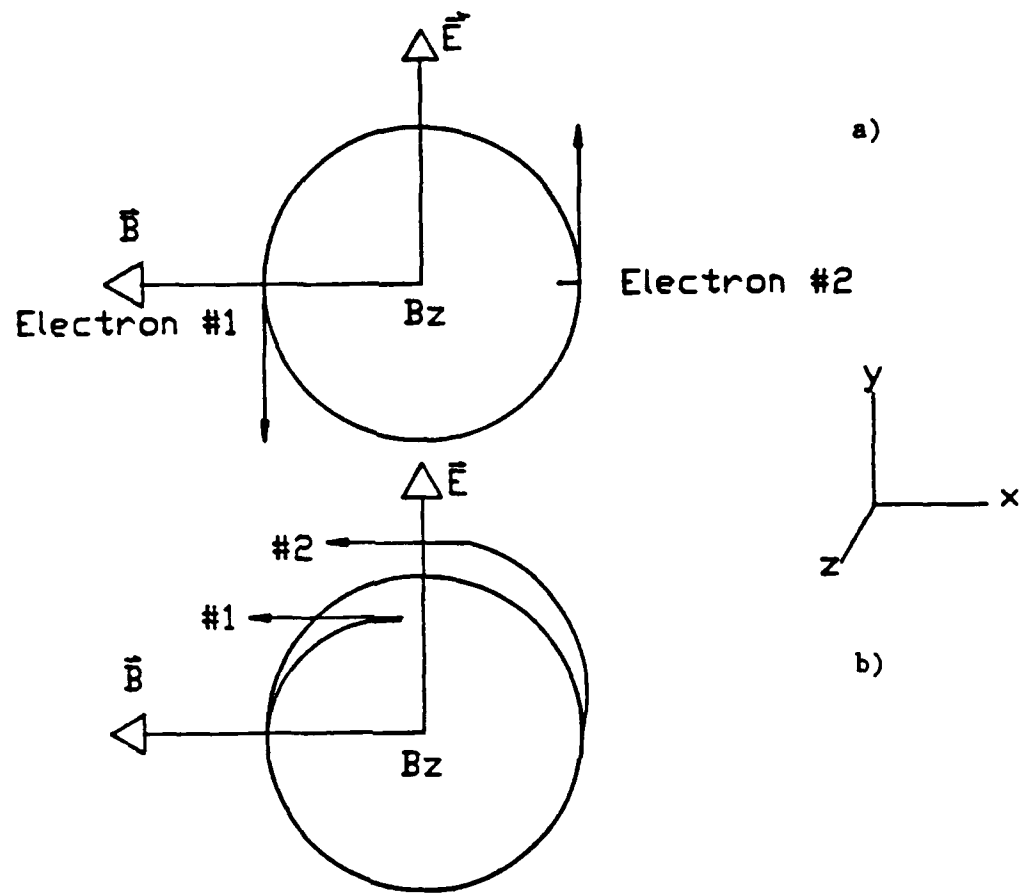


Figure 1-2: Vector relationships of two orbiting electrons. (a) Electrons are uniformly spread (in relation to the electric field vector,  $\vec{E}$ ) over the orbit at the beginning of the interaction. Two electrons are shown. Both  $\vec{v} \cdot \vec{E}$  and  $\vec{v} \times \vec{B}$  are of opposite sign for each. (b) In azimuthal bunching, the electrons tend to drift toward each other at varying Larmor radii.

shows that the  $\vec{v} \cdot \vec{E}$  is of opposite sign for the two electrons. This means that electron #1 gains energy and #2 loses energy. Since  $\Omega_c = \Omega_{c0}/\gamma$ , the electron gaining energy will have a decreasing angular velocity while the electron losing energy will have an increased angular velocity. The two electrons will tend to drift toward each other around the cyclotron orbit in the direction of the electric field vector as shown in figure 1-2(b).

The second step of the azimuthal bunching mechanism is due to the axial field  $B_z$ . There is some value  $B_z(sync)$  that will keep the electron bunch at the proper phase of the  $\vec{E}$  field vector for energy extraction.

Axial bunching is due to the magnetic field  $\vec{B}_\perp$  of the rf wave. The Lorentz force  $-e(\vec{v}_\perp \times \vec{B}_\perp)$  moves the electrons in the  $z$  direction. As seen in figure 1-2(a), electron #1 will move in the positive  $z$  direction and electron #2 will move in the negative  $z$  direction.

The axial and azimuthal bunching take place simultaneously and the mechanism for extracting energy from the beam is shown below [27]. Equation 1.1 can be used to define the Doppler shifted frequency of the electron  $\omega_D$

$$\omega_D = k_{\parallel} v_{\parallel} + \frac{\Omega_{c0}}{\gamma} \quad (1.13)$$

which is the electron gyrofrequency in the frame of the rf wave. Equation 1.1 can also be rewritten to define a mismatch factor  $\delta$

$$\delta = \omega - k_{\parallel} v_{\parallel} - \frac{\Omega_{c0}}{\gamma} \quad (1.14)$$

which indicates how closely the electron is resonant with the wave.

$\omega_D$  can be varied as

$$\Delta\omega_D = k_{\parallel} \Delta v_{\parallel} - \frac{\Omega_{c0}}{\gamma^2} \Delta\gamma. \quad (1.15)$$

This  $\Delta\omega_D$  will be used to show how the gyrofrequency of an electron, two of which are shown in figure 1-2, is changed due to the  $\vec{E}$  and  $\vec{B}$  fields present in the CARM interaction region.

Equation 1.12 determines the change in  $\gamma$  as

$$\Delta\gamma = \frac{-e}{mc^2} \vec{v}_\perp \cdot \vec{E}_\perp \Delta t \quad (1.16)$$

where  $\vec{E}_\perp$  is the electric field vector of the rf wave. The change in axial velocity can be determined by using Faraday's law and the Lorentz force due to the magnetic field  $\vec{B}_\perp$  of the rf wave

$$\frac{d}{dt} \vec{p}_\parallel = \frac{-e}{c} \vec{v}_\perp \times \vec{B}_\perp. \quad (1.17)$$

The change in the axial velocity is

$$\Delta v_\parallel = \frac{-e v_{ph}}{\gamma m c^2} \left[ \frac{c^2}{v_{ph}^2} - \frac{v_\parallel}{v_{ph}} \right] \vec{v}_\perp \cdot \vec{E}_\perp \Delta t. \quad (1.18)$$

The change in the Doppler shifted frequency of the electron can be determined by combining equations 1.16, 1.18, and 1.15 resulting in

$$\Delta\omega_D = \left[ \left( 1 - \frac{v_\parallel}{v_{ph}} \right) - \left( \frac{c^2}{v_{ph}^2} - \frac{v_\parallel}{v_{ph}} \right) \right] \frac{e}{\gamma m c^2} \vec{v}_\perp \cdot \vec{E}_\perp \Delta t. \quad (1.19)$$

The first term in the brackets of equation 1.19 ( $1 - v_\parallel/v_{ph}$ ) is the azimuthal bunching term and the second term ( $c^2/v_{ph}^2 - v_\parallel/v_{ph}$ ) is the axial bunching term. Depending upon the signs of the azimuthal and axial bunching terms, the two mechanisms can either offset or reinforce each other.

Simplifying equation 1.19 results in

$$\Delta\omega_D = \left[ 1 - \frac{1}{\beta_{ph}^2} \right] \frac{e}{\gamma m c^2} \vec{v}_\perp \cdot \vec{E}_\perp \Delta t. \quad (1.20)$$

This equations shows that, at the autoresonance condition  $\beta_{ph}=1.0$ ,  $\Delta\omega_D = 0$  and the azimuthal and axial bunching mechanisms offset each other. At autoresonance the electrons therefore do not change their gyrofrequency with respect to the rf wave, and, if they are in the proper phase position for energy extraction, will continue to transfer energy to the wave.

The mismatch factor  $\delta$  describes the conditions for positioning the electron bunch, in the proper phase with respect to the rf wave, for energy extraction.

Resonance between the beam and the wave occurs at  $\delta \sim 0$ . The mismatch factor can be rewritten as

$$\delta = \omega - \omega_D + \Delta\omega_D \sim 0 \quad (1.21)$$

for resonance.

For wave amplification, more electrons must give up energy to the wave (i.e.  $\vec{v}_\perp \cdot \vec{E}_\perp > 0$  in equation 1.12). Equation 1.20 shows that  $\Delta\omega_D$  and the bunching term  $[1 - 1/\beta_{ph}^2]$  both must have the same sign for this to be true. For the case of a positive bunching term, most electrons must increase their Doppler shifted frequency ( $\Delta\omega_D > 0$ ). Therefore a positive mismatch factor  $\delta$  is necessary to position the electron bunch such that the majority of electrons resonate with the rf wave. (This holds true for  $[1 - 1/\beta_{ph}^2]$ ,  $\Delta\omega_D$ , and  $\delta$  all negative also.)

Up to this point it is not apparent that the beam needs to possess any perpendicular velocity other than that required to initiate cyclotron motion. The energy due to the perpendicular motion of the beam is the major portion of the energy available for transfer to the wave in a CARM. The wiggler field is frequently called the pump field, in that it raises the electron to a higher perpendicular velocity (at the expense of the parallel velocity). It is that portion of the total energy that is due to the perpendicular velocity that is available for transfer to the wave through stimulated emission. As will be seen in chapter 4, the spatial growth rate of the CARM interaction is a function of the perpendicular velocity and of the beam current.

The amplitude of the rf wave in the CARM is proportional to  $e^{i(k_\parallel z - \omega t)}$  and, the cyclotron maser instability can be either convective or absolute. Convective, or spatial, growth is desired for an amplifier and those conditions that contribute to the onset of the absolute instability that may occur at the Doppler downshifted mode must be avoided. The conditions are outlined in chapter 4.

Extensive theoretical work on the cyclotron maser interaction has been published. The analysis has been done for the CARM in free space [16,10,28] and in a cylindrical waveguide [15]. A comprehensive analysis of the CARM interaction in a

waveguide for all harmonics has been presented by Fliflet [15] and will be outlined in chapter 4. While the analytic work provides a basis for the CARM interaction in the small-signal, linear regime, to effectively model an actual device requires the use of numerical simulations to solve the nonlinear equations. The Fliflet work provides the framework of equations for modeling of the CARM interaction. The equations can be analytically solved only for the most simple of electron phase space distributions. As such, numerical simulations that utilize more realistic beam distributions to model the CARM interaction have been developed by Danly [29], and Chen [30]. The Chen model of the CARM interaction will be detailed in chapter 4.

This experiment involves the first successful construction and testing of a CARM single pass amplifier and involves two basic studies. First is the dynamics of an electron beam that must be produced, spun up, and delivered to the CARM interaction region. The second is the CARM interaction itself, in which the beam must be made to efficiently couple to the electromagnetic wave.

Following this introduction is a description of the experimental apparatus in chapter 2.

Chapter 3 discusses the dynamics of the electron beam from the general to the specific. At first, ideal orbits in ideal magnetic fields are presented. This is followed by a discussion of trajectories in realistic magnetic fields. Problems specific to this experiment such as off axis trajectories, the effects of exiting the wiggler field, and the effects of the beam space charge are presented. This is followed by a thorough presentation of numerical simulations of the beam dynamics.

Chapter 4 reviews the theoretical basis of the CARM interaction also from the general to the specific of the experiment. A presentation is made of the CARM interaction in a cylindrical waveguide. As in the previous chapter, numerical simulations and their theoretical basis are presented. As input, the results of the study of the beam dynamics from chapter 3 are tied into the CARM interaction simulations so that a reasonable prediction can be made of the experimental results.

Chapter 5 reports the observed results of the results of this experiment in a manner that shows the connection to the theoretical predictions of the previous chapter. Also presented is the manner in which the power and efficiency are optimized in this particular experiment.

The final chapter presents a summary of the results of this experiment, suggestions for ways to improve on the experiment, and possible applications.

# Chapter 2

## Experimental Apparatus

### 2.1 Introduction

A general overview of the apparatus involved in this experiment is presented in this chapter. This is followed by detailed descriptions of the various components of the apparatus. A schematic of the CARM experiment is shown in figure 2-1.

Successful operation of a CARM requires an electron beam of a given energy, a method of imparting a specific amount of perpendicular velocity to the beam and finally a region in which the CARM interaction can take place. The CARM interaction is sensitive to variations in the energy and momentum of the beam (as will be seen in chapter 4) and great care must be taken to energize and spin up the beam.

The beam is energized by transmitting a voltage pulse to a diode. Roughly 1% of the electrons that accelerate across the anode-cathode gap are transmitted into the region where the beam is spun up. The beam receives perpendicular velocity in the region of the waveguide surrounded by a helical wiggler magnet that provides a unique transverse field. The spun-up beam then exits the wiggler region and enters the region where the CARM interaction takes place. The diode, the wiggler region, and the CARM interaction region are all immersed in a solenoidal magnetic field.

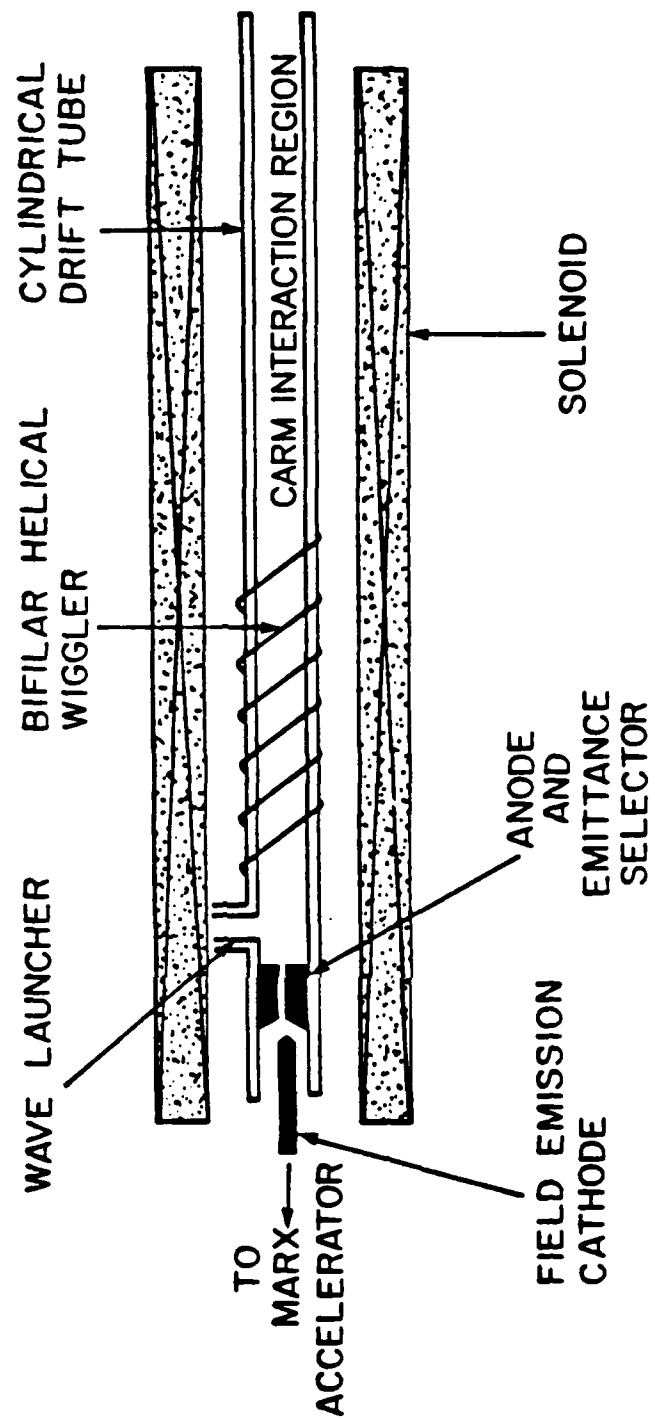


Figure 2-1: Schematic of the CARM Apparatus



When the CARM is operated as an amplifier of an input microwave signal, the input is delivered immediately after the diode. After the CARM interaction takes place, the output high power microwave signal is then propagated through an air gap and through  $K_a$  band attenuators. The output signal is then detected by means of calibrated crystal detectors.

## 2.2 Detailed Description of the Apparatus

The specifics of each component of the CARM experimental apparatus are presented in this section.

### 2.2.1 The Marx Accelerator

The power supply for the diode is a Pulserad 110A accelerator which delivers a 30 ns voltage pulse via a transmission line to the diode. The accelerator is composed of an eleven-stage Marx generator which charges an oil-filled Blumlein transmission line. An equivalent circuit of the Marx-Blumlein transmission line system is shown in figure 2-2(a). The accelerator is capable of generating a 1.4 MV, 32 kA square wave pulse to a matched  $43 \Omega$  load. A calibrated Rogowski coil mounted over the cathode (Rogowski # 1 in figure 2-3) is used to measure a 22 kA current generated at 1.5 MV, giving a measured impedance of  $68 \Omega$ .

The Marx generator is an eleven-stage, oil insulated, 2.75 kJ capacitor bank which is charged in parallel and then discharged in series. Each of the eleven stages consists of two  $0.1 \mu\text{F}$  capacitors in a common case. Each capacitor can be charged to a maximum of  $\pm 50 \text{ kV}$ . Charging is accomplished by a  $\pm 50 \text{ kV}$ , 1 mA Universal Voltronics power supply. The capacitors are connected in series by pressurized  $\text{SF}_6$  spark gaps (12-32 psi). The initial three spark gaps in the series are fired by a Physics International TG-70 trigger that connects the first three capacitors. This results in an overvoltage on the succeeding spark gaps which causes a voltage

cascade.

The output voltage is delivered to a high voltage Blumlein transmission line. A schematic of the transmission line is shown in figure 2-2(b). The transmission line is used to deliver the pulse because the risetime of the Marx generator is a few hundred nanoseconds which is not appropriate for the diode which operates on the order of tens of nanoseconds. The long rise time is due to the high internal inductance of the Marx generator circuit which limits the rise time of the current pulse. The technique to shorten the risetime is to use a low inductance, high voltage transmission line between the Marx generator and the diode.

The Blumlein itself is composed of three concentric aluminum cylinders which form two coaxial transmission lines. The high voltage from the Marx generator charges the intermediate conductor. The inner and outer conductors are held at ground during charging of the Blumlein. When the voltage on the transmission line intermediate conductor reaches some critical value, a short circuit is made by a  $\text{SF}_6$  switch to it and the inner conductor. This produces a positive voltage on the inner conductor and a negative voltage of the same value on the outer conductor. The load is placed between the inner and outer conductors which acts as a coaxial transmission line that has a voltage pulse twice that of the initial charging of the intermediate conductor. Since the voltage that is seen by a matched load of a transmission line is half that of the transmission line voltage, the voltage that is delivered to the load is the full charging voltage. The output pulse length is determined by the propagation time of a *TEM* mode travelling in the line, in this case 30 ns. By mismatching the load, more voltage can be provided to the diode, however with a concurrent loss of power. The undelivered power is then reflected back to the Marx generator. This reflected power will degrade the waveform of the voltage pulse and can damage the Marx generator. As a final precaution, to prevent the diode from drawing current during the voltage risetime, another  $\text{SF}_6$  prepulse switch is positioned between the Blumlein and the diode.

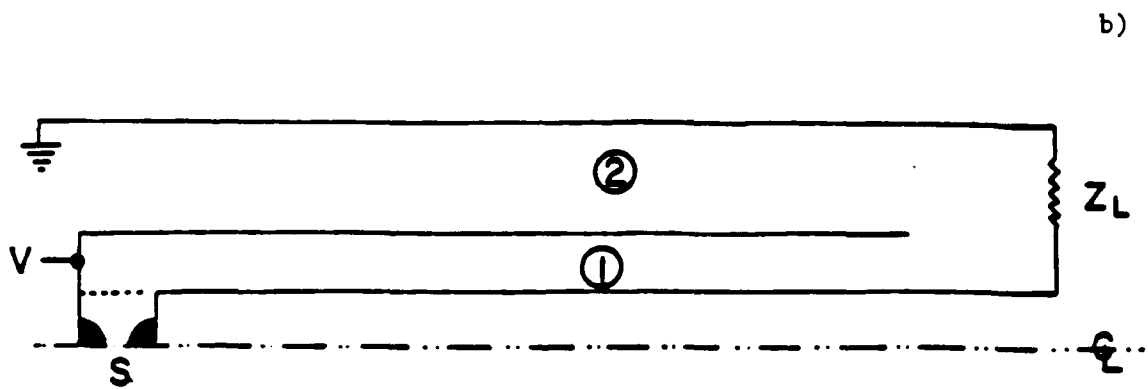
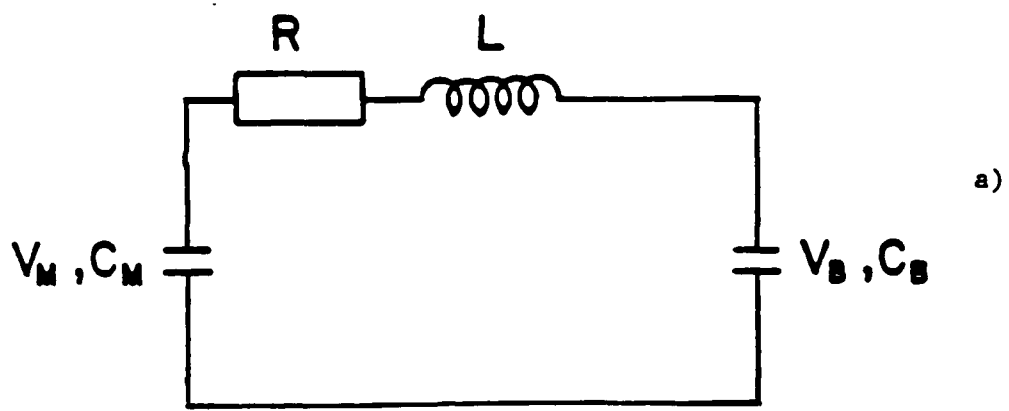


Figure 2-2: (a) Equivalent circuit of the Marx-Blumlein transmission line system.  
 (b) The Blumlein transmission line configuration.

### 2.2.2 The Diode

The diode used in this experiment is similar to a design that has been used previously [31]. As shown in figure 2-3, the diode is formed by placing a cylindrical cathode a fixed distance from a conically shaped anode. Both anode and cathode are constructed of machined POCO graphite which is a relatively hard (compared to other available graphite products) with a density of  $\rho = 1.84 \text{ gm/cm}^3$ .

The electron beam in the diode is generated through the process of explosive field emission. When the strong electric field due to the voltage pulse from the Marx generator is applied across the anode-cathode gap, intense electron flow begins through microscopic projections on the cold cathode surface. This flow leads to resistive heating and vaporization of the microscopic points. These cathode flares expand and form a surface plasma. The current that flows across the gap is limited only by the modification of the equipotential contours in the diode due to the space charge of the electron current [32].

The emitting surface of the cathode is a hemispherically shaped section of POCO graphite connected by a 50 cm aluminum stalk to the center conductor of the transmission line. The anode-cathode gap can be adjusted by the placement of aluminum spacers prior to the graphite tip. The gap used in this experiment is 1.0 cm. The conical angle of the anode is  $10^\circ$  measured from the perpendicular to the anode axis. The contours of the anode and cathode are designed [31] to provide a planar equipotential surface over the anode port. A port of 0.318 cm radius is made in the anode along the axis to permit the transmission of current into the CARM experimental region. The axial thickness of the anode is 7.62 cm which is sufficiently long to permit the electrons to complete more than one cyclotron orbit prior to reaching the exit of the anode port.

In this manner, the anode acted also as an emittance selector. As can be seen in table 2.1, the beam normalized (rms) emittance for a 0.318 cm radius anode port is .094 cm-rad. This corresponds to an energy spread of 4.4% (half width  $\Delta\gamma_{\parallel}/\gamma_{\parallel}$ ).

This design has several advantages for this experiment. First, a good estimate can be made of the beam emittance and energy spread. Second, the transmitted current can be adjusted by the geometry of the diode or the strength of the surrounding axial magnetic field. Lastly, it is rugged and can withstand thousands of shots without degrading.

In the limit of high current electron flow, there is a potential for the self focusing of the beam in the diode across the anode-cathode gap. A rough criterion [32] for the onset of beam pinching is when the relativistic gyroradius of an electron emitted at the cathode is equal to the anode-cathode gap. The critical current is shown by Miller [32] to be  $I_c = \gamma I_A r_c / 2d$ , where  $d$  is the gap spacing (1 cm in this experiment),  $r_c$  is the cathode radius (0.89 cm in this work) and  $I_A = 17$  kA is the Alfvén current. The measured current across the anode-cathode gap is 22 kA which is less than  $I_c = 30$  kA.

The beam emittance and energy spread can be deduced through a technique developed at the Lawrence Livermore National Laboratory. It is based upon a definition of normalized brightness by D. Proznitz for the Electron Laser Facility (ELF) emittance selector [33,34]. This selector is a long pipe immersed in a solenoidal field. Since the anode port in this experiment can be considered 'long' in that it is longer than the  $z$  distance an electron travels in a cyclotron orbit, this technique is used here.

The normalized brightness of the diode is defined as

$$B_n = \frac{\pi^2 \delta I}{(\gamma\beta)^2 (\delta^4 V)} \quad (2.1)$$

where  $\delta I$  is the current transmitted through the emittance selector. The four space volume  $(x, x', y, y')$  where the primed quantities are time derivatives) called the acceptance is defined as

$$\delta^4 V = \pi^2 r_p^4 \Omega_{c0}^2 / 6c^2 \gamma^2, \quad (2.2)$$

where  $r_p$  is the emittance selector (anode port) radius. The condition that describes

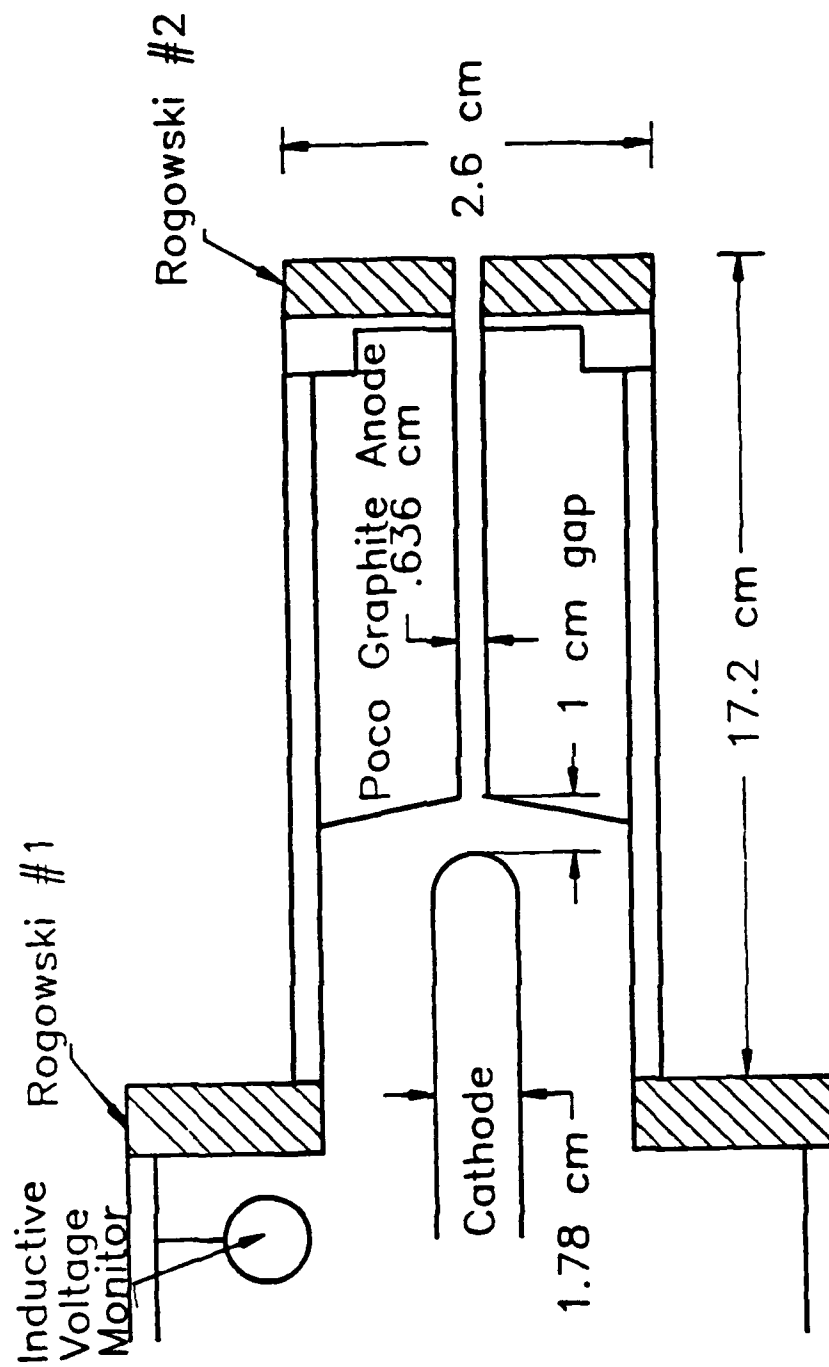


Figure 2-3: The diode

the phase space volume accepted by the emittance selector is

$$\left[\left(\frac{x'}{\Omega_c} + \frac{y}{2}\right)^2 + \left(\frac{y'}{\Omega_c} - \frac{x}{2}\right)^2\right]^{\frac{1}{2}} + \left[\left(\frac{x'}{\Omega_c} - \frac{y}{2}\right)^2 + \left(\frac{y'}{\Omega_c} + \frac{x}{2}\right)^2\right]^{\frac{1}{2}} < r_{pipe}. \quad (2.3)$$

The normalized (rms) emittance is then defined as

$$\epsilon_n^2(rms) = \frac{2\delta I}{9B_n} \quad (2.4)$$

for a uniform phase space distribution. The fractional spread in the beam energy  $\Delta\gamma_{\parallel}/\gamma_{\parallel}$ , where  $\gamma_{\parallel} = (1 - v_{\parallel}^2/c^2)^{1/2}$ , can be related to the transverse emittance, since the transverse emittance corresponds to a spread in transverse beam velocity which is a component of  $\gamma_{\parallel}$  ( $\gamma_{\parallel}^{-2} = \gamma^{-2} + \beta_{\perp}^2$ ). The beam that exits the diode is assumed to have a uniform spatial distribution of particles and a truncated momentum distribution. The momentum distribution is truncated since the particle that transits the diode at the maximum radius in the anode port can have no perpendicular velocity since any gyro-motion would cause it to impact the anode port wall. The particles with maximum spread in perpendicular velocity exist in the centerline of the anode port since their gyroradius can be the largest. The Lawrence Livermore Laboratory technique used here assumes the momentum distribution of the particles to be a truncated Gaussian. Figure 2-4 shows a phase space plot for the typical parameters of this experiment.

Since the momentum distribution is Gaussian, then  $\epsilon_n = 3\epsilon_n(rms)$  [33]. This results in the following relationship between the energy spread and the normalized emittance.

$$\frac{\Delta\gamma_{\parallel}}{\gamma_{\parallel}} \Big|_{\text{gaussian}}^{HWHM} = \frac{1}{9} \frac{\epsilon_n^2}{2r_p^2} = \frac{\epsilon_n^2(rms)}{2r_p^2}. \quad (2.5)$$

All energy spreads quoted in this work assume a uniform spatial distribution and a gaussian momentum distribution and therefore utilize the HWHM-gaussian energy spread values of equation 2.5.

The normalized brightness and emittance are measured as follows: The current transmitted through the port in the anode is measured by means of a Rogowski

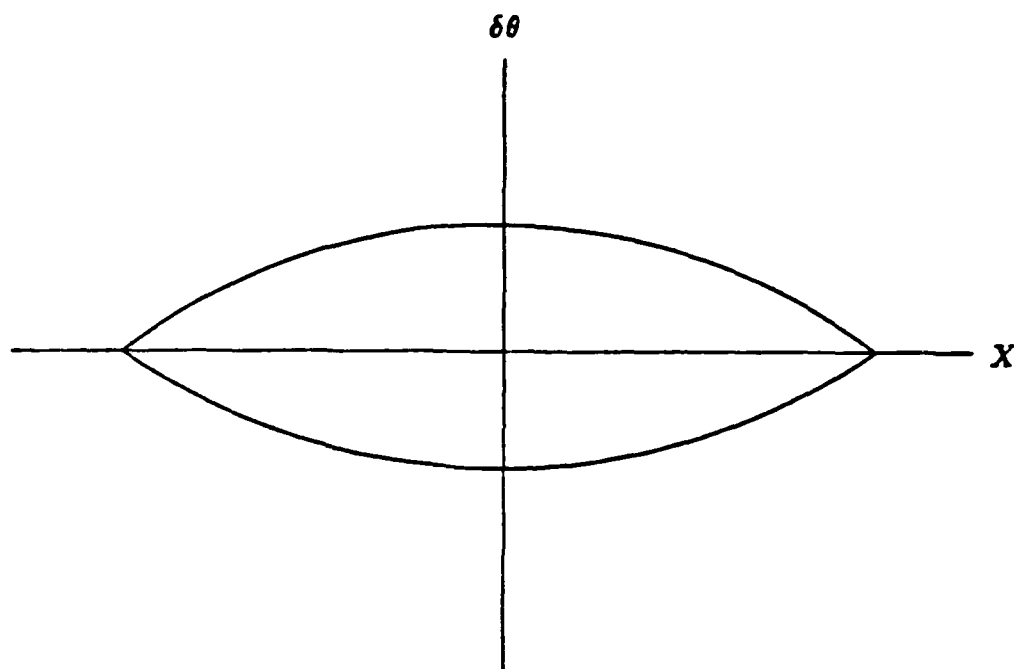


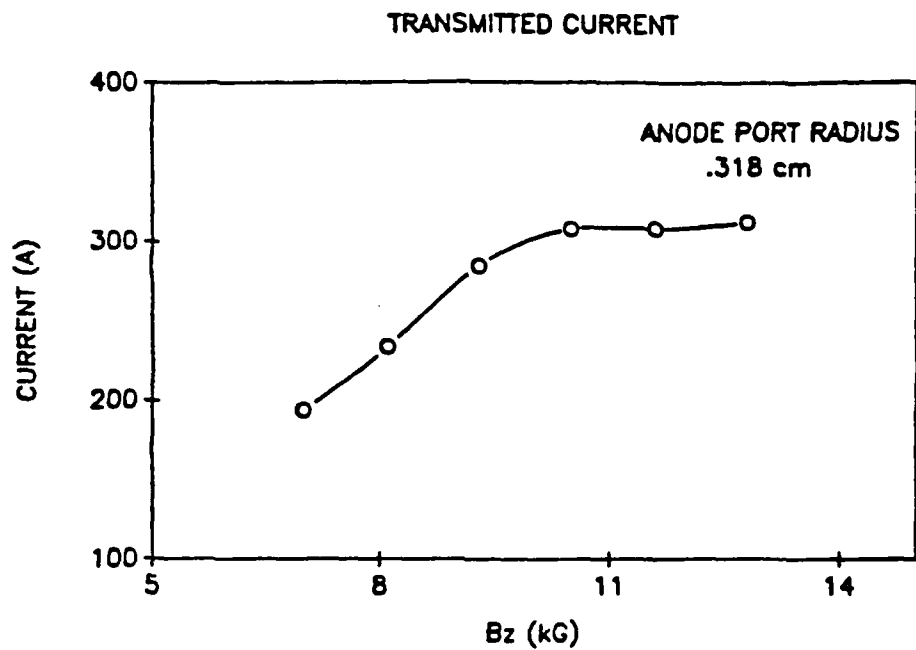
Figure 2-4: A typical phase space plot of the beam as it exits the diode. The anode port radius is 0.318 cm and the rms spread in the normalized perpendicular velocity ( $v_{\perp}/v_{\parallel}$ ) is .094 radians. radians.



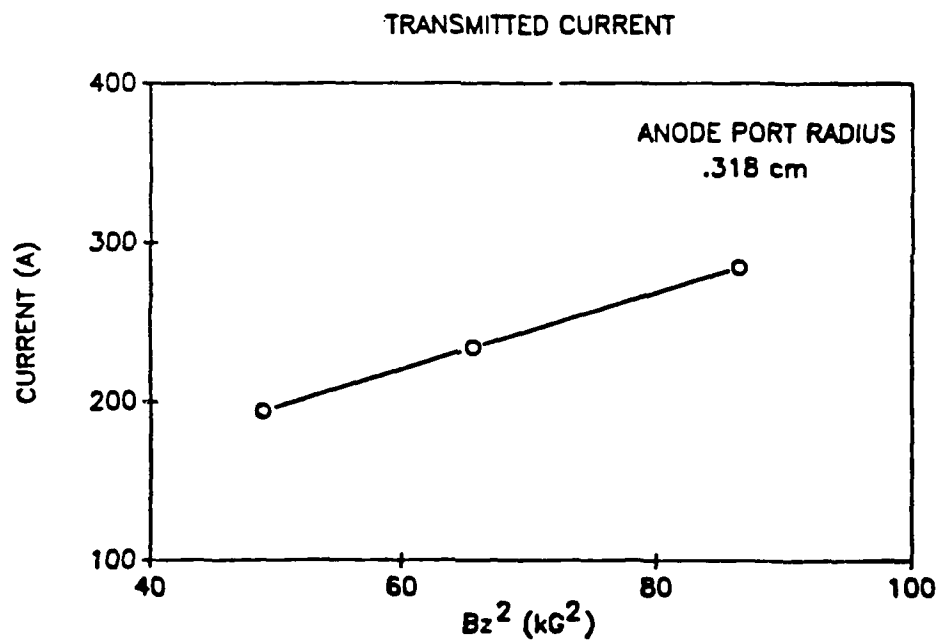
coil placed between the exit port of the diode and start of the CARM experimental structure (Rogowski #2 in figure 2-3). Figure 2-5(a) shows the transmitted current as a function of the axial field. Figure 2-5(b) shows the transmitted current as a function of the square of the axial field. Note the linear relationship between the transmitted current and the square of the axial magnetic field in figure 2-5(b). Examination of equation 2.1 shows that the brightness is a function of the parameter  $\delta I/B^2$ . The normalized brightness (equation 2.1) is calculated by using the slope of figure 2-5(b) which is  $\delta I/B^2$  equal to 5.27 A/kG<sup>2</sup>. The value of the normalized brightness is therefore constant up to the point of current saturation shown in figure 2-5(a). This value of  $B_n$  is then used to calculate the normalized (rms) emittance  $\epsilon_n(rms)$  from equation 2.4 where the transmitted current  $\delta I$  used is that corresponding to the particular magnetic field of the experiment ( $B=7$  kG at the diode and  $\delta I=195$  A).

In this experiment two diodes were used. A 0.076 cm radius anode port was used for beam alignment and as a diagnostic for determining the perpendicular velocity of the beam generated by the wiggler magnet. (Since the displacement of the beam from the axis can be related to the perpendicular velocity generated in the beam, an anode port that produced a small beam spot was necessary for accurate measurements. The results of these measurements are presented in chapter 3.) No power measurements were taken using this anode port. A 0.318 cm radius anode port was used for high power operation. This radius is the maximum possible due to the bore of the microwave input coupler that immediately follows the anode in the beam line. Since the current transmitted is a function of the square of the port radius, the 0.318 cm port allowed the maximum current into the CARM region. Table 2.1 shows the transmitted current, brightness, emittance and energy spread for the two anode ports.

It must be noted that there is considerable loss of current between the anode and the CARM interaction region due to the presence of the microwave input coupler



a)



b)

Figure 2-5: (a) Transmitted diode current at the exit of the emittance selector as a function of axial magnetic field  $B_z$ . Note that the current saturates at 10.4 kG. (b) Transmitted current versus  $B_z^2$ .

Table 2.1: Beam Parameters

Anode port radius (cm)	Axial Magnetic Field (kG)	Current transmitted (Amperes)	Brightness (normalized) (Amps/cm <sup>2</sup> -rad <sup>2</sup> )	Emittance (normalized) (rms) (cm-rad)	Energy spread uniform HWHM
$r_p$	$B_z$	$\delta I$	$B_n$	$\epsilon_n(rms)$	$\Delta\gamma_{  }/\gamma_{  }$
0.076	7.0	5.0	$3.2 \times 10^4$	$5.9 \times 10^{-3}$	.003
0.318	7.0	195	$0.5 \times 10^4$	$9.4 \times 10^{-2}$	.044

(see figure 2-10) and the action of the wiggler magnet. The current that reaches the CARM interaction region is of the order of 130 amperes. Thus, as seen from table 2.1, only 65% of the current emitted by the diode reaches the CARM interaction region.

In this experiment the voltage, the total current across the diode and the current transmitted through the anode port are measured in every shot. The diagnostics for the currents consist of the two calibrated Rogowski coils mentioned earlier in this section (see figure 2-3 for placement). The voltage delivered to the diode is measured with a resistive voltage monitor located after the prepulse switch prior to the diode. This divider consists of two copper sulfate resistors with an impedance ratio of 2160:1 connected between the high voltage conductor and the ground. The voltage signal at the divider is passed through a low pass filter and then transmitted via coaxial cables to the oscilloscope in a screened viewing room.

Due to the fast rise time of the current pulse, there is a large inductive voltage component of the signal that appears at the voltage divider. The total voltage is the sum of the resistive voltage  $V_R$  (the desired quantity) and the inductive voltage  $V_L$  (which is not desired). The inductance  $L$  of the diode is difficult to calculate because of the relatively complex geometry of the diode and the casing connecting the diode to the prepulse switch. Figure 2-6 is a schematic of the method used to physically

subtract the inductive voltage signal from the total voltage signal. This subtraction method was conducted at a low voltage (1 MV) in which the resistive voltage was eliminated via a short in the diode, resulting in the total voltage that equaled only the inductive voltage. The inductive voltage was measured via a single turn  $B_1$  loop placed a fixed distance from the high voltage conductor connected to the cathode (see figure 2-3). This signal was then passed through a series of attenuators and delays so that, when mixed with the total voltage (with the resistive voltage shorted), the signal was eliminated at the scope (see figure 2-6(b)). The short was then removed and the total voltage was then taken as the resistive voltage as seen by the diode (see figure 2-6(c)).

Figure 2-7 shows the voltage trace after the subtraction of the inductive voltage and the total current across the diode. This measurement was not conducted at higher voltages due to the destructive potential of the reflected pulse back to the Marx generator. The voltage measured in figure 2-7 is 0.885 MV which is the result of charging the Marx bank to 30 kV. The maximum charging voltage of the Marx bank is 50 kV, which was the value used in the experiment. Since the voltage discharged (in series) by the capacitor bank is a linear function of the charging (in parallel), the diode voltage at 50 kV charging (the value used in the experiment) was taken to be  $5/3 \times 0.885 = 1.495$  MV. Using the relationship

$$\gamma = 1 + \frac{e}{m_0 c^2} V_0 = 1 + 1.96 V_0 (\text{MV}) \quad (2.6)$$

where  $V_0$  is the diode voltage, the relativistic mass factor for the maximum charging is  $\gamma=3.94$ .

### 2.2.3 The Solenoid System

The solenoid surrounds the entire apparatus of the experiment, except for Marx bank and the transmission line (see figure 2-1). The axial field is provided by two pulsed solenoids connected in series. Each has an overall length of 92 cm and consists

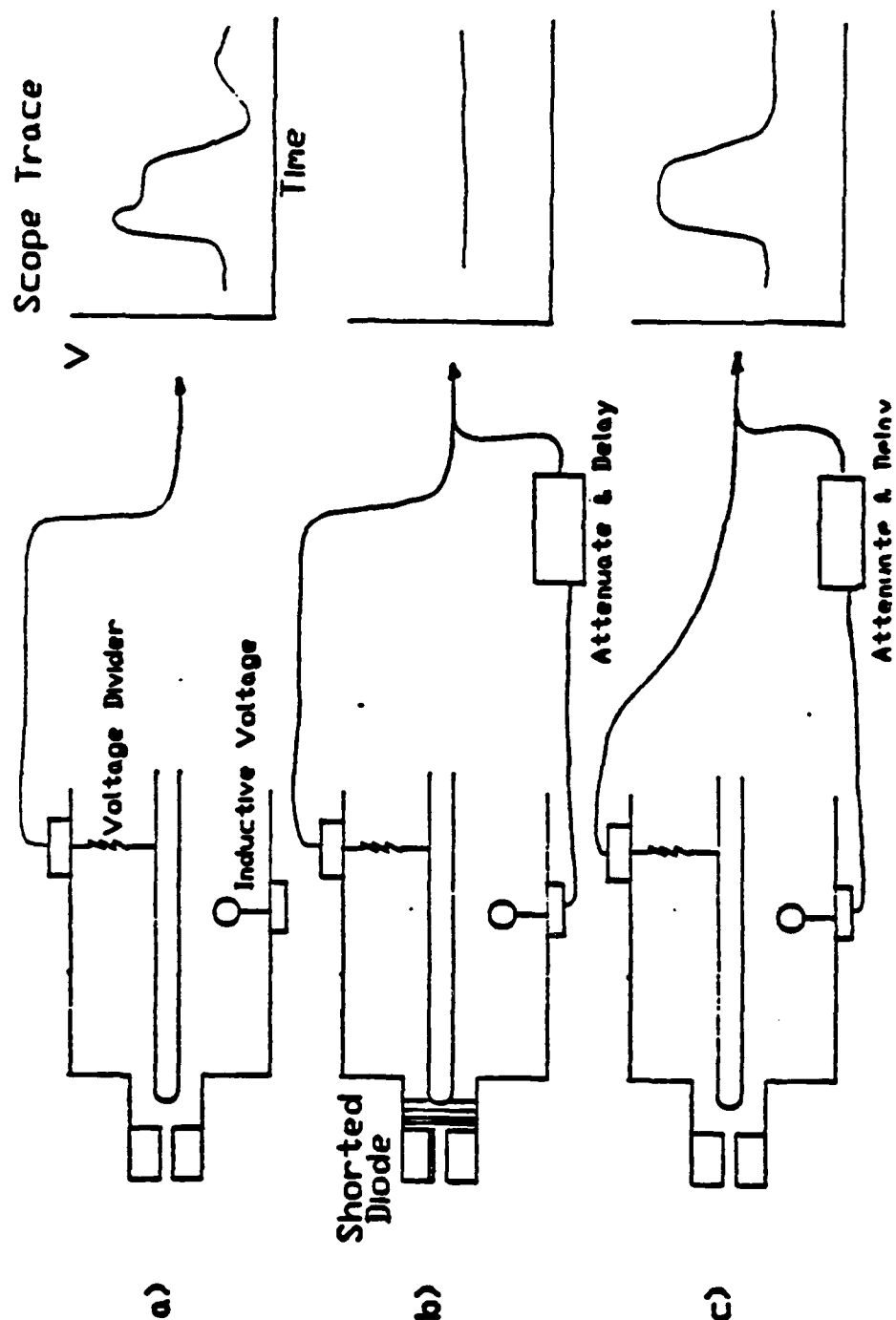


Figure 2-6: Inductive voltage subtraction method. (a) Total voltage is read across a voltage divider. (b) Diode voltage is shorted and inductive voltage is measured via a  $B_1$  loop. Inductive voltage is subtracted from voltage across the voltage divider. (c) Short is removed and total voltage is read at the scope.

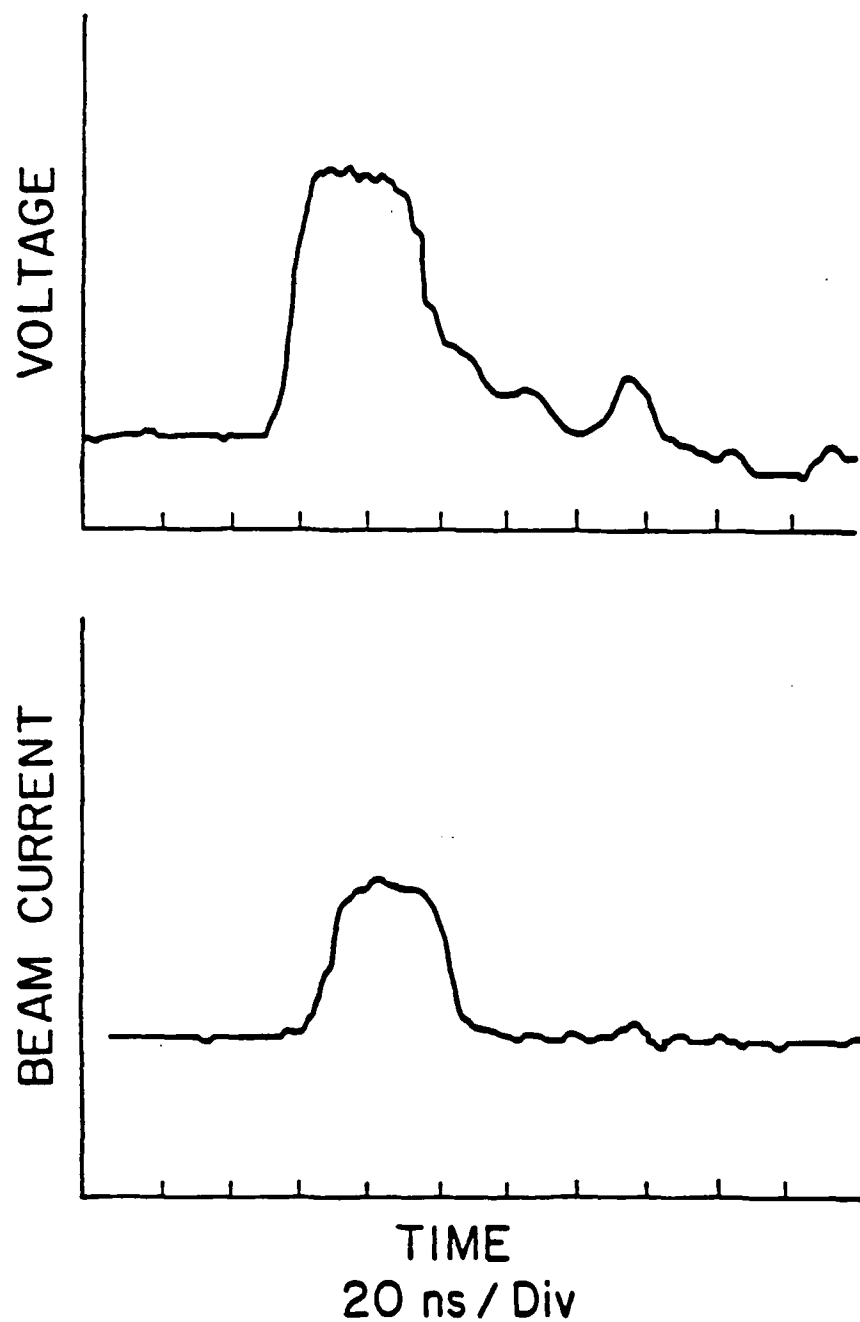


Figure 2-7: Diode Voltage and Current (a) True resistive voltage which determines beam energy (b) Total current transmitted across the diode.

of 25 turns per centimeter wound in 7 layers on a 8.23 cm OD phenolic tube. There are two extra layers of windings that cover the first 17 cm of the first solenoid. These extra turns surround only the diode and microwave input coupler regions. They are applied over the diode to increase the current transmitted through the anode port of the diode and over the input coupler to increase the current transmitted through the 1/4 inch ID pipe section of the coupler. As can be seen in figure 2-5(a), the transmitted current through the diode saturates at a value of  $B_z = 10.4$  kG. Since the operating range of the CARM device is 5-7 kG, the extra magnetic field produced by the extra windings of the solenoid results in increased transmitted current.

The power for the solenoids is generated by a 10 capacitor bank consisting of 375  $\mu$ f capacitors which are charged in parallel to a maximum of 4 kV. The capacitors are discharged and the solenoidal magnetic field reaches its peak value after 30 ms. The capacitor bank can deliver a maximum of 500 amperes to the solenoid which is calibrated at 32.5 gauss/amp in the CARM interaction region. The maximum field is therefore 16 kG, although a field of 5-7 kG is used in the experiment.

The axial magnetic field profile is measured along the axis of the solenoid with an axial Hall probe while the solenoid was powered by a 40 V DC power supply. Figure 2-8 shows the field profile as a function of axial distance. Locations are shown for the various components of the system. There is a slight discontinuity at the juncture of the two solenoids in the center of the experiment. The field gradient can be expressed as the fractional magnetic field change per cyclotron wavelength,  $\Delta B/(l_c B)$ , where  $l_c$  is the cyclotron wavelength. The field gradient in the solenoid juncture region is 4.6% per cyclotron wavelength and is 6.2% per cyclotron wavelength in the transition between the field over the diode and the field over the wiggler region (at the operational field of 5.4 kG).

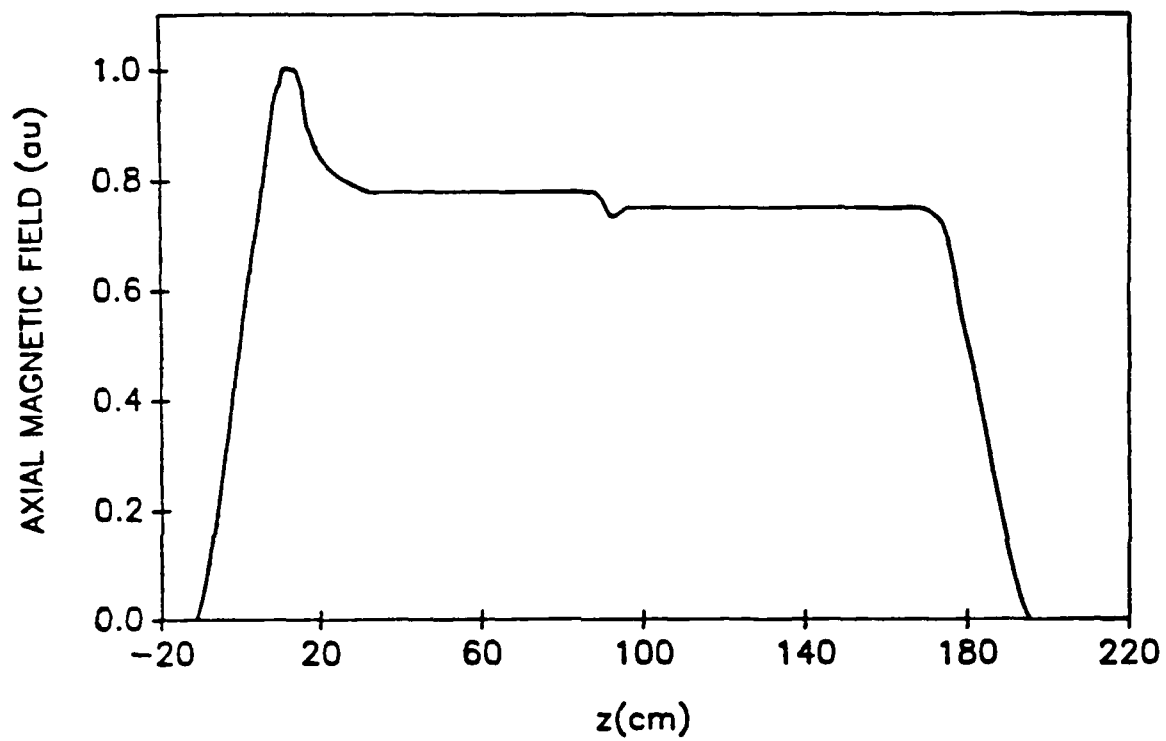


Figure 2-8: Axial magnetic field profile



## 2.2.4 The Microwave Input and Detection System

Immediately following the diode is a microwave input coupler that is used to inject a high power rf signal from a fixed frequency magnetron into the waveguide. A schematic of the entire microwave transport and detection system is shown in figure 2-9. Figure 2-10 shows the microwave input coupler in detail.

The rf power is supplied by an AN/TPQ-11 cloud height finder radar source based on a SFD-319 fixed frequency coaxial magnetron. The magnetron is powered by a 400 V HP6515A power supply that delivers up to 50 mA to the pulse-forming network of the AN/TPQ- 11. Bias voltage is maintained at -300 V by an HP6110A power supply. The high voltage for maximum rf power is in the 4.4-4.6 kV range. The magnetron operates at a frequency of 34.73 GHz with a 2.5 MHz bandwidth. The peak power available at the circular waveguide exit of the magnetron is 102 kW.

The signal generated by the magnetron exits the magnetron in a circular waveguide and is transformed into a  $TE_{11}$  mode in a rectangular  $K_a$  band waveguide. This waveguide then enters the solenoid at the exit end of the experiment parallel to the circular beampipe which is located on the solenoid axis. After traversing the length of the solenoid, the rectangular waveguide then makes an abrupt  $90^\circ$  turn and is inserted into a circular waveguide of 1/4 inch ID of the input coupler positioned immediately after the diode. This 1/4 inch diameter waveguide allows only a  $TE_{11}$  mode to propagate and cuts off all higher modes. Downstream of the input coupler is a gradual uptaper from the 1/4 inch ID bore of the input coupler to the 5/8 inch ID waveguide of the experiment.

The measured attenuation of the signal from the magnetron to the output horn of the CARM device is 5.6 dB (refer to figure 2-9). The measured attenuation of the 1.92 meter #304 stainless steel cylindrical waveguide from the uptaper after the input coupler to the output horn is 0.64 dB/m. This compares favorably with the value of 0.50 dB/m attenuation of a steel cylindrical waveguide as calculated

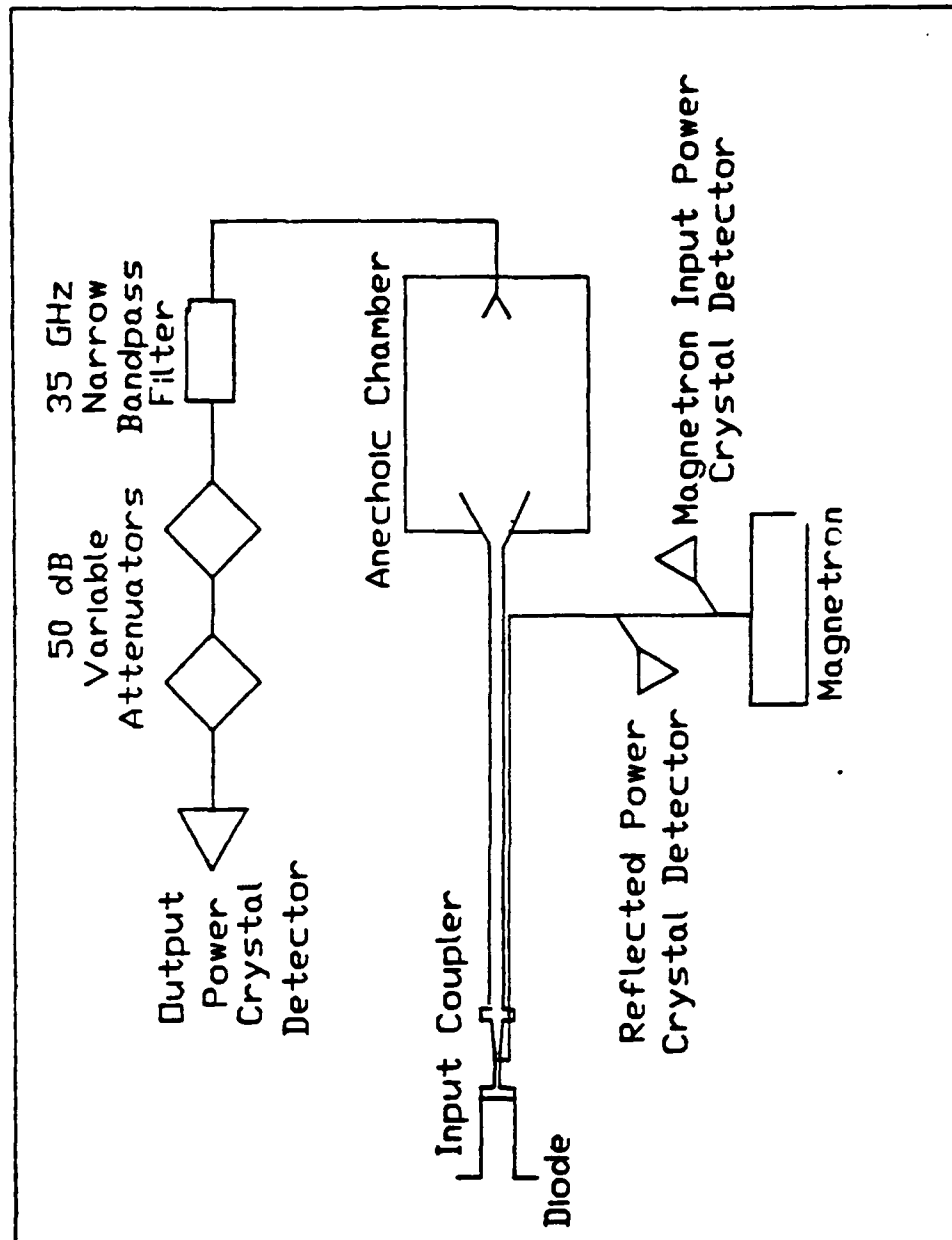


Figure 2-9: Microwave Transport and Detection System

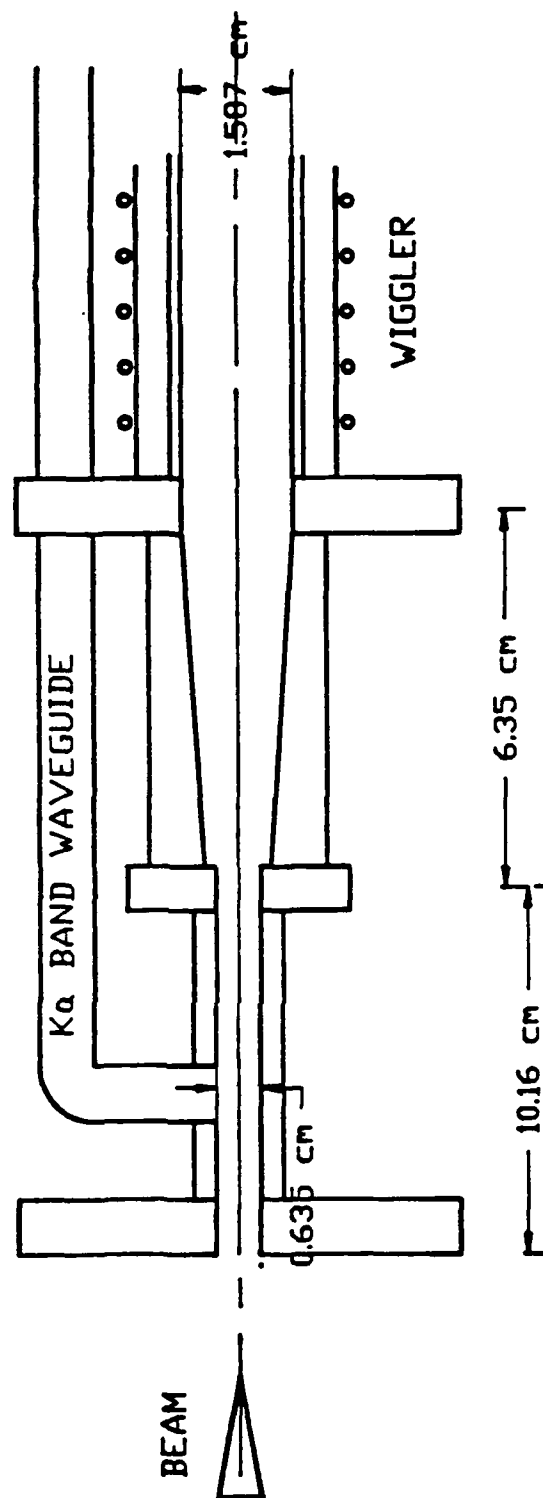


Figure 2-10: Microwave Input Coupler

by [35]

$$\alpha(\text{dB}/ft) = (6.5) \left[ \frac{0.00423}{r_w^{3/2}} \right] \frac{\left[ \left( \frac{f}{f_c} \right)^{-\frac{1}{2}} + \frac{1}{2.38} \left( \frac{f}{f_c} \right)^{\frac{2}{3}} \right]}{\left[ \left( \frac{f}{f_c} \right)^2 - 1 \right]^{\frac{1}{2}}} \quad (2.7)$$

where  $\alpha$  is the attenuation,  $f$  is the operating frequency,  $f_c$  is the cutoff frequency of the  $TE_{11}$  waveguide mode, and  $r_w$  is the waveguide radius. Measurements of attenuation were made at low power using an Alpha Corporation Gunn diode (1 mW max power) and at high power using the magnetron. Using the above attenuation measurements, a power of 50 kW read at the input power detector (see figure 2-9) corresponds to a power of 18.1 kW at the beginning of the CARM interaction region (see figure 2-1). During this experiment, powers of the range 15 to 24 kW are used at the beginning of the CARM region.

Radiation that is generated in the CARM region ( $B_z = 5.4$  kG) proceeds from there through an additional 82 cm of cylindrical waveguide ( $B_z = 0$ ) to a transmitting horn. The electron beam does not get transmitted very far past the end of the solenoid because the electrons follow the diverging magnetic field lines and eventually strike the waveguide wall.

The transmitting horn has an aperture sufficiently large so that microwave breakdown does not occur at the vacuum-air interface. Figure 2-11 is a detailed description of the transmitting horn.

The radiation pattern of the conical horn can be obtained approximately by treating the radiation pattern as Fraunhofer diffraction with the source at the apex of the horn and the aperture at the horn base. The phase difference between a ray along the axis and a ray at the aperture edge can be treated as a quadratic error  $\beta r^2 = (\pi a / \lambda) r^2$  [36] where  $a$  is the aperture radius,  $\lambda$  is the free space radiation wavelength, and  $r$  is the normalized radial distance in the plane of the aperture. The field pattern can be calculated from the following integral

$$g(\theta, \phi) \propto \int_0^{2\pi} \int_0^1 f(r, \phi') e^{(ur \cos(\phi - \phi') - 4\beta(r \cos(\phi - \phi'))^2)} r dr d\phi \quad (2.8)$$

where  $u = k \sin(\theta)$ ,  $k = 2\pi/\lambda$ , and  $f(r, \phi')$  is the illumination function, and  $\theta$

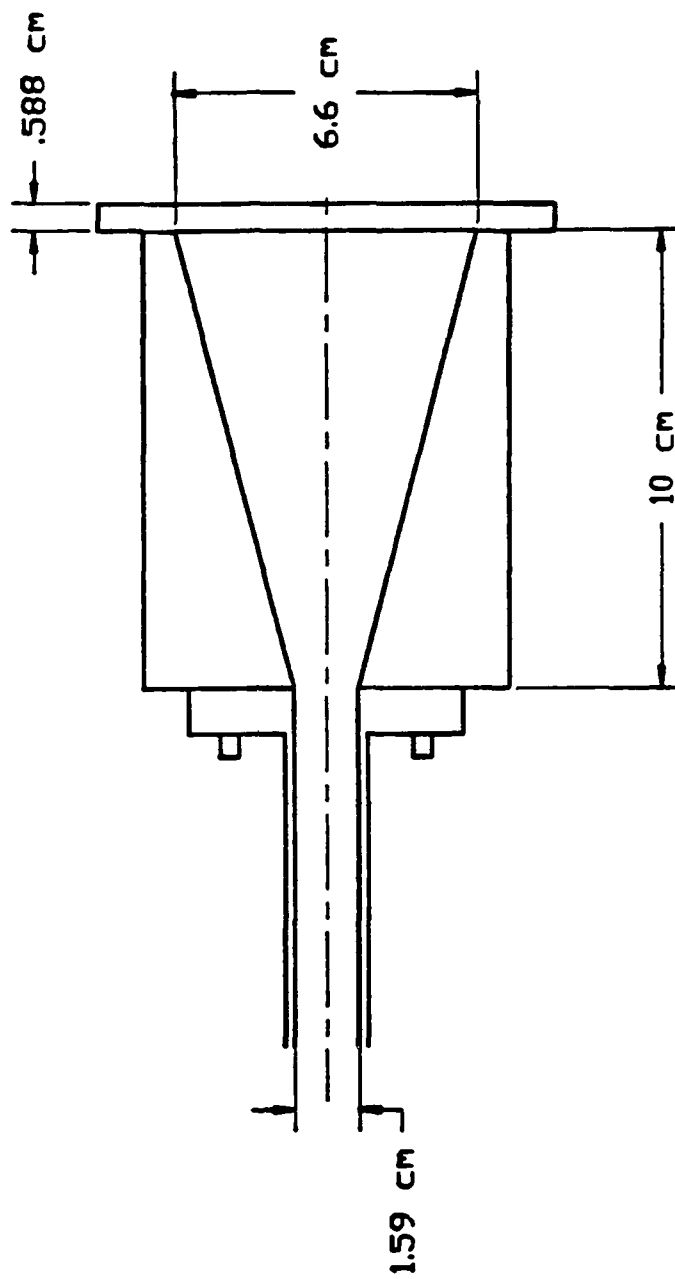


Figure 2-11: The Transmitting Horn

and  $\phi$  are the spherical angles from the center of the aperture to the point of interest ( $\phi$  is fixed here). The illumination function can be constructed [37] from the individual  $TE$  and  $TM$  modes of the wave. The radiation pattern can then be determined by numerical solutions to the square of the integral of equation 2.8. The quadratic phase error  $\beta r^2$  is equal to 0.295 at the aperture edge for the horn in this experiment. The primary effect of the quadratic phase error is to smooth over the zeros of the intensity pattern and widen the main lobe. As will be seen in chapter 5, there are four waveguide modes that are likely to interact with the electron beam. Their calculated intensity patterns are shown in figure 2-12(a). A comparison of the measured  $TE_{11}$  mode launched from the magnetron and the calculated mode pattern are shown in figure 2-12(b) showing good agreement.

With the CARM interaction providing multimewatt powers, it is essential that a means of reducing the signal to a level that could be safely intercepted by the microwave detectors is developed. The first stage of reduction is a 91 cm air gap between the transmitting horn and the pickup horn at the detector array. The 91 cm gap assures that the pickup horn is in the far (Fraunhofer) field. This was confirmed by a test of the  $1/r^2$  dependence of the pickup intensity. Since the CARM interaction region is in vacuum, a transmitting surface was needed on the transmitting horn that could hold the vacuum and also be transparent to the microwave radiation. A transmitting surface with a minimum amount of reflection is required so as to reduce the possibility of multipass CARM operation. The reflectivity of the window is given by

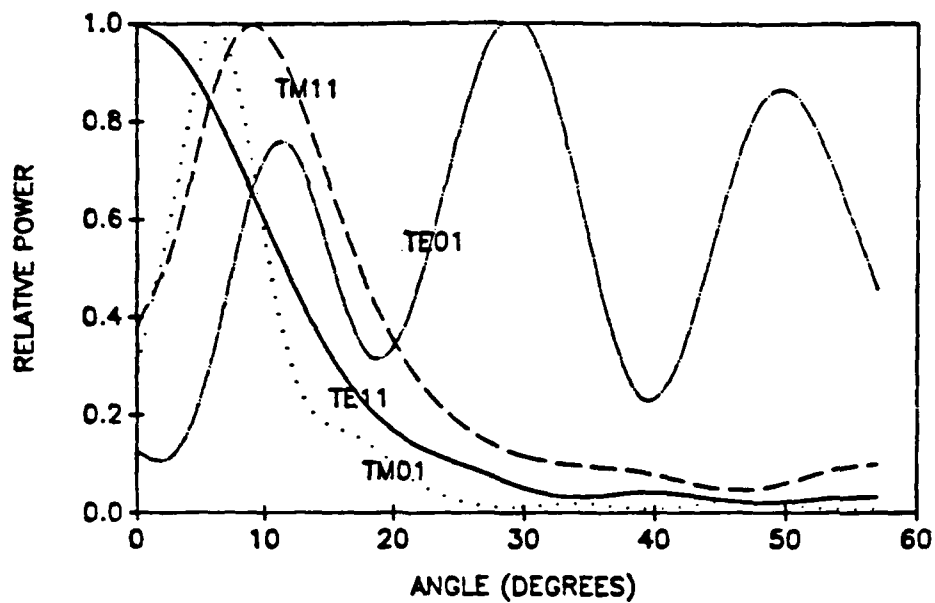
$$R = \frac{F \sin^2(kL)}{1 + F \sin^2(kL)} \quad (2.9)$$

where

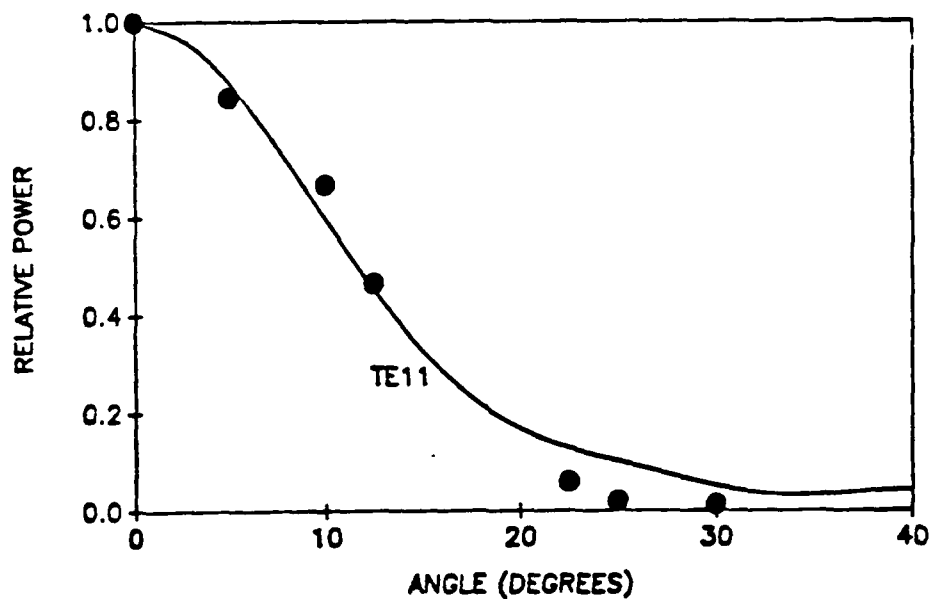
$$F = \left( \frac{2r}{1 - r^2} \right)^2 \quad (2.10)$$

$$r = \left( \frac{\mu - 1}{\mu + 1} \right) \quad (2.11)$$

$k = 2\pi\mu/\lambda_0$  is the wavenumber of the radiation in the material,  $\mu$  is the refractive index of the window material, and  $L$  is the window thickness. The thickness for zero



(a)



(b)

Figure 2-12: Radiating horn mode patterns. (a) The calculated patterns for the four modes available to the CARM interaction. (b) A comparison between the calculated  $TE_{11}$  mode pattern (solid line) and the observed pattern (solid circles) of the  $TE_{11}$  mode launched from the magnetron.

reflectivity is then integer multiples of  $\lambda_0/2\mu$  where  $\lambda_0$  is the free space wavelength of the radiation. The transmitting window was constructed of TPX plastic ( $\mu = 1.458$ ) and milled to a thickness of .588 cm for zero reflectivity. The actual power reflected by the window was measured to be 47 dB lower than the input level. Earlier, during experimentation, a window was constructed of plexiglass ( $\mu=1.603$ ) with a reflectivity of 10%. This led to multipass performance of the CARM and will be discussed in chapter 5.

The power that is delivered by the CARM to the transmitting horn is allowed to propagate over the 91 cm air gap resulting in a signal reduction of 29 dB. The signal received by a small pickup horn (see figure 2-9) is then passed through several variable precision attenuators (of up to 50 dB attenuation each) that reduce the power to a level appropriate to the detectors. Use is made of calibrated Hewlett Packard PN-R422A crystal detectors whose maximum operating power level is on the order of 100mW. The pickup horn can also be rotated azimuthally about the  $z$  axis to analyze both orthogonal polarizations of the radiation. Finally, the pickup horn can be rotated about the output horn in order to obtain an angular scan of the emitted radiation.

The R422A crystal detectors were mounted to the WR-28 waveguide and are designed for high sensitivity and have a fast response nearly independent of frequency. A calibration of the voltage signal output of the crystal versus power input to the crystal is shown in figure 2-13 and is treated as linear on the log-log scale. The calibration equation corresponding to the detector shown in figure 2-13 is

$$\text{Power(mW)} = 0.103(\text{mV})^{0.886}. \quad (2.12)$$

All power measurements performed in this experiment utilize the R422A crystals with the detector output cables terminated in  $50 \Omega$  in order to minimize cable ringing in pulsed operation. Finally, prior to detection, the output signal is passed through two Systron Donner P/N DBD-735 narrow band pass filters that allow only frequencies of  $34.8 \pm 1.2$  GHz to reach the detector. The calibration curve for this



HP DETECTOR PN R422A  
SN 1942A0294J

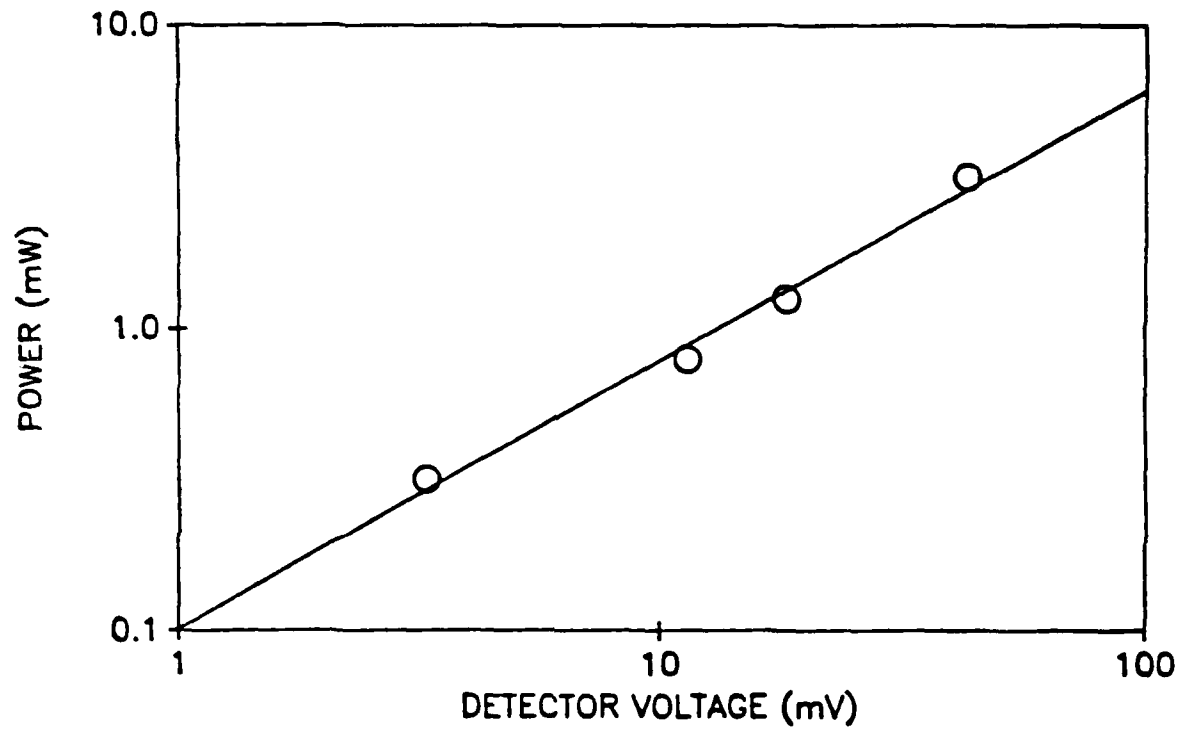


Figure 2-13: Crystal Detector Calibration Curve

filter is shown in figure 2-14.

### 2.2.5 The Wiggler Magnet

The next section of the experiment after the microwave input coupler is the waveguide which is surrounded by the wiggler magnet. The purpose of the wiggler magnet is to provide perpendicular velocity to the beam. Two different wiggler magnets are used in this experiment. The designs of both are quite similar and the construction techniques were the same. Common to both wigglers is the gradual uptaper of the field through the use of resistive shunts and the nonadiabatic termination of the wiggler through a shorting ring.

At the input end, the field is gradually increased along the  $z$  axis in order to minimize the spread in perpendicular velocity generated in the beam. At the output end of the wiggler, the field is abruptly terminated so that the perpendicular velocity of the beam is retained. Each wiggler allowed for a separate class of electron orbits to be utilized in the experiment. As will be seen in chapter 3, the orbits are classed as either group I or group II. Each wiggler is a right-handed bifilar helical winding over a phenolic tube. The wiggler with a winding period of  $\lambda_w = 4.06$  cm is called the group I wiggler and the one with  $\lambda_w = 7.00$  cm is called the group II wiggler.

The wiggler must impart perpendicular velocity to the beam while minimizing the velocity spread above that generated by the diode. Two factors are critical in minimizing velocity spread: the first is the harmonic content of the off-axis wiggler field and the second is the wiggler termination. The following is the decision process in designing the group I and II wigglers. The action of the beam in these wigglers will be discussed in chapter 3.

The formula for the field of a current driven (thin wires), infinitely long bifilar helical wiggler is, in cylindrical coordinates, [38,39]

$$\vec{B}_w = -\frac{2ik_w b \mu_0}{\pi} \nabla \left[ \sum_{p=1}^{\infty} \sin \frac{p\pi}{2} \cos p(\phi - k_w z) K'_p(pk_w b) I_p(pk_w r) \right] \quad (2.13)$$

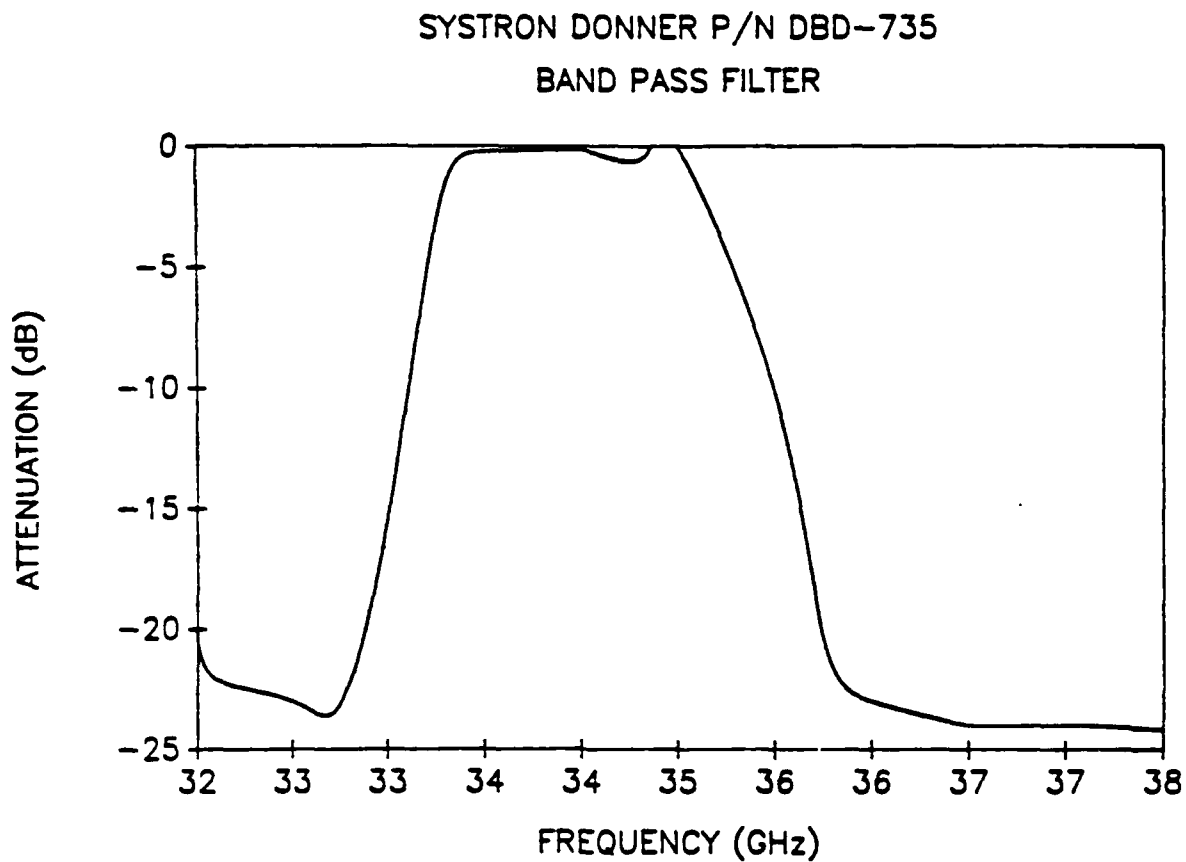


**Figure 2-14: Band Pass Filter Calibration**

where  $k_w$  is the wavenumber associated with the winding periodicity ( $k_w = 2\pi/\lambda_w$ ),  $b$  is the radius of the wiggler winding,  $r$  is the radial position measured from the  $z$  axis,  $i$  is the current in the windings, and  $I$  and  $K$  are modified Bessel functions[40]. A proper choice of  $b$  and  $k_w$  in equation 2.13 can insure that off-axis wiggler field harmonics are minimized since the wiggler field strength is a function of the product  $k_w b$ .

The harmonic content of equation 2.13 can be graphically seen in figure 2-15 for the case of two different wiggler radii ( $b=0.90$  cm and  $b=2.6$  cm). Both cases are taken for a value of  $k_w = .897$  cm<sup>-1</sup> (the group II wiggler) and  $r = .6$  cm which is the maximum excursion of the beam in the waveguide. Note that the large radius wiggler drastically reduces the harmonic content of the field at the position of the electron. An alternative to increasing  $b$  is to increase  $k_w$  by shortening the period of the wiggler winding. Changing  $k_w$  is also a method of transitioning between group I and II orbits. Two cases were tried with  $\lambda_w = 7.0$  cm and  $\lambda_w = 4.06$  cm for  $b=0.90$  cm with similar improvements for the group I wiggler.

There can exist a large spike in the wiggler field at the termination of the wiggler in a shorting ring [38,39]. The critical parameter is the ratio between the winding radius  $b$  and the winding periodicity  $\lambda_w$ . The spike is negligible if the ratio  $b/\lambda_w \leq 0.6$ . To graphically portray the end spike effects and the relationship of the end spike strength to the ratio  $b/\lambda_w$ , use was made of the COILE [41] simulation that modeled the magnetic field of the wiggler using the Biot-Savart law to generate a realistic magnetic field on axis. Each wire of the helical wiggler was numerically broken into small steps and the magnetic field determined from

$$d\vec{B} = \frac{\mu_0 I d\vec{l} \times \vec{r}}{4\pi r^3}. \quad (2.14)$$

Figure 2-16 shows the wiggler field components and wiggler field magnitude for two different wigglers. The simulations were done for  $\lambda_w=4.06$  cm (group I wiggler) and for two winding radii ( $b= .9$  cm in figure 2-16(a) and  $b=2.6$  cm in figure 2-16(b)). The wiggler without the end spike ( $b=0.9$  cm and  $\lambda_w=4.06$  cm) is used in this

### WIGGLER FIELD HARMONIC CONTENT

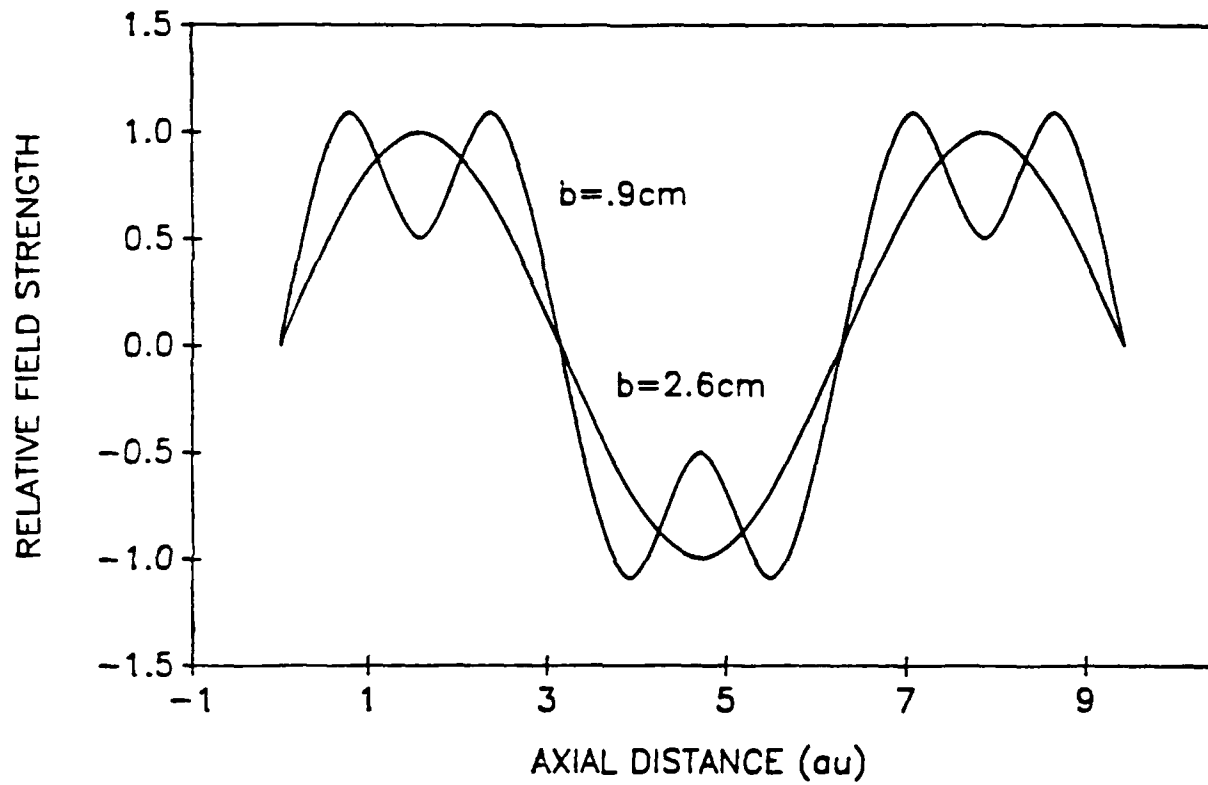


Figure 2-15: Wiggler Field Harmonic Content

experiment.

Based on this analysis of both field harmonics and end spike effects, the group I wiggler is designed with  $\lambda_w=4.06$  cm,  $b=0.9$  cm and the group II wiggler with  $\lambda_w=7.00$  cm and  $b=2.6$  cm. In this manner, two different wigglers are used for two separate classes of orbits, yet their characteristic field profiles are very similar. Neither wiggler has a significant off-axis harmonic field content nor an end spike.

A circuit diagram common to both the group I and II wigglers is shown in figure 2-17. Both the group I and II wigglers can be described by this figure since the only differences between the two are the winding periodicity  $\lambda_w$ , the winding radius  $b$ , and the overall length  $l$ . The helical coils of the wiggler are constructed of #12 a.w.g. copper wire that is wound onto a machined phenolic tube. This tube then is placed coaxially over the cylindrical waveguide (3/4 inch OD). The wiggler field is gradually increased by the use of resistive shunts that are placed every half period [42]. The shunt resistances used in this experiment are  $R1=.3$   $\Omega$ ,  $R2=.2$   $\Omega$ , and  $R3=.1$   $\Omega$  as shown in figure 2-17. These resistive rings are made from nichrome wire flashed with a very fine copper coating which insures that good electrical contact is made with the wiggler winding.

The field is abruptly terminated using a copper shorting ring. The measured field profiles of the group I and II wigglers are shown in figure 2-18 and 2-19. They are both constructed with the same set of resistive shunts and are both terminated with a copper ring. The magnetic field profiles shown are taken on axis with a transverse Hall probe while the wiggler magnets are powered by a 40 V DC power source. Table 2.2 is a comparison of the characteristics of the group I and II wigglers.

The wiggler magnet power supply is a 4 mf, 4000 V capacitor bank with a rise time of 120  $\mu$ s when operated with either wiggler magnet. The current from the capacitor bank is monitored by a T&M Research model F-1000-2 current viewing resistor ( $R=.000498\Omega$ ). The maximum current that can be delivered is about

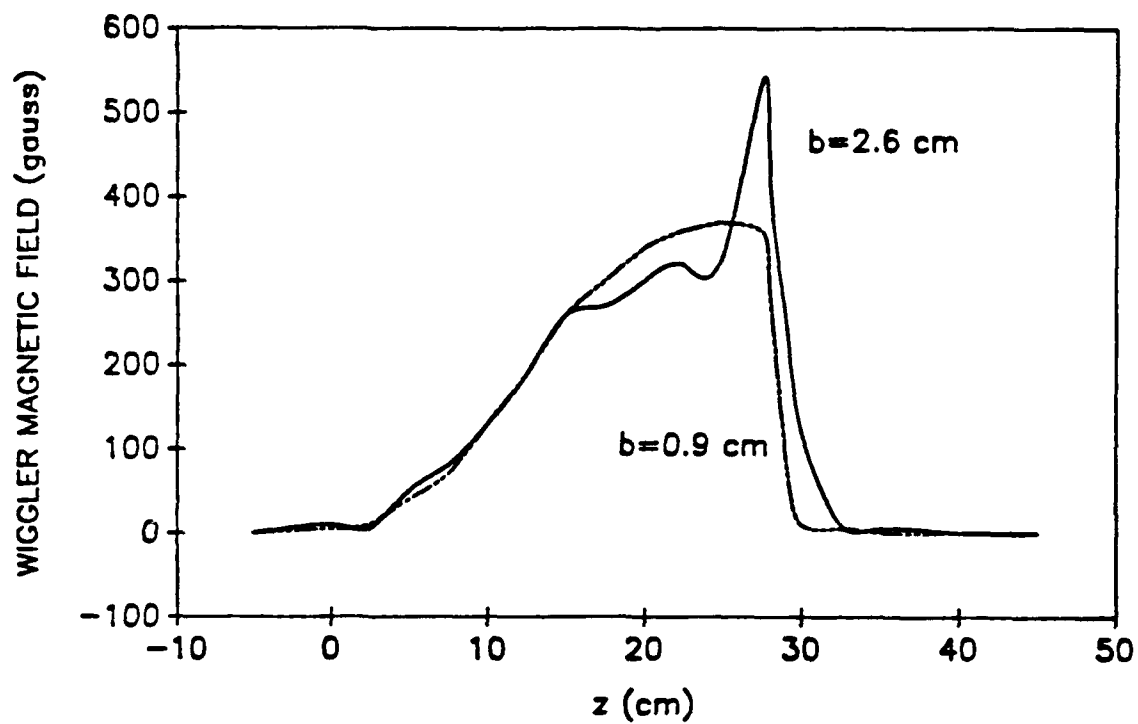


Figure 2-16: Wiggler Field Profiles,  $\lambda_w = 4.06$  cm with  $b = .9$  and 2.6 cm

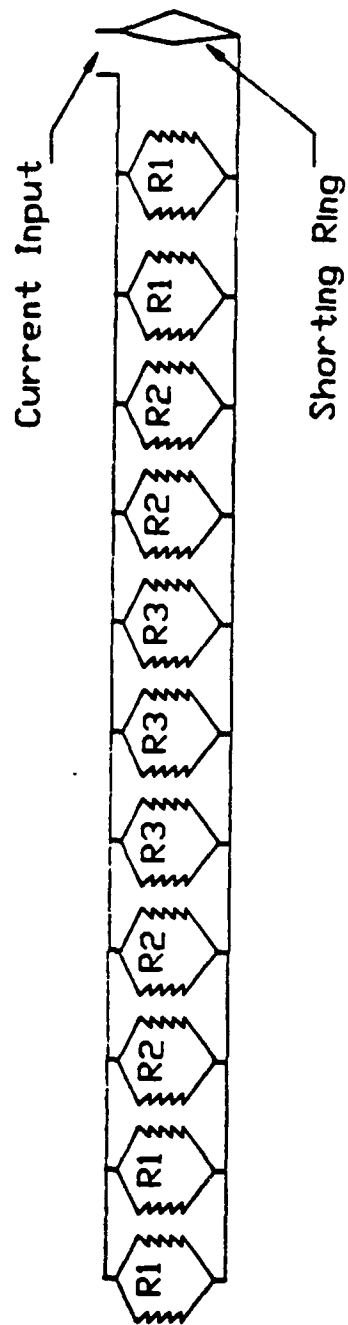
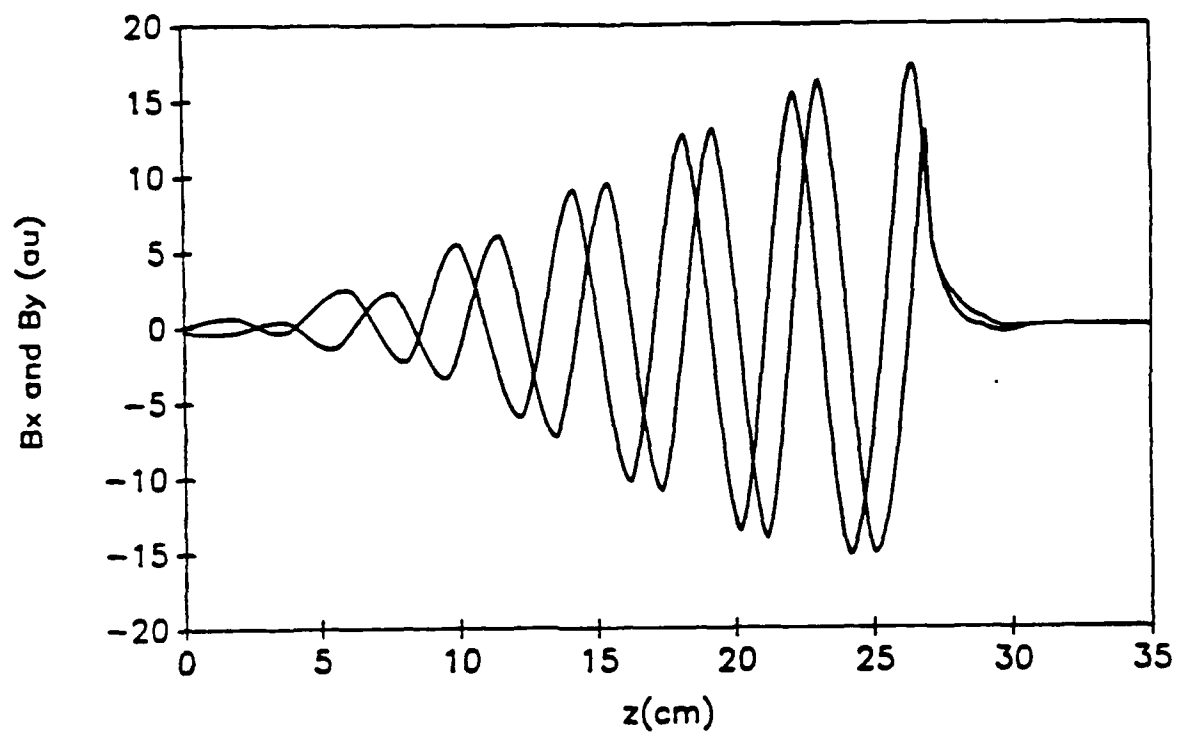


Figure 2-17: Wiggler magnet schematic showing shunt resistors and shorting ring.  
 $R1 = .3 \, \Omega$ ,  $R2 = .2 \, \Omega$ , and  $R3 = .1 \, \Omega$





**Figure 2-18: Measured Field Profile of the 4.06 cm Period Wiggler**

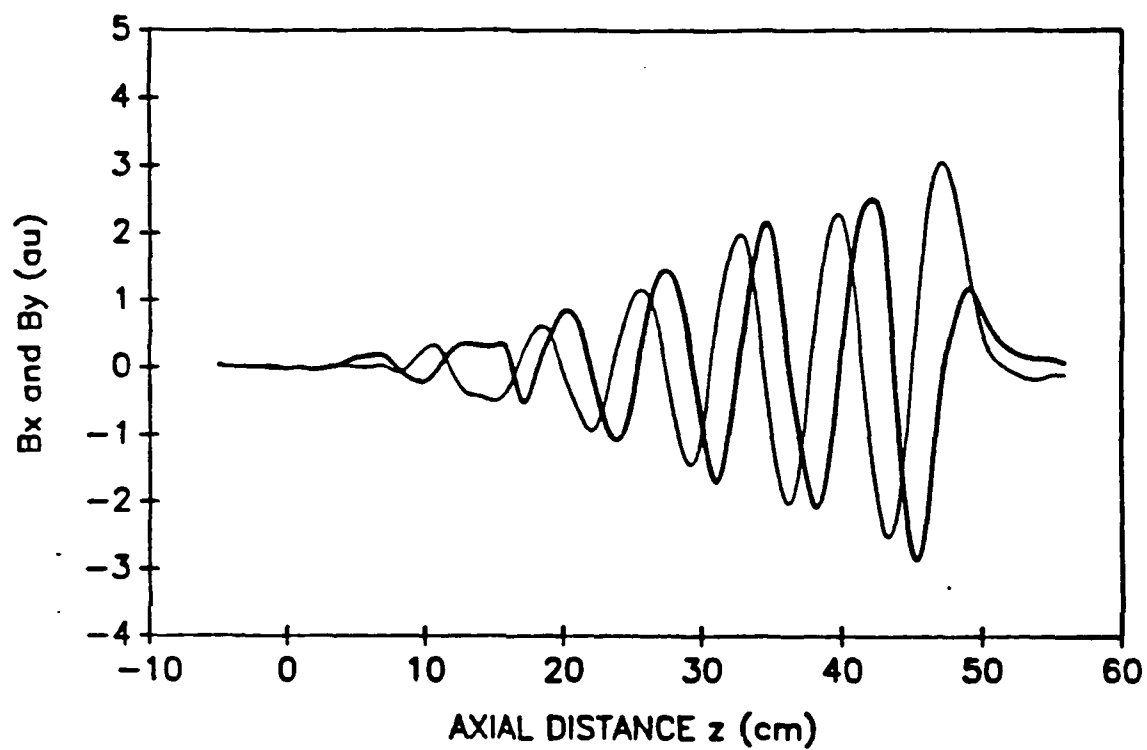


Figure 2-19: Measured Field Profile of the 7.00 cm Period Wiggler

**Table 2.2: Characteristics of the Group I and Group II Wiggler**

	Group I	Group II
$\lambda_w$	4.06 cm	7.00 cm
winding radius ( $b$ )	0.9 cm	2.6 cm
overall length $l$	27 cm	43.5 cm
gauss/amp	0.234	0.072
$B_w(max)$	11.2 kG	3.5 kG
$B_w$ used	$\leq 1.2$ kG	$\leq 1.0$ kG
$b/\lambda_w$	0.22	0.37

48 kA. Since damage to the system of shunt wires occurs at 25 kA, the maximum current was never drawn and the wiggler fields used seldom approached 1.5 kG. The maximum wiggler field was kept below this figure also due to the fact that, at the solenoidal field used in the experiment, the orbit of the beam at a wiggler field greater than 1.5 kG would cause the beam to strike the waveguide wall. (The electron orbits are discussed in chapter 3.)

### 2.2.6 The Electron Beam Current Monitors

A current probe that can measure the current and position of the beam simultaneously is used in this experiment [42]. This capability allows for the precise coaxial alignment of the waveguide and solenoid. It also allows for the determination of the spatial distribution and perpendicular velocity of the beam at any  $z$  position as will be discussed in chapter 3. This is necessary in order to determine the characteristics of the beam that generate the most radiation in the CARM interaction region. The probe also aids in the comparison of measured beam characteristics to numerical simulations of the beam dynamics and of the CARM interaction.

The probe consists of a POCO graphite current collector that is attached to

a holder that can be positioned anywhere in the cylindrical waveguide (see figure 2-20). Placing the probe at a particular  $z$  position is accomplished by means of a rigid  $50\Omega$  coaxial cable. The rigid cable is fed through a vacuum-sealed flange placed at the output end of the CARM device. The graphite collector is connected to the rigid coaxial cable via a brass holder that fits snugly inside the waveguide and is insulated from the holder by a nylon spacer. A  $2.3\ \Omega$  carbon-based shunt resistor connects the collector to the grounded brass holder. The voltage pulse across the shunt resistor, when the probe is struck by the electron beam, is then monitored. In this manner, the probe is used to measure the current as a function of  $z$ ,  $B_x$ , and  $B_w$ . The probe is calibrated with respect to a calibrated Rogowski coil (#2 in figure 2-3) by placing the probe at the exit of the anode port and delivering an electron beam from the diode. The Rogowski coil #2 was calibrated with respect to an earlier current viewing probe [42].

The probe can also be used to measure the position of the beam by placing a piece of thermal paper over the graphite collector. When a beam of sufficient current density ( $> 0.5\ \text{kA/cm}^2$ ) strikes the paper, it will leave a black mark. In this manner, the beam, in the absence of wiggler field, can be dynamically centered in the waveguide.

## CURRENT PROBE

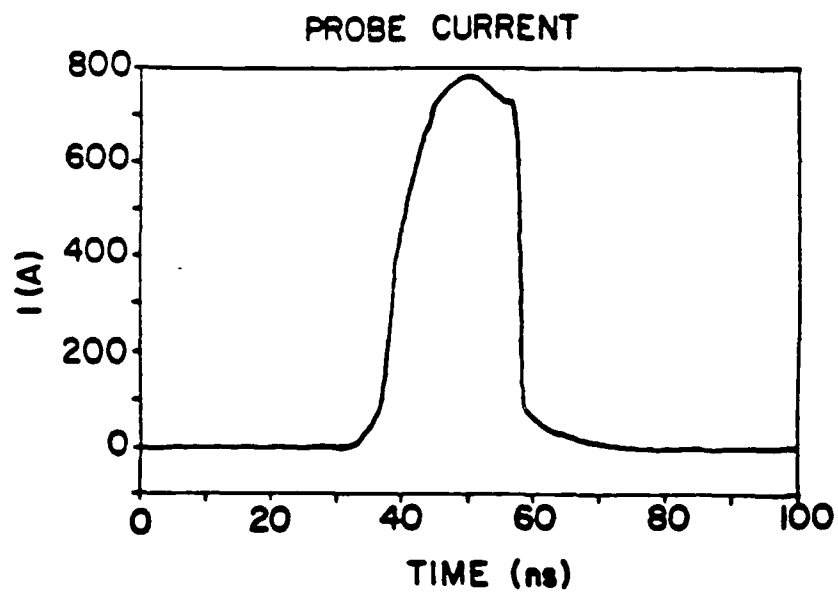
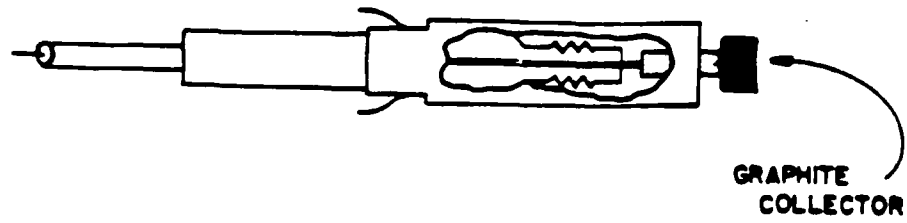


Figure 2-20: Current Viewing Probe and typical current signal pulse.

# Chapter 3

## Beam Transport

### 3.1 Introduction and Outline

The electron beam used to generate the radiation in a CARM is transported by a combination of solenoidal and wiggler magnetic fields into the interaction region where only an axial field remains (see figure 2-1). The beam is generated in the diode which is also immersed in the solenoidal field. This design eliminates the need for focusing magnets and complicated beam transport mechanisms required to deliver an electron beam into a CARM device. This chapter discusses the theory of electron orbits in a combined wiggler and axial magnetic field as well as the effects on the electron beam as it exits the wiggler and enters the CARM interaction region.

The chapter is broken into three sections. The first is a one-dimensional model of a monoenergetic, cold electron beam transported through ideal solenoidal and wiggler fields. The second is a three-dimensional model of the dynamics of realistic electron beams through realistic magnetic fields. The final section presents numerical simulations of the beam dynamics and comparisons to experimental results.

### 3.2 Ideal Electron Trajectories - One Dimensional Model

The first step in the analysis of beam dynamics is to study the motions of a single particle in a model set of magnetic fields in order to obtain an initial set of design criteria for an experiment. This section will present the dynamics of an ideal beam in an ideal axial and wiggler field configuration. An ideal electron beam is comprised of point particles, all of the same momentum and energy and, in this case, with no initial perpendicular velocity. The beam also has no finite radial extent, enters the system directly on the  $z$  axis, and neglects space charge effects.

The field that combines the effect of an axial and wiggler magnetic field is one of the form

$$\vec{B} = \hat{z}B_z + B_w[\hat{r}\cos(\phi - k_w z) - \hat{\phi}\sin(\phi - k_w z)]. \quad (3.1)$$

Friedland [43] and Diamant [44] have shown that this field configuration can result in purely helical orbits characterized by the fact that the axial and perpendicular velocities are constants of the motion. A field of this type is not, however, physically realizable by any set of windings outside of the space that field is to be generated.

The trajectories can be calculated using the conservation of energy equation

$$\gamma^{-2} = 1 - \beta_{\parallel}^2 - \beta_{\perp}^2 \quad (3.2)$$

and the momentum equation for the electrons of the beam

$$\frac{d}{dt}(\gamma\vec{v}) = -\frac{e}{m_0c}(\vec{v} \times \vec{B}). \quad (3.3)$$

If one uses the ideal field configuration given by equation 3.1 in the momentum equation 3.3, then the components of the electron velocity  $\vec{v}$  can be determined. The parallel velocity is a constant and the perpendicular velocity can be given by

$$\frac{\vec{v}_{\perp}}{c} = \left( \frac{\Omega_w \beta_{\parallel}}{k_w \beta_{\parallel} c - \Omega_e} \right) [\hat{r}\sin(\phi - k_w z) + \hat{\phi}\cos(\phi - k_w z)] \quad (k_w \beta_{\parallel} c \neq \Omega_e) \quad (3.4)$$

where  $\Omega_w = eB_w/\gamma m_0 c$  and  $\Omega_e = eB_z/\gamma m_0 c$  are the relativistic cyclotron frequencies associated with the wiggler and axial fields respectively and  $k_w = 2\pi/\lambda_w$  is the

wavenumber associated with the wiggler period. This solution is possible only if  $\Omega_w$ ,  $\Omega_c$ , and  $k_w$  are independent of position  $z$  and time  $t$ . When equation 3.4 is combined with the energy relation 3.2, the values of  $\beta_\perp$  and  $\beta_\parallel$  can be determined. The negative sign in the denominator of equation 3.4 is the result of assuming that  $B_z > 0$  in equation 3.1 which results in a right-handed twist to the perpendicular components of equation 3.1. A left-handed field would result in a positive sign in the denominator. Experimentally this field handedness is critical since reversing the polarity of the axial solenoid could result in a greatly decreased  $\alpha$  as shown by equation 3.4. In order to achieve the purely helical orbits mentioned, the electron must enter the wiggler field region from an on-axis position and proceed into a wiggler introduction that has a slow steady state buildup to full strength [45]. Helical orbits do not occur at the resonance condition  $\Omega_c = k_w \beta_\parallel c$ . A depiction of the orbit of an electron in a combined axial and wiggler field is shown in figure 3-1 which is a view looking in the negative  $z$  direction at the beam as it is adiabatically spun up.

Due to the fact that there is a resonance at  $\Omega_c = k_w \beta_\parallel c$ , the electron orbits can be classified into two groups. Group I orbits are those below the magnetoresonance ( $k_w \beta_\parallel c > \Omega_c$ ) and group II orbits are those above magnetoresonance ( $k_w \beta_\parallel c < \Omega_c$ ). Figure 3-2 shows the relationship between the parallel velocity and the axial magnetic field for a given wiggler strength and wiggler period. The trajectories shown in figure 3-2 are the solutions to the fourth order equation resulting from the simultaneous solution of equations 3.2 and 3.4. The condition for stable orbits is [43]

$$\frac{\Omega_c}{\Omega_w} \left( \frac{\beta_\perp}{\beta_\parallel} \right)^3 < 1 \quad (3.5)$$

in which case branch 3 of figure 3-2 is unstable. A choice can then be made as to which orbital group to operate in by choosing the appropriate combination of axial and wiggler field strength and wiggler periodicity.

This experiment utilizes both the group I orbits (branch 1 in figure 3-2) and the group II orbits (branch 2 with  $B_z > B_z(\text{res})$ ) to spin up the beam in two separate studies of the CARM interaction. Due to the fact that the axial field of the CARM



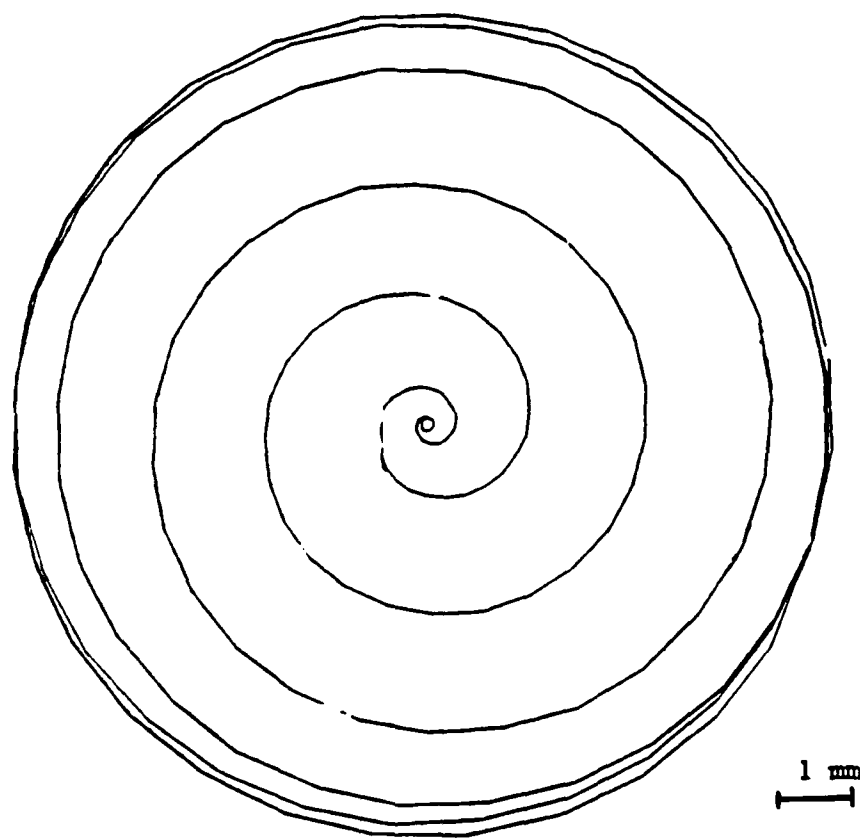


Figure 3-1: Electron orbit in an ideal axial and wiggler magnetic field.  $B_z=7$  kG,  $B_w=500$  gauss,  $k_w=0.893$ ,  $\gamma=4$

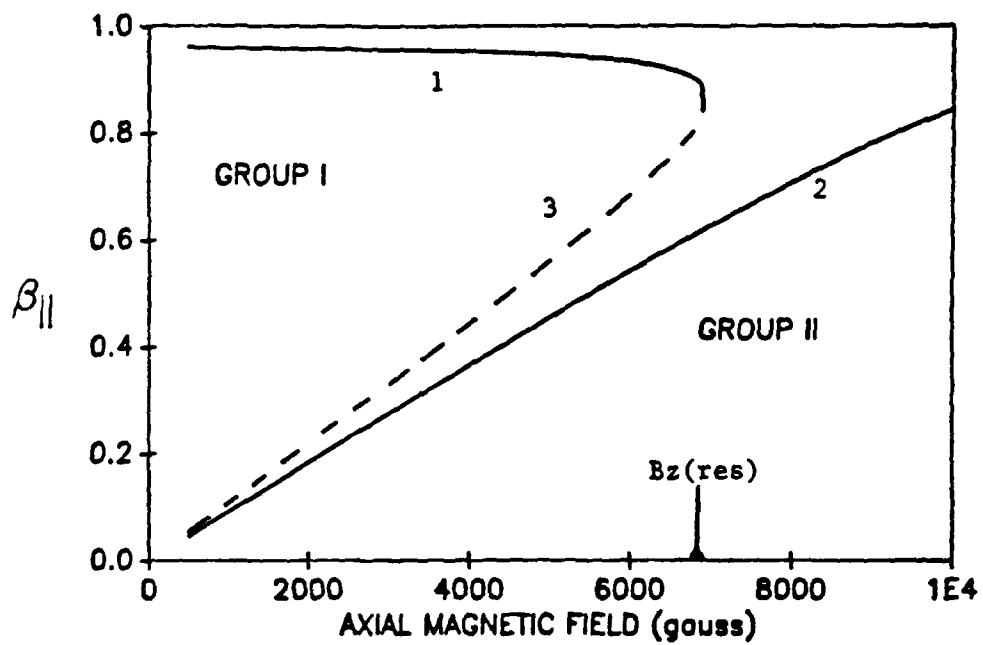


Figure 3-2: Axial velocity versus axial magnetic field.  $\gamma=3.8$   $B_w=850$  gauss,  $\lambda_w=4.06$  cm.

device is fixed, the wiggler itself was modified to facilitate experiments involving both types of orbits. The group I orbits were generated in a wiggler with period  $\lambda_w = 4.06$  cm ( $k_w = 1.55$  cm $^{-1}$ ) and the group II orbits were generated in a wiggler with period  $\lambda_w = 7.00$  cm ( $k_w = .898$  cm $^{-1}$ ).

### 3.3 Realistic Electron Trajectories - Three Dimensional Model

A physically realizable field that satisfies  $\vec{\nabla} \cdot \vec{B}_w = 0$  and  $\vec{\nabla} \times \vec{B}_w = 0$  will necessarily have a radial dependence. Solving Maxwell's equations for the case of a helical wiggler composed of infinitely thin wires and neglecting higher order spatial harmonics results in the following field configuration (for  $r < b$ ):

$$\vec{B} = \hat{z}B_z + 2B_w [\hat{r}I_1'(k_w r) \cos(\phi - k_w z) - \hat{\phi} \frac{I_1(k_w r)}{(k_w r)} \sin(\phi - k_w z) + \hat{z}I_1(k_w r) \sin(\phi - k_w z)] \quad (3.6)$$

where  $I_1$  is the modified Bessel function. This equation is the same as equation 2.13 with harmonic number  $p=1$ . The field strength  $B_w$  of equation 3.6 on axis is

$$B_w = \frac{\mu_0 i b k_w^2}{\pi} K_1'(k_w b) \quad (3.7)$$

where  $i$  is the current flowing in the wires of the helix and where  $b$  is the radius of the winding.

The electron trajectories are determined in the same manner as in the one dimensional model. The magnetic field specified by equation 3.6 is input into the momentum equation 3.3 and the normalized amplitudes of the velocity components are determined as  $\beta_{\parallel} = \text{constant}$  and

$$\beta_{\perp} = \frac{\beta_{\parallel} 2\Omega_w I_1(\chi)/\chi}{k_w \beta_{\parallel} c - \Omega_c - 2\Omega_w I_1(\chi)} \quad (3.8)$$

where  $\chi = \beta_{\perp}/\beta_{\parallel} = \pm k_w r$  is the normalized size of the orbit. The (+) sign is for the group I orbits and the (-) sign is for the group II orbits. When the velocity relation 3.8 is combined with the energy relation 3.2, the velocity components can be uniquely determined.

This normalization parameter  $\chi$  is used in the experiment to measure the beam  $\alpha \equiv \beta_{\perp}/\beta_{\parallel}$  which is proportional to the radial displacement of the beam from the axis ( $\alpha = k_w r$ ). As discussed in chapter 2, a current probe can be positioned at any  $z$  location. When an electron beam is intercepted by the probe, it will darken a piece of thermal paper glued to the probe. Figure 3-3 shows the burn marks on the thermal paper. The probe is placed at a particular  $z$  position and the beam is allowed to strike the thermal paper. The probe is then moved one centimeter and the beam allowed to strike the probe again. This is repeated over a distance equal to the wiggler winding period. A shot is taken with the wiggler field off in order to mark the center. The distance  $r$  between the center spot and the individual spots at various  $z$  positions is then measured. Since  $\alpha = \beta_{\perp}/\beta_{\parallel} = k_w r$ , then  $\alpha$  can be determined.

The field given in equation 3.6 (with 3.7) was used as an initial basis for the design of the wiggler. In order to minimize the amount of temperature that the wiggler field imparts to the beam, three effects were taken into account: the off-axis trajectory perturbations inside the wiggler; the effect of termination of the wiggler field; and the effect of dc space charge on the beam. Each effect is discussed below.

### 3.3.1 Off Axis Trajectory Effects

Perturbations of the electron trajectories are the result of two factors. The first is the fact that equation 3.6 neglects higher harmonics of the wiggler field which can become dominant as the electron trajectories approach the wiggler windings (i.e.  $r \simeq b$ ). The second is the fact that in practical systems the beam of electrons has some finite thickness and hence most of the electrons are not axis centered. This causes their orbits to not be purely helical.

As was shown in section 2.2.5, both the group I and II wigglers were designed to avoid the effects of the field harmonics. Since the value of  $k_w r < 1$ , use can be made of equation 3.6 to specify the magnetic field. Those electrons that have off-axis trajectories oscillate about some mean values of velocity denoted by  $\langle \beta_{\perp} \rangle$

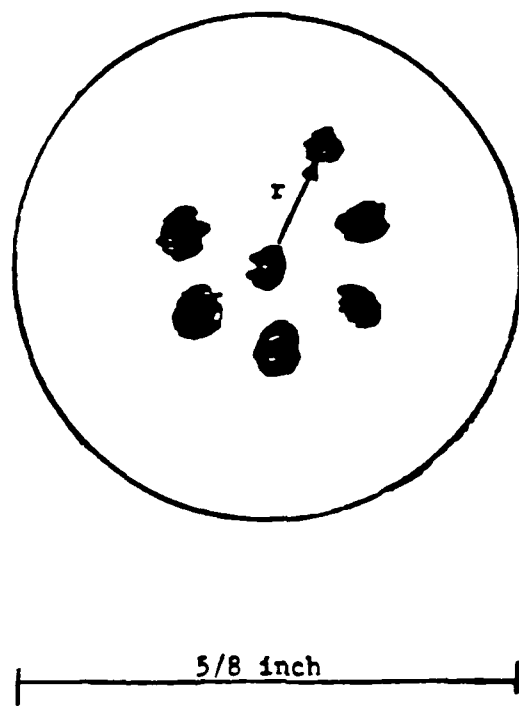


Figure 3-3: Thermal paper method of determining  $\alpha$ .  $B_z=7.4$  kG,  $B_w=940$  gauss,  $\gamma=2.75$ ,  $k_w=0.897$ . This series of shots is for  $z=37$  to  $43$  cm.

and  $\langle \beta_{\parallel} \rangle$ . Fajans [45] has shown that a good approximation for  $\langle \beta_{\perp} \rangle$  is

$$\frac{\langle \beta_{\perp} \rangle}{\langle \beta_{\parallel} \rangle} = \frac{2\Omega_w I_0(k_w r_g) I_1(\chi) / \chi}{k_w \langle \beta_{\parallel} \rangle c - \Omega_c - 2\Omega_w I_0(k_w r_g) I_1(\chi)} \quad (3.9)$$

where  $r_g$  is the displacement of the electron from the axis (also called the guiding center of the electron orbit). Note that the only difference between equations 3.8 and 3.9 is the presence of the  $I_0(k_w r_g)$  terms. Since the beam radius in this experiment is .32 cm and the waveguide radius is .79 cm, the maximum  $r_g$  is  $r_g(max) = .47$  cm. For the group I wiggler,  $k_w r_g(max) = .73$  and for the group II wiggler,  $k_w r_g(max) = .42$ . Both of these values represent less than 1% deviation of equation 3.9 from equation 3.8. For this reason, equation 3.8 is used in the analysis of the beam dynamics and in the design of the experiment.

### 3.3.2 Effects of Wiggler Termination

In the early 1980s it was found [46,38] that finite termination of a helical wiggler could result in large magnetic field spikes at the end of the wiggler. In this experiment, entrance disturbances have been minimized by tapering the wiggler field entrance, however, the beam must exit the wiggler field into the CARM interaction region. In doing so, it must not increase its temperature and must retain its perpendicular velocity. To accomplish this, the wiggler is terminated in a nonadiabatic manner by means of a shorting ring. (If the wiggler were terminated adiabatically, as in the uptaper, the majority of the perpendicular velocity generated would be lost.) Therefore, the second basis for wiggler design was the elimination of the effect of the end spike due to the finite termination of the wiggler.

As was shown in section 2.2.5, there is a potential for a large spike in the perpendicular component of the wiggler field if the value of  $b/\lambda_w > 0.6$ . Simulations of electron trajectories for the case of the two wigglers shown in figure 2-16 predict a 36% increase in energy spread for the case of the wiggler with the end spike over the wiggler without an end spike. Wigglers without end spikes are used in this experiment.

### 3.3.3 Effect of Space Charge on the Beam

A final parameter that must be analyzed is the effect of the beam dc space charge on the trajectory of the beam through the system. The ac space charge can possibly effect the CARM interaction itself, however no satisfactory theory of the ac space charge effect exists at this time. The dc effect can be broken into two portions: the radial force due to the electrostatic repulsion and the self magnetic field due to the current of the beam.

The steady state momentum equation

$$\vec{v} \cdot \nabla \vec{p} = -e(\vec{E} + \frac{\vec{v}}{c} \times \vec{B}) \quad (3.10)$$

where  $\vec{p}$  and  $\vec{v}$  are the macroscopic beam momentum and velocity, yields the energy balance

$$\frac{m\gamma(r)v_{\perp}^2(r)}{r} - e[E_r + \frac{v_{\perp}}{c}(B_z + B_z^s) - \frac{v_{\parallel}}{c}B_{\perp}] = 0 \quad (3.11)$$

where  $B_z^s$  is the axial diamagnetic self field and  $B_{\perp}$  is the perpendicular self magnetic field. The first term of equation 3.11 is the outward centrifugal force, the second term is the outward repulsion of the electric field due to the beam space charge and the third and fourth terms are the constraining forces of the magnetic fields.

Davidson [25] has shown that the dc self fields of the electron beam can be neglected and the beam considered tenuous if

$$1 \gg 2\gamma \frac{\omega_{p0}^2}{\Omega_{e0}^2} - 2\gamma \frac{\omega_{p0}^2}{\Omega_{e0}^2} \beta_{\parallel}^2. \quad (3.12)$$

The first term on the right hand side is a result of the defocusing effect of the radial self electric field and the second term is the result of the focussing effect of the self magnetic field. The right hand side of equation 3.12 is only 3.4% and therefore the dc self fields are neglected in this experiment.

In addition, the beam dc space charge can effect the CARM interaction. For electron beams of sufficient current density, the oscillatory motion of the beam due to the self fields can have an effect on the stability of the CARM interaction. This leads to a more restrictive condition. It has been shown by Davidson [25] that the space charge effects can be neglected if

$$(\frac{\omega_{p0}}{\Omega_{e0}})^2 \gamma < 0.2. \quad (3.13)$$

The left-hand side of equation 3.13 is 0.13 and therefore dc space charge is considered to have no significant effect on the CARM interaction. As a result of this analysis, dc space charge effects have been ignored in numerical simulations of both the beam dynamics and the CARM interaction.

### 3.4 Numerical Simulations

In the numerical computations of beam dynamics the Biot-Savart law

$$d\vec{B} = \frac{\mu_0 I d\vec{l} \times \vec{r}}{4\pi r^3} \quad (3.14)$$

is used to generate the magnetic field. The beam is treated as a group of up to 1024 macroparticles with a given spatial and velocity distribution and integration is accomplished over sufficiently small steps through the computer simulation. Use was made of the COILE [41] program that divided each wire of a bifilar helical wiggler and its loop terminations into small segments of current as an approximation to the actual magnet. This magnetic field (together with the solenoidal component) is then used in the TRAJ6.10 [41] program and the trajectory of each macroparticle, as determined by the values of the magnetic field at each location, is then computed from the Lorentz force law in a step-by-step manner over sufficiently small  $\Delta z$ . The effect on beam velocity and velocity spread by spinning up the beam in the realistic models of the group I and II wigglers is then determined.

#### 3.4.1 Group I Orbit Simulations

Figure 3-4 shows the perpendicular velocity generated in the group I wiggler as a function of the wiggler strength for various axial fields. As the axial field approaches the field corresponding to the transition field ( $B_z(res) = 9.8$  kG), between group I and II orbits, perpendicular velocity rises quickly. Figure 3-5(a) shows the growth in  $\alpha$  as a function of  $z$  for the operating parameters  $B_z = 5.4$  kG and  $B_w = 840$  G. Note that there is a smooth rise due to the adiabatic uptaper of the wiggler and that the  $\alpha$  that is generated remains constant at the peak value after the wiggler has



# GROUP I ORBITS

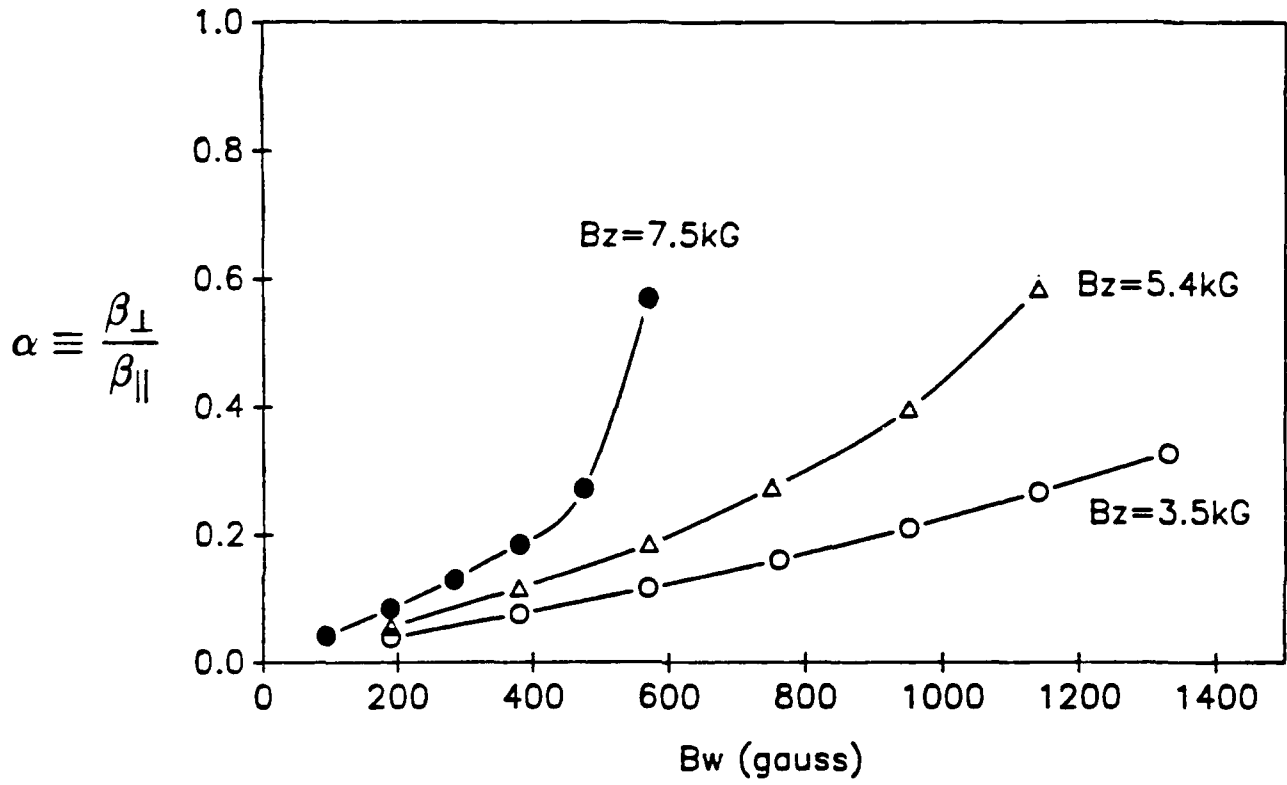


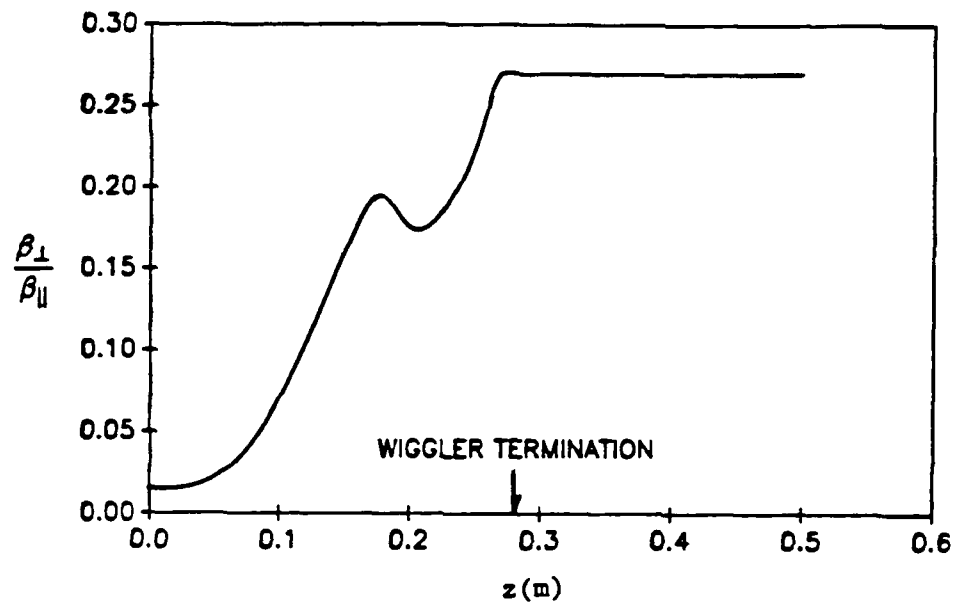
Figure 3-4:  $\alpha \equiv \beta_{\perp}/\beta_{\parallel}$  versus wiggler strength for the group I wiggler ( $B_z(\text{critical})=9.8$  kG,  $\gamma=4$ , and  $\lambda_w=4.06$  cm).

been terminated. The calculated energy spread  $\Delta\gamma_{\parallel}/\gamma_{\parallel}$  that has been generated is 5.6% (space charge effects have been neglected). The growth of the energy spread as the beam transits the wiggler region is shown in figure 3-5(b). Note that the 4.4% energy spread generated by the diode was input into this analysis and can be seen at the  $z=0$  position in figure 3-5(b).

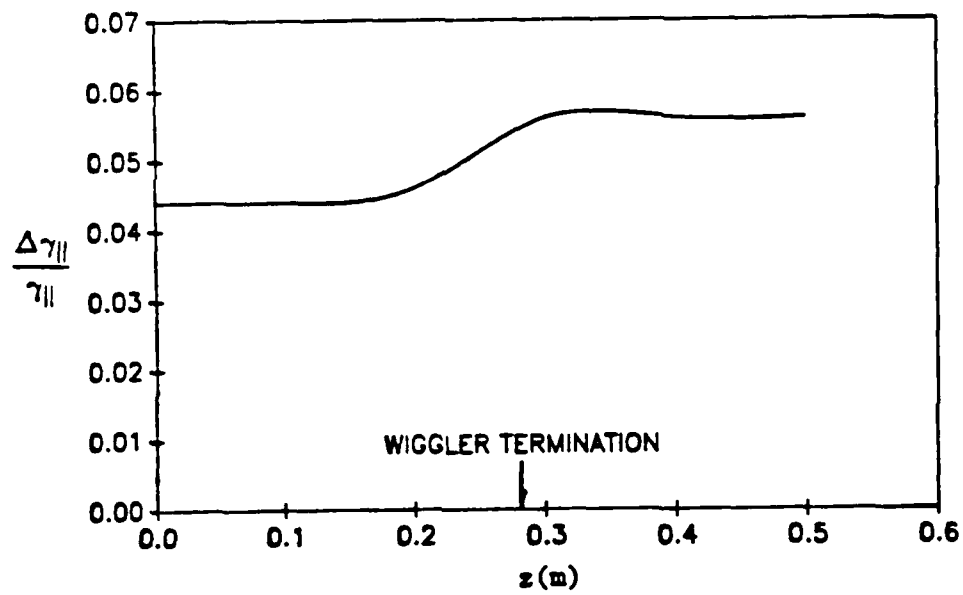
Figure 3-6 shows the simulated beam spot after the exit from the wiggler region at the start of the CARM region. Three spots have been superimposed which represent the beam at successive distances  $z$  separated by thirds of a cyclotron orbit ( $l_c=7.3$  cm). A notch has been superimposed on the particle distribution to show that the beam rotation about its own center is minimal. The values of the average beam offset guiding center radius  $\langle r_g \rangle = 0.16$  cm and the average Larmor radius  $\langle r_L \rangle = 0.35$  cm can be seen. These values of beam offset, Larmor radius, and energy spread are the values that are input to the simulation of the CARM interaction as presented in chapters 4 and 5.

Significant increases in beam temperature arise as the combination of wiggler and solenoidal fields approach the resonant field (see equation 3.8). As the beam transits the wiggler region and proceeds into the CARM interaction region it may become dispersed in space and momentum. This spatial dispersion is graphically shown in figure 3-7 for the case of  $B_z=6.2$  kG and  $B_w=840$  G. Note that the beam is now spread over more of the waveguide cross section. The energy spread is now nearly twice as large as the case of the operating parameters, for only a 13% change in the axial field. Analysis of the beam at  $B_z=6.2$  kG and  $B_w=840$  G show  $\langle r_g \rangle = 0.13$  cm,  $\langle r_L \rangle = 0.42$  cm, and  $\Delta\gamma_{\parallel}/\gamma_{\parallel} = 9.4\%$ . These values have been input into the CARM simulation and are compared with experimental data taken as part of the power maximization process shown in chapter 5.

A beam that is dispersed and off-center will cause a decrease in the efficiency of the CARM interaction. An off center beam can be brought to the center of a waveguide through magnetic steering or by modifying the waveguide so that the beam exits the wiggler on the axis of the interaction region. A beam that is dispersed and with inordinately high beam temperature cannot be corrected. As will be seen in chapter 5, field setting corresponding to figure 3-6 resulted in 8.9 dB more rf



(a)



(b)

Figure 3-5: (a)  $\alpha$  as a function of  $z$  and (b)  $\Delta\gamma_{\parallel}/\gamma_{\parallel}$  as a function of  $z$  for the group I wiggler ( $B_z=5.4$  kG,  $B_w=840$  gauss).

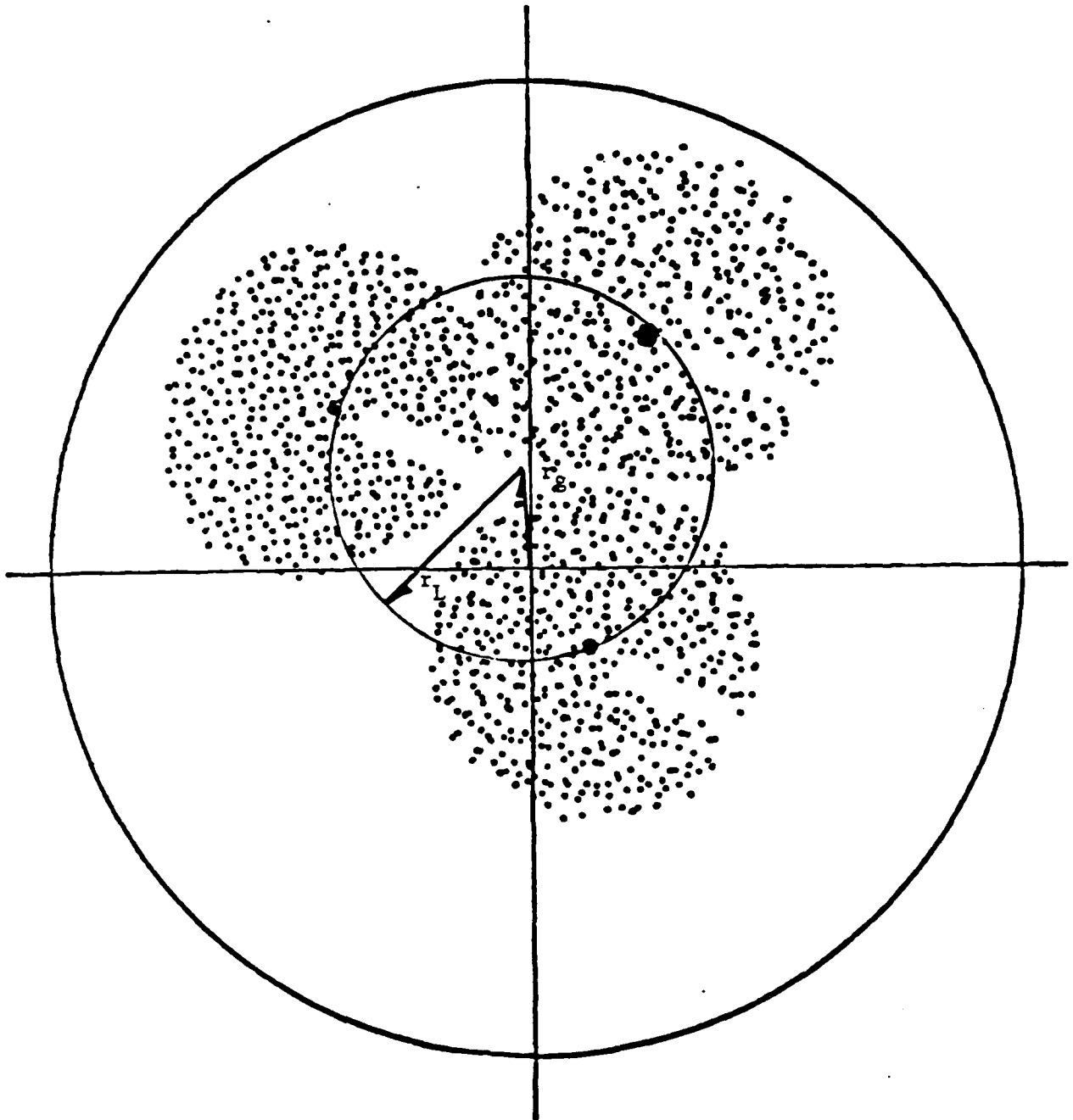


Figure 3-6: Beam spots at three successive axial positions, separated by a third of a cyclotron orbit, superimposed to show the beam offset guiding center  $\langle r_g \rangle$  and the average Larmor radius  $\langle r_L \rangle$  of the beam.  $B_z=5.4$  kG and  $B_w=840$  G.

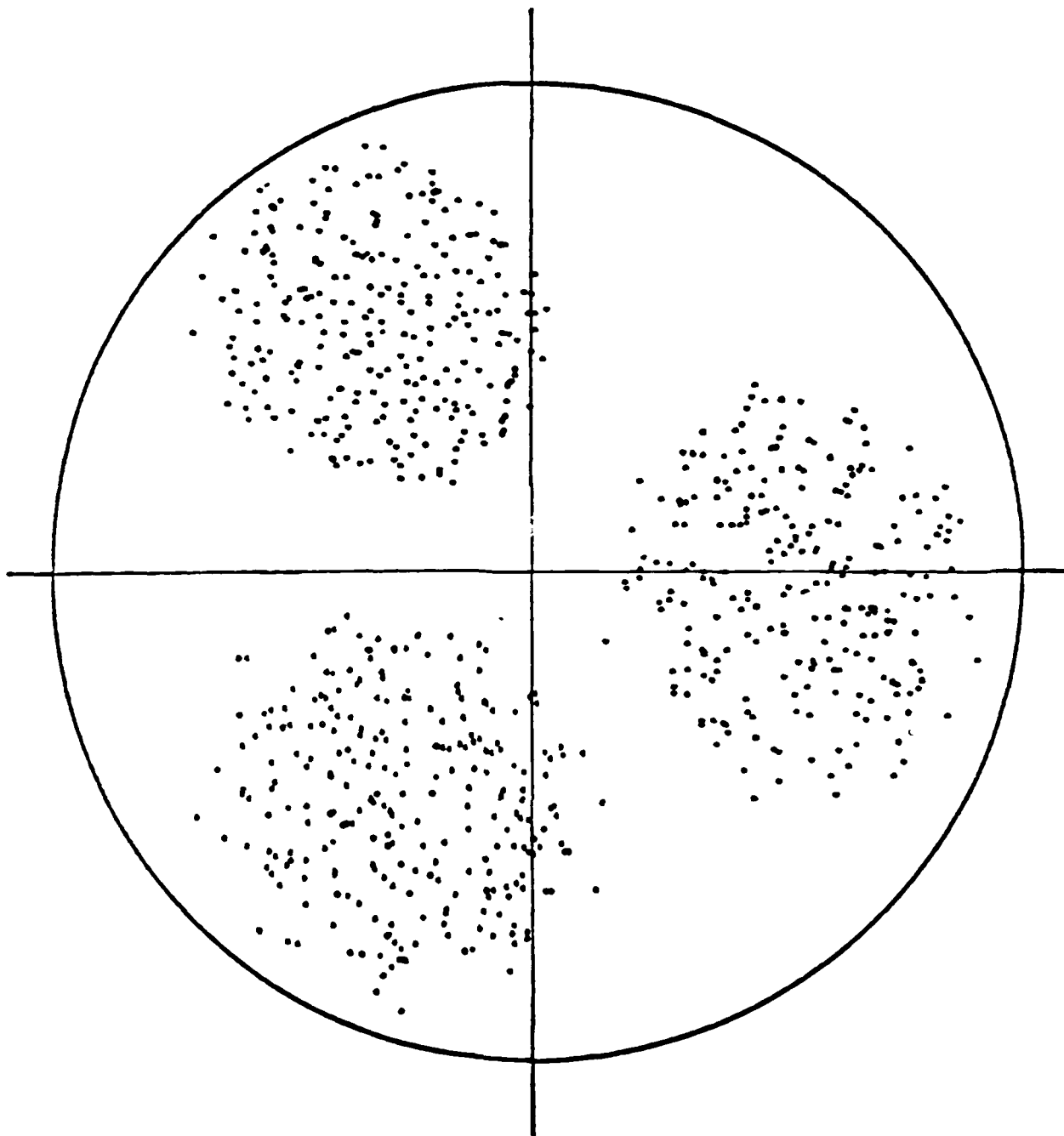


Figure 3-7: Increased spatial dispersion of the beam as the operating field nears magnetoresonance. Three beam spots representing the beam at successive thirds of a cyclotron orbit are shown.  $B_z=6.2$  kG and  $B_w=840$  G.

power output from the CARM than that corresponding to figure 3-7.

The simulation of the group I orbits has shown that there is an increase in the beam temperature due to the action of the beam in the wiggler region. When the fields approach the magnetoresonance, a significant increase in beam temperature is seen. Inside the wiggler, the perpendicular velocity of the beam reaches some maximum value and then exits the wiggler with the same perpendicular velocity.

### 3.4.2 Group II Orbit Simulations

A similar analysis has been completed for the group II wiggler, however significant differences appear. Figure 3-8 shows the perpendicular velocity generated as a function of wiggler field for various axial fields. There is a significant amount of structure in these curves which does not appear in figure 3-4. This is due, in part, to the fact that the group II wiggler operates closer to the magnetoresonance ( $B_z=5.6$  kG) than the group I wiggler. Far from the magnetoresonance ( $B_z=9.0$  kG) there is a linear relationship between  $\alpha$  and wiggler field strength. However, as  $B_z$  approaches the magnetoresonant value, large fluctuations are seen. To analyze the effects of spinning the beam up in group II orbits, two sets of field configurations are studied corresponding to operation at the experimental field values and at field values nearer to the magnetoresonance.

The first set of field configurations presented here are those that correspond to the operating parameters of the group II wiggler experiment. Figure 3-9 shows the growth in  $\alpha$  as a function of  $z$  corresponding to the operating parameters ( $B_z=6.1$  kG,  $B_w=490$  G). Of significance is the fact that the value of  $\alpha$  saturates prior to termination of the wiggler and that a large fluctuation in  $\alpha$  has begun at  $z=35$  cm. The fixed position of the wiggler termination then cuts off the action of the wiggler and the  $\alpha$  existing at that point remains constant. In this example there is a loss of 50% of the maximum value of  $\alpha$  and an energy spread of  $\Delta\gamma_{||}/\gamma_{||} = 4.5\%$ .

Figure 3-10 shows a superposition of three beam spots that represent the beam at successive thirds of a cyclotron orbit at the beginning of the CARM region. The average guiding center  $\langle r_g \rangle = 0.16$  cm and the average Larmor radius  $\langle r_L \rangle = 0.42$  cm

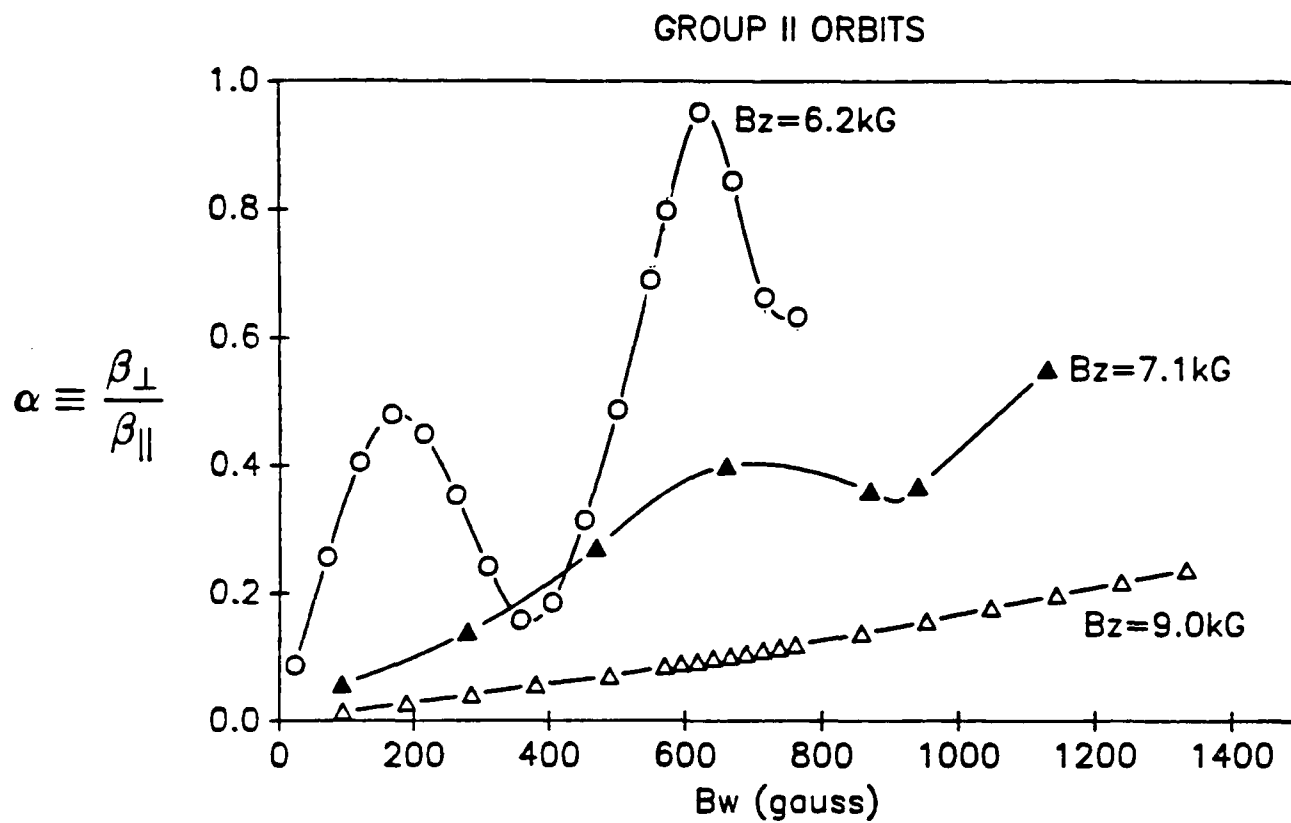


Figure 3-8:  $\alpha \equiv \beta_{\perp}/\beta_{\parallel}$  versus wiggler strength for the group II wiggler ( $B_z(\text{critical})=5.6$  kG,  $\gamma=4$ , and  $\lambda_w=7.0$  cm).

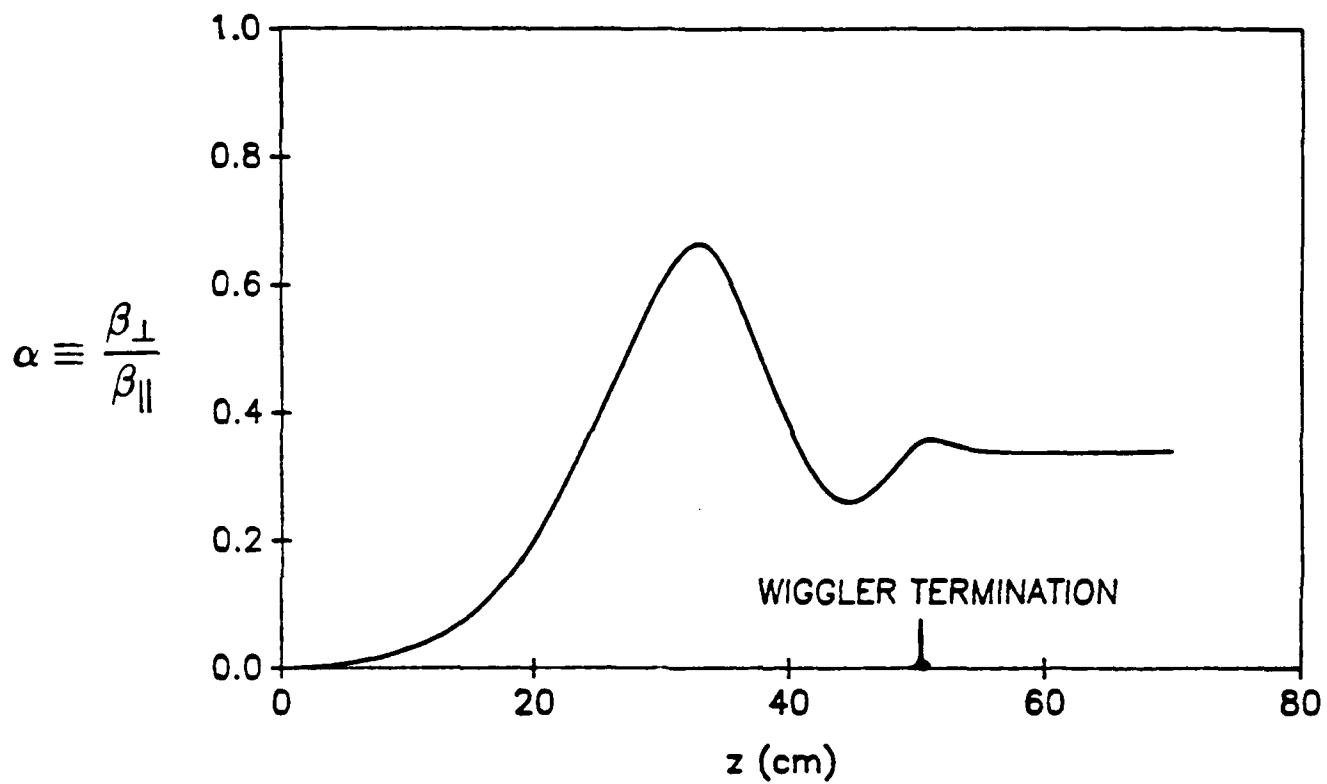


Figure 3-9:  $\alpha \equiv \beta_{\perp}/\beta_{\parallel}$  as a function of  $z$  for  $B_z=6.1$  kG and  $B_w=490$  G for the group II wiggler.



are shown. Note that the beam strikes the wall of the waveguide in this simulation. Current measurements of the actual experiment show that only 65% of the current into the wiggler reaches the midpoint of the CARM interaction region.

A similar analysis is been done for the second set of field configurations,  $B_z=5.8$  kG and  $B_w=490$  G, which is a region closer to the magnetoresonance. Figure 3-11 shows the growth of  $\alpha$  as a function of  $z$ . A three beam spot picture is shown in figure 3-12. It can be readily seen that the spatial beam dispersion shown in figure 3-12 is considerably greater than that for the operating parameters. The energy spread is also twice as high ( $\Delta\gamma_{\parallel}/\gamma_{\parallel}=8.9\%$ ). Field settings corresponding to figure 3-10 result in a measured power 3.5 dB greater than for the field settings of figure 3-12. (see chapter 5)

The simulation of the group II orbits reveals three important findings. First, depending upon the fields selected, there is a potential for a large increase in beam temperature due to wiggler action. Second, due to a smaller  $k_w$ , the beam deviates significantly from the center of the waveguide. This can cause the beam to strike the waveguide wall resulting in a loss of current. Third, depending on where the wiggler is terminated, there is a potential for significant loss in the peak  $\alpha$  generated in the wiggler.

### 3.5 Conclusion

This numerical analysis has been undertaken to show that both group I and II wigglers can be utilized to produce perpendicular velocity in a beam that can then be delivered to a CARM interaction region. Beam dynamics in a combined axial and wiggler magnetic field are highly nonlinear. This makes it difficult for the experimenter to fix the value of one field and 'tune' the value of the other. The use of numerical simulations to aid in the study of beam dynamics becomes increasingly important.

This chapter has formulated an effective model of the combined axial and wiggler magnetic field and for beam trajectories through that field. The purpose of the model is to understand the dynamics of the beam in order to calculate the power

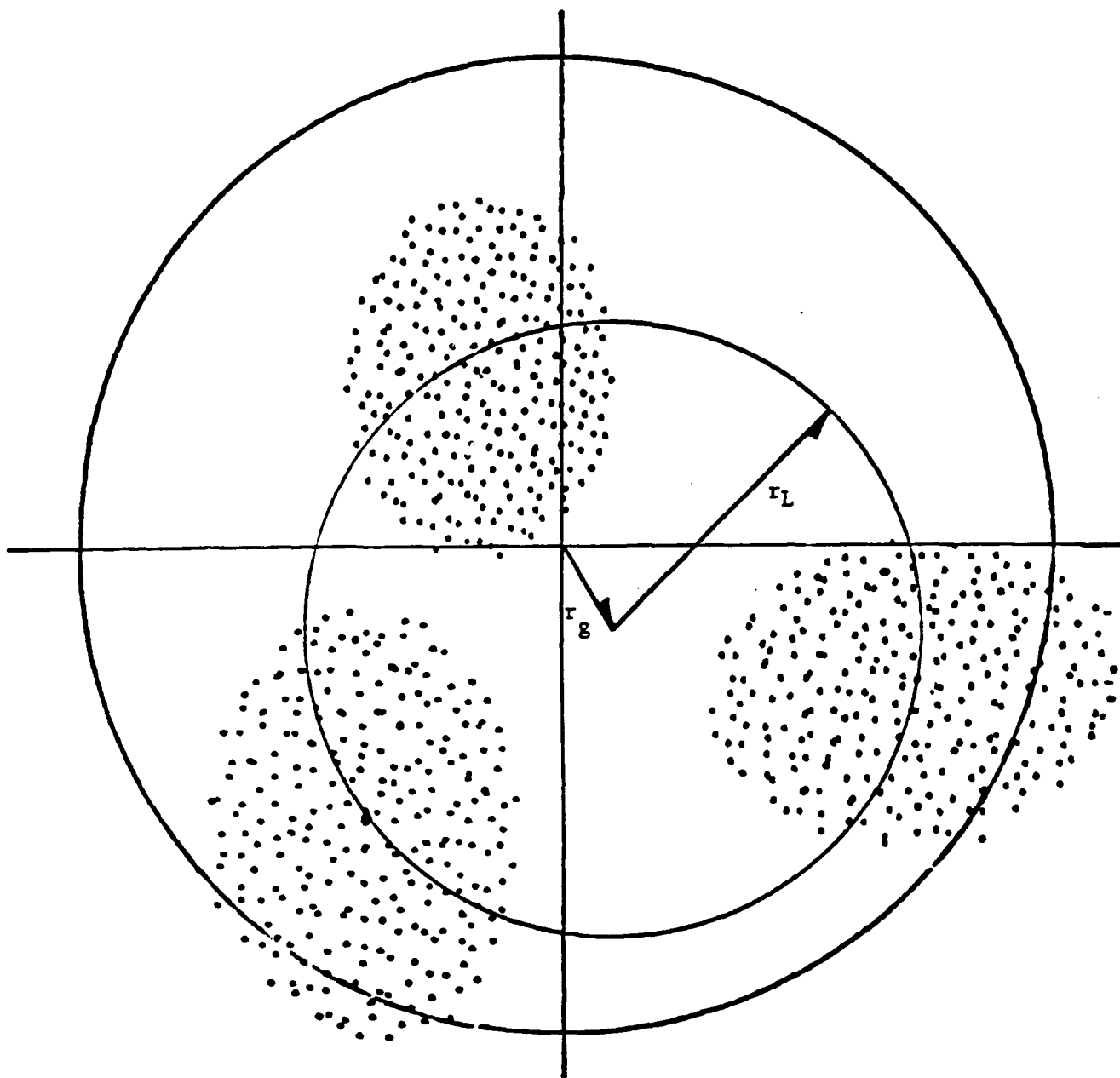


Figure 3-10: Three beam spots, representing the beam at successive thirds of a cyclotron orbit, for the group II wiggler for the fields  $B_z=6.1$  kG and  $B_w=490$  G.

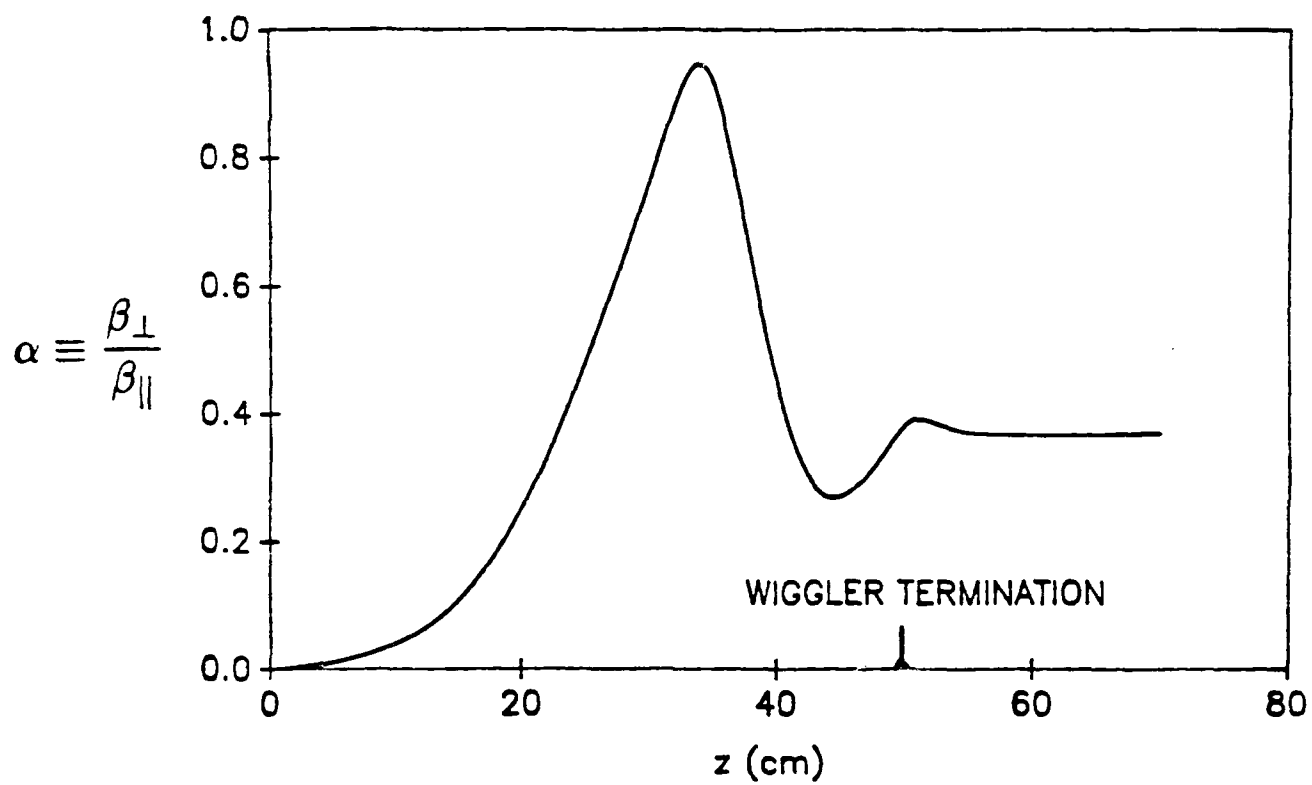


Figure 3-11: Growth of  $\alpha$  vs  $z$  for  $B_z=5.8$  kG and  $B_w=490$  G, group II wiggler.

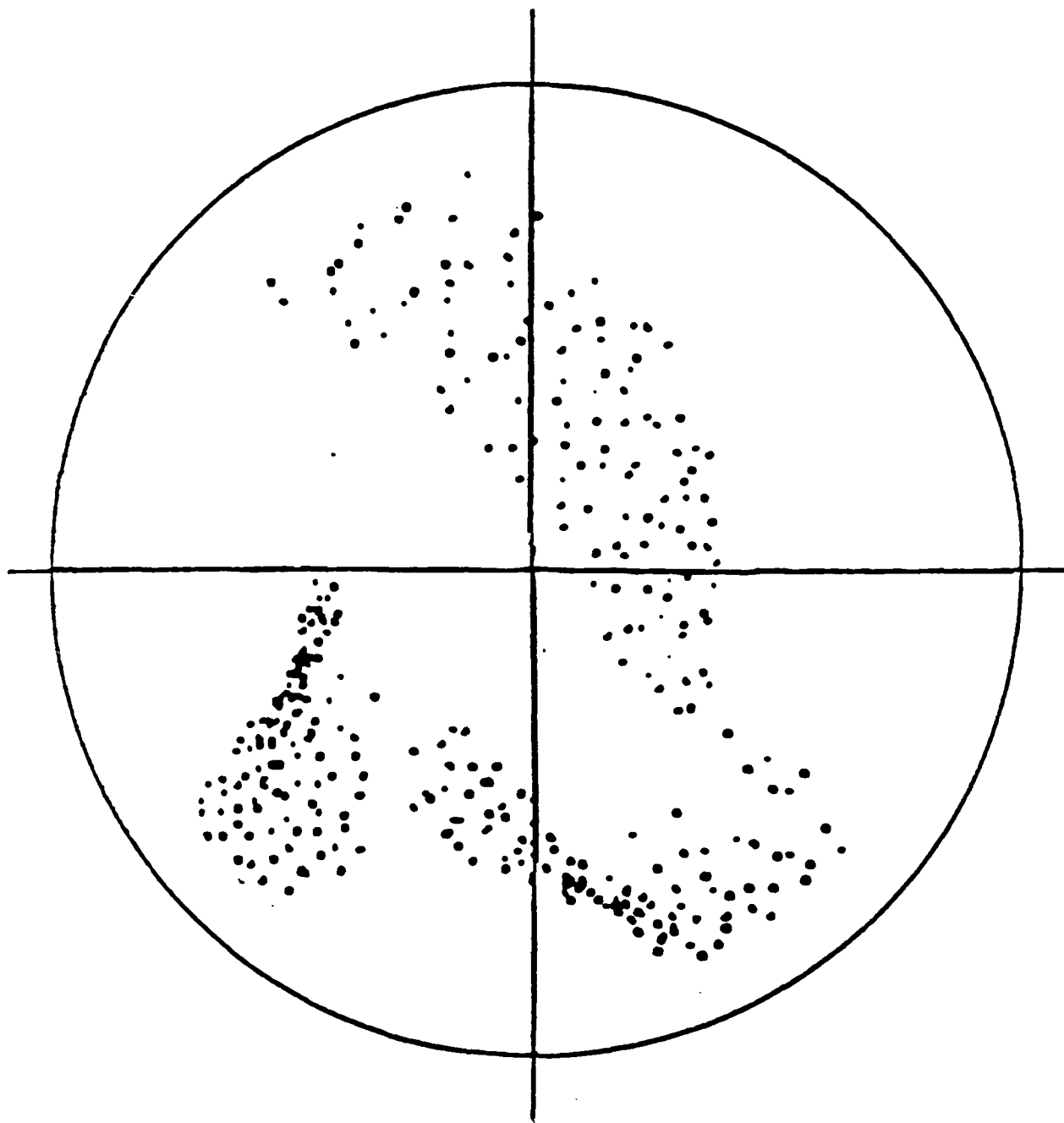


Figure 3-12: Three Spot representation for  $B_z=5.8$  kG and  $B_w=490$  G.

Table 3.1: Wiggler Field Results

	Group I Wiggler	Group II Wiggler
Period $\lambda_w$	4.06 cm	7.00 cm
Winding Radius $b$	0.90 cm	2.6 cm
Resonant Axial Field	9.8 kG	5.6 kG
Operating Axial Field	5.4 kG	6.1 kG
Operating Wiggler Field	840 G	490 G
$\alpha$ Calculated	.27	.30
$\alpha$ Measured	.3 $\pm$ .1	.35 $\pm$ .08
$\Delta\gamma_{  }/\gamma_{  }$ Calculated	5.6%	4.5%

extracted from the beam in the CARM interaction region. These calculations are presented in chapter 4. Two wigglers have been presented and discussed. Table 3.1 is a compendium of the parameters of the beam that exit from the two wigglers according to the model presented. The experimental values shown are the result of witness plate measurements and are included to show the effectiveness of the model.

The values of  $\alpha$  and energy spread will be used as starting points in an analysis of the potential for generation of rf power in the CARM interaction region to be presented in Chapter 4. Since the CARM interaction does not involve the use of a wiggler field as a free electron laser does, there is a wider latitude in the choice of devices used to generate beam perpendicular velocity for use by the CARM. As will be seen, rf power can be generated using electrons that have been spun up in both group I and II orbits.

## Chapter 4

# Cyclotron Autoresonance Maser Theory

### 4.1 Introduction and Outline

If an electron moves in a homogeneous magnetic field, it may be at the cyclotron resonance with an electromagnetic wave travelling with it. When the phase velocity  $v_{ph} = \omega/k_{\parallel}$  of the wave is near light speed and the axial velocity of the beam is in the direction of propagation of the wave, a large Doppler upshift of the radiated frequency is possible.

This chapter discusses the interaction mechanism of the cyclotron autoresonance maser (CARM). The derivations of the CARM interaction in free space and in a waveguide have been published extensively [9,15,16,47,10,14]. The linear theory of the CARM interaction in a cylindrical waveguide is presented. These equations are the point of departure for the numerical simulations used in this work which analyze the CARM interaction both in the linear growth regime as well as after power saturation. The method of numerical analysis is presented here in detail.

## 4.2 The Linear Characteristics of the CARM Interaction

This section presents the linear CARM dispersion relation for a  $TE_{11}$  mode in a cylindrical waveguide as derived by A. Fliflet [15]. The growth rate of the CARM interaction in the linear regime as well as the dependence of the growth rate on parameters available for manipulation in the experiment are shown. The linear dispersion relation must be analyzed in order that the onset of an absolute instability at the lower intersection of figure 1.1(b) is avoided. This determination is made by applying a Bers-Briggs pinch point analysis to the dispersion relation. The results of that analysis are presented in this section.

Only the  $TE_{11}$  mode is discussed here as it is the mode of the CARM experiment of this work. The effect on the growth rate of the interaction by the inclusion into the analysis of finite Larmor radius, detuning, and waveguide loss are presented.

Since the electron trajectory seldom positions the electron at the center ( $r=0$ ) of the waveguide, an electron/waveguide geometry must be defined. This geometry is used in both the theoretical and numerical simulation portions of this work. The geometry of interaction is shown in figure 4-1. The Larmor radius  $r_L = p_{\perp}/m\Omega_{ce}$  and the guiding center of the electron orbit are related by

$$r_g^2 = r^2 + r_L^2 - 2rr_L \sin(\phi - \theta). \quad (4.1)$$

In this experiment  $\langle r_L \rangle > \langle r_g \rangle$ .

The linear dispersion relation for the  $TE_{11}$  mode for the first harmonic is [15]

$$\frac{\omega^2}{c^2} - k^2 - k_{\perp}^2 = \frac{4\pi e^2}{c^2 r_w^2 (1 - 1/k_{\perp}^2 r_w^2) J_1^2(k_{\perp} r_w) m} \int_0^{r_w} r_g dr_g \int_0^{\infty} p_{\perp}^2 dp_{\perp} \int_{-\infty}^{+\infty} dp_{\parallel} \quad (4.2)$$

$$J_0(k_{\perp} r_g) J_1'(k_{\perp} r_L) \frac{F_{11}^{TE}(r_g, p_{\perp}, p_{\parallel})}{\gamma(\omega - kv_{\parallel} - \Omega_c)}$$

where

$$F_{11}^{TE}(r_g, p_{\perp}, p_{\parallel}) = J_0(k_{\perp} r_g) J_1'(k_{\perp} r_L) \left[ \left( \omega - \frac{kp_{\parallel}}{\gamma m} \right) \frac{\partial f_0}{\partial p_{\perp}} + \frac{kp_{\perp}}{\gamma m} \frac{\partial f_0}{\partial p_{\parallel}} \right]. \quad (4.3)$$

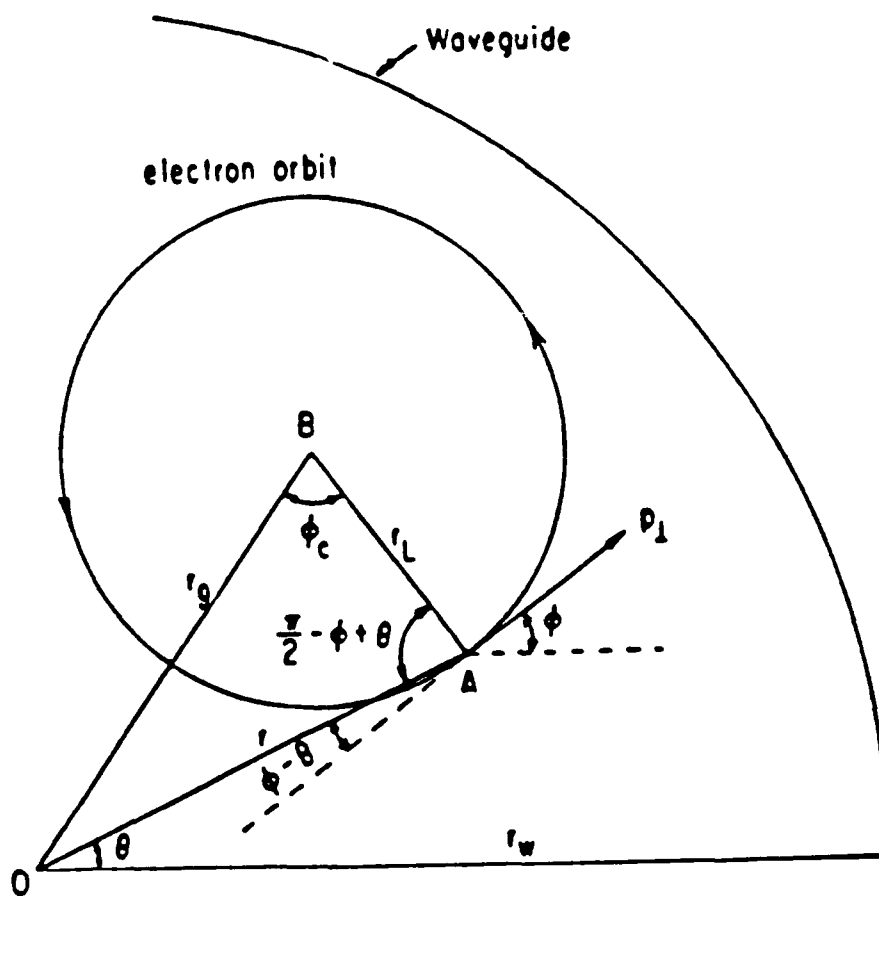


Figure 4-1: The geometric relationship between the Larmor radius  $r_L$  and the guiding center  $r_g$  of the electron as it orbits in the waveguide.



The distribution function  $f_0$  that specifies the system must be determined. While the experiment does not use a cold beam, several interesting points can be made from using the cold beam distribution function ( $N$  is the normalization constant)

$$f_0 = N \frac{\delta(p_{\perp} - p_{\perp 0}) \delta(p_{\parallel} - p_{\parallel 0})}{2\pi p_{\perp 0}}. \quad (4.4)$$

The integration of the integral above (equation 4.2) with a cold beam distribution function results in the following dispersion relation

$$(\omega^2 - k_{\perp}^2 c^2 - k^2 c^2)(\omega - kv_{\parallel} - \Omega_c)^2 = -\frac{A_b}{\pi r_w^2} \frac{\omega_p^2}{\gamma(1 - 1/r_w^2 k_{\perp}^2) J_1^2(k_{\perp} r_w)} \left[ (\omega^2 - k^2 c^2) \beta_{\perp}^2 H_{11} - (\omega - kv_{\parallel})(\omega - kv_{\parallel} - \Omega_c) Q_{11} \right] \quad (4.5)$$

where

$$H_{11} = J_0^2(k_{\perp} r_g) J_1'(k_{\perp} r_L) \quad (4.6)$$

and

$$Q_{11} = 2J_0^2(k_{\perp} r_g) [J_1'^2(k_{\perp} r_L) + k_{\perp} r_L J_1'(k_{\perp} r_L) J_1''(k_{\perp} r_L)] \quad (4.7)$$

and  $A_b$  is the cross sectional area of the beam. Equation 4.5 is written in the coupled mode form with the left-hand side specifying the modes and the right-hand side specifying the coupling. This shows that at very low current ( $\omega_p^2 \simeq 0$ ), the roots represent the empty waveguide mode and the cyclotron beam mode.

The coupling term in equation 4.5 is critical in an analysis of the CARM interaction. As will be seen in the next section on numerical simulations, the inclusion of finite Larmor radius and offset guiding center effects is quite important in determining a growth rate and a total power comparable to the experimental values. As can be seen in equation 4.5, if  $r_L \rightarrow 0$ , then  $Q_{11} \rightarrow 2J_0^2(k_{\perp} r_g)(1/4)$ , and  $H_{11} \rightarrow J_0^2(k_{\perp} r_g)(1/2)$ , since  $J_n'(x) \rightarrow nx^{n-1}/2^n n!$  for  $x \rightarrow 0$ .

The effects due to wall loss can also be incorporated into the analysis with the following substitution [47]

$$k_{\perp}^2 \rightarrow k_{\perp}^2 \left[ 1 - (1 + i) \left( 1 + \frac{1}{k_{\perp}^2 r_w - 1} \frac{\omega^2}{\omega_c^2} \right) \frac{\delta}{r_w} \right] \quad (4.8)$$

where  $\delta$  is the skin depth of the conducting wall ( $\mu = 1$ ).

The spatial growth rate can be calculated by substituting  $\omega = \omega_r$  and  $k = k_r + ik_i$  into equation 4.5 and solving for  $k_i$  (to leading order)

$$k_i = \left[ \frac{\beta_{ph} \beta_{\perp}^2}{\beta_{\parallel}^2} \frac{A_b \omega_{p0}^2 k_{\perp} H_{11} (1 - \beta_{ph}^{-2})^{1/2}}{16(1 - 1/r_w^2 k_{\perp}^2) J_1(r_w k_{\perp}) \gamma \pi r_w^2} \right]^{1/3}, \quad (4.9)$$

where the phase velocity  $\beta_{ph} = \omega/c k_{\parallel}$ . This equation can be presented as the spatial growth rate in terms of dB/m

$$\Gamma(\text{dB/m}) = 7.5 \left[ \frac{\beta_{ph} \beta_{\perp}^2}{\beta_{\parallel}^2} \frac{A_b \omega_{p0}^2 k_{\perp} J_0^2(k_{\perp} r_g) J_1'^2(k_{\perp} r_L) (1 - \beta_{ph}^{-2})^{1/2}}{(1 - 1/r_w^2 k_{\perp}^2) J_1(r_w k_{\perp}) \gamma \pi r_w^2} \right]^{1/3}. \quad (4.10)$$

In the above equation (4.10), the effects of finite Larmor radius ( $r_L$ ) and offset guiding center ( $r_g$ ) are apparent since both  $J_0$  and  $J_1'$  decrease for increasing argument. As can be seen, the growth rate is proportional to the 2/3 power of  $\alpha$  and 1/3 power of the current as expected in the large gain, single particle regime in the absence of space charge effects.

Equation 4.9 suggests that the growth rate of the CARM interaction is zero for luminous ( $\beta_{ph} = 1$ ) waves. The growth rate is small, but non-zero, since the higher order terms neglected in equation 4.9 contribute to the growth rate for luminous waves.

This dispersion relation has been derived only for the case of the cold beam. The use of any distribution function other than the cold beam distribution function of equation 4.4, such as the following for a monoenergetic beam with a Gaussian spread in both parallel and perpendicular velocities

$$f(p_{\perp}, p_{\parallel}) = N \delta(\gamma - \gamma_0) \exp\left[-\frac{(p_{\parallel} - p_{\parallel 0})^2}{2(\Delta p_{\parallel})^2}\right] \exp\left[-\frac{(p_{\perp} - p_{\perp 0})^2}{2(\Delta p_{\perp})^2}\right] \quad (4.11)$$

( $N$  is the normalization constant), results in an equation that is most easily solved by numerical methods through a multiparticle simulation.

The experimental design must be a tradeoff between desired total power and adequate growth rate, since the latter is directly connected to the size of the device. Since the growth rate is a strong function of current,  $\alpha$ , phase velocity and waveguide geometry (see equation 4.9), tradeoffs must be made. These tradeoffs can result in a departure from the resonant frequency and can be analyzed through the use of

the detuning parameter. Detuning can be defined as a departure from the resonant frequency of equation 1.1 and written as

$$\Delta = \frac{\omega - \Omega_c - k_{\parallel} v_{\parallel}}{\omega} \quad (4.12)$$

where  $\Delta$  is the normalized detuning parameter. Since the relativistic cyclotron frequency  $\Omega_c$  is directly proportional to the axial magnetic field, the detuning can be varied by changing the value of the axial magnetic field. This cannot be simply accomplished in the actual experiment, however, since the axial field also surrounds the wiggler field and changes in the axial field will change the  $\alpha$  and velocity spread of the beam. As such a direct comparison between the detuning and the growth rate cannot be made.

Lastly, spatial growth of the instability does not occur forever with a realistic beam of particles. This is due to the fact that the particles which are initially uniformly distributed in phase at the start of the interaction, become bunched and release a net energy to the wave in the linear growth region, and eventually are trapped in a ponderomotive wave in the region of power saturation. These bunched particles alternately transfer energy to and from the wave. No additional power can be gained by increasing the interaction length of the experiment after saturation has occurred since the power output as a function of  $z$  simply oscillates between some maximum and minimum power value. This problem can be partially rectified by tapering the axial magnetic field strength after saturation occurs. The tapered field modifies the condition of the ponderomotive potential well. The beam particles can then continue to resonate (see chapter 1 on autoresonance) with the wave in a manner that releases a net energy to the wave over some interaction length. This will be seen graphically in the next section on numerical simulations.

#### 4.2.1 Pinch Point Analysis

In a CARM, an absolute instability can occur at the Doppler downshifted frequency. It is therefore necessary to analyze the stability of the CARM interaction in order to avoid the onset of this instability. Experimental parameters appropriate to the

convective instability at the Doppler upshifted frequency that defines the CARM interaction can then be selected. The stability analysis is accomplished by means of the Bers-Briggs pinch point method [48,49,50] for  $(\omega, \vec{k})$  in the region of the downshifted frequency. A pinch point is formed by the merging of  $k$ -plane images of the Laplace contour from above and below the real  $k$  axis as the Laplace contour is lowered toward the real  $\omega$  axis. The necessary and sufficient condition for the existence of an absolute instability is the existence of a pinch point in the complex  $k$  plane. Rewriting the dispersion relation (equation 4.5) as  $D(\omega, \vec{k}) = 0$ , the pinch points are the simultaneous solutions of this equation and  $\delta D(\omega, \vec{k})/\delta \vec{k} = 0$  for  $\text{Im}\omega > 0$ . The absolute instability is initiated at  $\text{Im}\omega = 0$ .

A numerical pinch point analysis has been made for the CARM in this experiment and the results of that analysis are shown in figure 4-2. The curves shown in figure 4-2 specify the region of onset of the absolute instability. Parameters to the lower left of the curves are regions where the absolute instability does not occur. The parameters used in this experiment are outlined in the rectangle to the left of the lowest curve. As can be seen the CARM in this experiment operates with a considerable margin of safety.

### 4.3 Numerical Simulations

This section presents the range of possible experimental outcomes resulting from manipulation of the available parameters through the use of a numerical code. The individual parameter analyses together yield the total possible outcomes of the experiment as presently configured, as well as indicating directions for improvement. The results of the beam transport analysis presented in chapter 3 are used as input into the simulations of this chapter.

The iterative process of designing a system begins with an analysis of the parameters available for manipulation in the experiment. Some parameters are fixed, for instance; the drive magnetron operates at 35 GHz, waveguides have relatively fixed radii, axial and wiggler magnets can only attain certain maximum fields, and beam quality and quantity are fixed by the acceleration device used. Some parameters

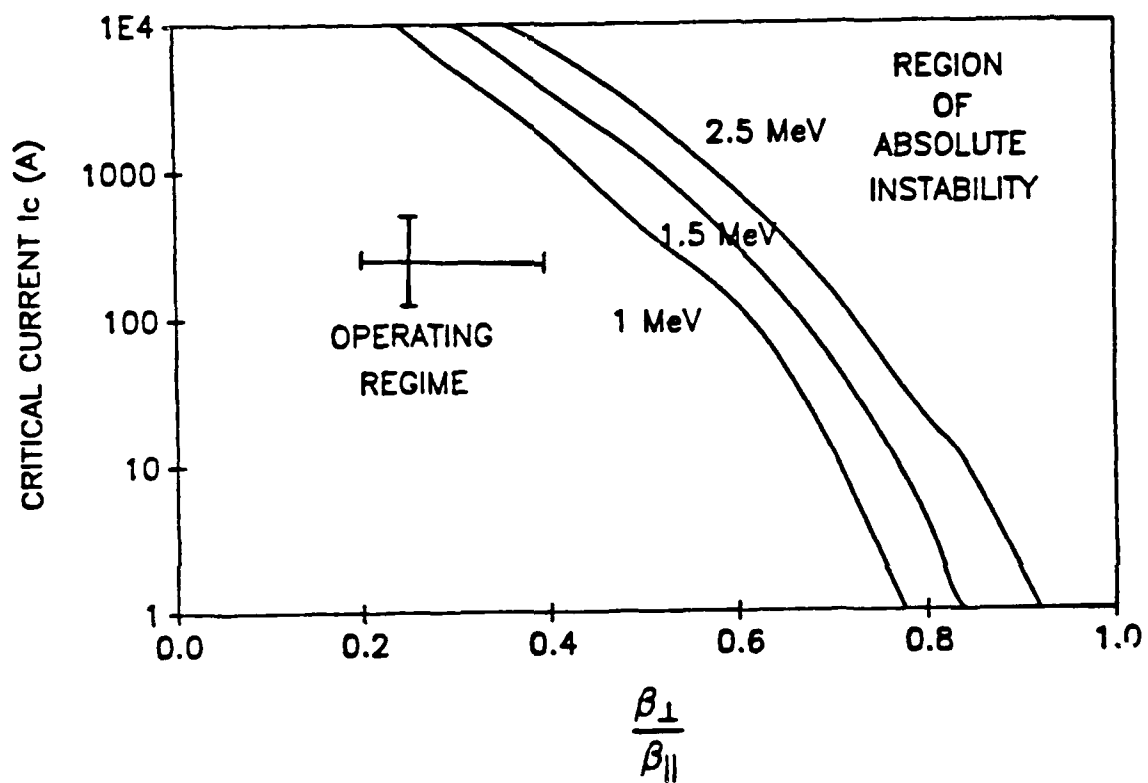


Figure 4-2: Pinch Point Analysis

can be altered, such as  $\alpha$ , current, detuning,  $B_z$ , and  $B_w$ . The process of predicting the maximum output of the device is accomplished through the use of numerical simulations. The simulated maximum output parameters are then experimentally tested and modifications made to either the simulation or experiment as appropriate. The analytic basis for the numerical method is presented below followed by a detailed description of each parameter available for manipulation.

The equations of motion of the electrons in the beam and the wave equation that includes the boundary conditions of the device form a closed set of ordinary differential equations that self-consistently describe the CARM interaction. These equations are as follows for a  $TE_{11}$  mode:

$$\frac{d\gamma}{d\hat{z}} = -J_0(k_{\perp}r_g)J'_1(k_{\perp}r_L)\frac{\hat{p}_{\perp}}{p_{\parallel}}\text{Re}(F_0e^{i\Lambda}) \quad (4.13)$$

$$\frac{d\hat{p}_{\parallel}}{d\hat{z}} = \frac{1}{\beta_{ph}}\frac{d\gamma}{d\hat{z}} - J_0(k_{\perp}r_g)J'_1(k_{\perp}r_L)\frac{\hat{p}_{\perp}}{\hat{p}_{\parallel}}\text{Im}\left(\frac{dF_0}{d\hat{z}}e^{i\Lambda}\right) - \frac{\hat{p}_{\perp}^2}{2\hat{p}_{\parallel}B_z}\frac{dB_z}{d\hat{z}} \quad (4.14)$$

$$\frac{d\Lambda}{d\hat{z}} = \frac{1}{\hat{p}_{\parallel}}\left(\gamma - \frac{\hat{p}_{\parallel}}{\beta_{ph}} - \hat{\Omega}_{c0}\right) - \frac{1}{\hat{p}_{\perp}\hat{p}_{\parallel}}J_0(k_{\perp}r_g)\frac{J_1(k_{\perp}r_L)}{k_{\perp}r_L}\left[\left(\gamma - \frac{\hat{p}_{\parallel}}{\beta_{ph}}\right)\text{Im}(\hat{F}_0e^{-i\Lambda}) + \hat{p}_{\parallel}\text{Re}\left(\frac{d\hat{F}_0}{d\hat{z}}e^{i\Lambda}\right)\right] \quad (4.15)$$

$$\frac{d\hat{F}_0}{d\hat{z}} = 4\pi\beta_{ph}\left(\frac{I_b}{I_A}\right)\left(\frac{C_{11}}{k_{\perp}}\right)^2\left(\frac{ck_{\perp}}{\omega}\right)^2\langle J_0(k_{\perp}r_g)J'_1(k_{\perp}r_L)\frac{\hat{p}_{\perp}}{\hat{p}_{\parallel}}e^{i\Lambda} \rangle \quad (4.16)$$

where  $I_b$  is the electron beam current in amperes,  $I_A = mc^3/e \simeq 17$  kA is the Alfvén current,  $\beta_{ph} = \omega/ck_{\parallel}$ ,  $\hat{\Omega}_{c0} = \Omega_{c0}/\omega$ ,  $\hat{z} = \omega z/c$ ,  $\vec{\hat{p}} = \gamma\vec{v}/c$ ,  $\gamma = (1 + \hat{p}_{\perp}^2 + \hat{p}_{\parallel}^2)^{1/2}$ ,  $\Lambda \equiv \phi - \omega t + k_{\parallel}z$ , (see figure 4-1) and

$$C_{11}^2 = k_{\perp}^2/(\pi(\nu_{11}^2 - 1)J_1^2(\nu_{11})) \quad (4.17)$$

where  $J'_1(\nu_{11}) = J'_1(k_{\perp}r_w) = 0$  where  $r_w$  is the waveguide radius in cm.

The normalized distribution function is related to the field strength through

$$\hat{F}_0 = \left(\frac{C_{11}}{k_{\perp}}\right)\left(\frac{ck_{\perp}}{\omega}\right)^2 E_{11} \frac{\omega}{I_A} e^{-i\pi/2} \quad (4.18)$$

where  $E_{11}$  is defined by

$$\vec{E}_{11}(\vec{r}, t) = E_{11} e^{ik_{\parallel} z} \hat{z} \times \vec{\nabla}_{\perp} [C_{11} J_1(k_{\perp} r) e^{im\theta}] e^{-i\omega t}. \quad (4.19)$$

The field strength is related to the power through

$$P_{11} = \frac{1}{8\pi} \frac{k_{\parallel} c^2}{\omega} k_{\perp}^2 |E_{11}|^2 \quad (4.20)$$

where  $P_{11}$  is the power associated with the  $TE_{11}$  mode. Finally, the beam and wave energies are conserved through the energy balance

$$\left( \frac{I_{beam}}{e} \right) \cdot \langle m_0 c^2 (\gamma - 1) \rangle + P_{11} = \text{constant}. \quad (4.21)$$

These equations form the basis of the numerical simulations. The averaged quantities in equations 4.16 and 4.21 are the averages over all of the macroparticles of the simulation. These equations represent  $3N_p + 2$  simultaneous differential equations ( $N_p$  is the number of macroparticles) that are solved at each  $z$  step of the simulation. Note that they retain the dependence on the finite Larmor radius and offset guiding center as was shown necessary in the previous section. What is not included in these equations are the possibilities of guiding center drifts, current loss, or any multimode interaction. A further averaging is applied to equation 4.16

$$\langle J_0(k_{\perp} r_g) J_1'(k_{\perp} r_L) \frac{\hat{p}_{\perp}}{\hat{p}_{\parallel}} e^{i\Delta} \rangle \rightarrow J_0(k_{\perp} \langle r_g \rangle) J_1'(k_{\perp} \langle r_L \rangle) \langle \frac{\hat{p}_{\perp}}{\hat{p}_{\parallel}} e^{i\Delta} \rangle. \quad (4.22)$$

The numerical simulations utilized are multiparticle codes that involve up to 1024 macroparticles which are integrated through sufficiently small steps in the interaction space. C. Chen [30] is the developer of the code used in this experiment which is an improvement over earlier CARM codes [29] that did not consider the effect of finite Larmor radius and offset guiding center. The code models the CARM amplifier for a single  $TE_{mn}$  or  $TM_{mn}$  waveguide mode and includes the following effects: 1) harmonic interactions, 2) any  $TE$  waveguide mode one at a time, 3) annular or solid electron beams, 4) waveguide losses, 5) energy, momentum and guiding center spreads usually loaded as Gaussians and 6) the finite Larmor radius and offset guiding center.

What is currently lacking from the process is the ability to take the data from the simulation of the beam dynamics as direct input into the CARM amplifier code. Having the disconnect between the results of chapters 3 and 4 does, however, allow an experimenter to gauge the capabilities of each section of the device before operating it as a complete system.

### 4.3.1 Simulation Results

The Chen code is used in this chapter to study the effect of varying different parameters on the characteristics of the CARM interaction. This analysis can help to answer questions such as the effect of beam temperature, perpendicular velocity, and beam current on the growth rate and efficiency of the CARM device. The first computational result is the effect of beam temperature on the efficiency and growth rate of the CARM interaction. As shown in chapter 2, the initial temperature of the beam is a function of diode geometry, current, energy, and axial magnetic field. These physical properties are fixed over the range of parameters used in this experiment and a value of  $\Delta\gamma_{\parallel}/\gamma_{\parallel} = 4.4\%$  was used consistently through all simulations as the value at the beginning of the wiggler region. It was shown in chapter 3 that the interaction of the beam with the wiggler field will cause some growth in energy spread. The beam loading into the CARM simulation was done in a manner that matched the output of the beam dynamics simulations to some extent. Table 4.1 shows the parameters used in the analysis presented in this chapter. In what follows, the efficiency and linear growth rate are calculated as a function of each of the parameters of table 4.1.

Figure 4-3 shows the effect of energy spread on the growth rate and efficiency of the CARM interaction. As can be seen, energy spreads above 10% greatly inhibit the CARM interaction.

The next study is the effect of  $\alpha$  on the characteristics of the CARM interaction. Since the purpose of the wiggler is to impart sufficient perpendicular velocity to the beam, it is important to know how much of an increase in output power is gained as a function of  $\alpha \equiv \beta_{\perp}/\beta_{\parallel}$ , since the process of spinning up the beam



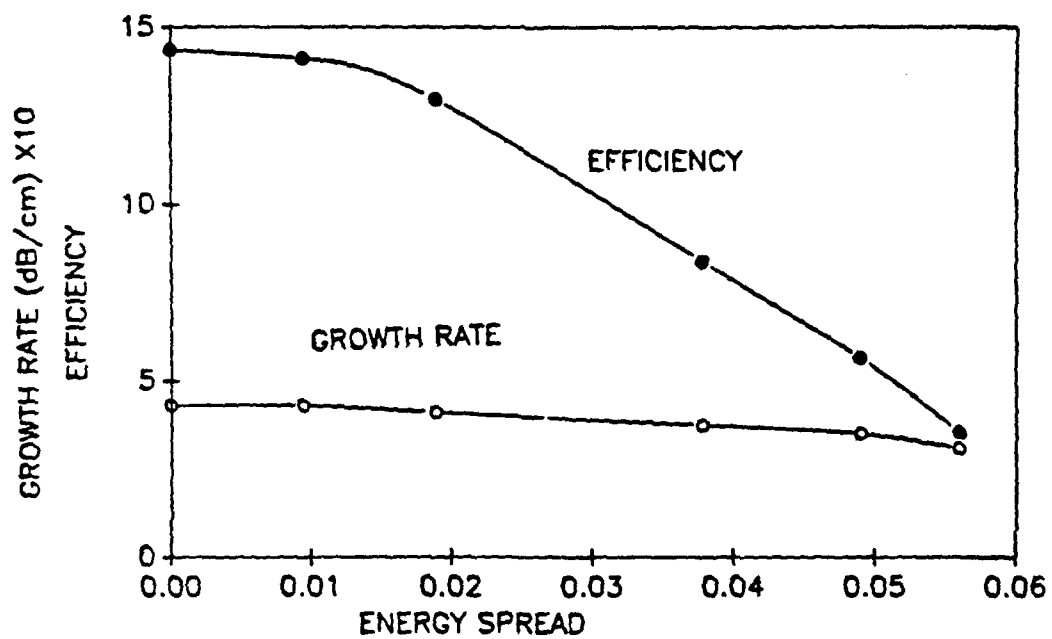


Figure 4-3: Effect of energy spread on the growth rate and efficiency of the CARM interaction. Parameters used are those shown in table 4.1.

Table 4.1: Simulation Parameters

Parameter	When Fixed	Range of Variation
$\Delta\gamma_{\parallel}/\gamma_{\parallel}$	0.00	0.00 to 0.06
$\alpha$	0.27	0.2 to 0.5
$\Delta$ as percent deviation from 35 GHz	0.0	-50% to +50%
Current $I$	128 A	100 to 600 A
$\gamma$	4.0	constant
$B_z$	5.4 kG	constant
$\langle r_g \rangle$	0.16cm	constant

without significantly increasing beam temperature is not trivial. Figure 4-4 shows the effect of  $\alpha$  on the growth rate and efficiency of the CARM interaction. In this simulation only the value of  $\alpha$  is changed. It must be remembered that the trajectory simulations of chapter 3 have shown that changes in the fields that generate a particular  $\alpha$  also can effect the energy spread. These added factors have not been included in these single parameter analyses. The values of  $\alpha$  shown in figure 4-4 are those that can be expected in this experiment.

The next study is the effect of varying the detuning parameter ( $\Delta$ ) on the growth rate and efficiency of the CARM device. The detuning is directly proportional to the value of the axial magnetic field. Caution is needed, however, since the axial field also has a direct effect on the amount of  $\alpha$  that is generated in the wiggler region. As the axial and wiggler fields are experimentally tuned, the actual power emitted by the CARM device becomes not only a function of the detuning, but also a function of  $\alpha$  and beam temperature as well. Figure 4-5 shows the effect of changing only the detuning on the efficiency and growth rate of the CARM. The detuning parameter can also be used to generate an expected gain bandwidth curve. This is done by changing the input frequency in the simulation and keeping the axial field constant. This gain bandwidth is shown in figure 4-6.

Lastly, a study of the effect of beam current on the growth rate and efficiency

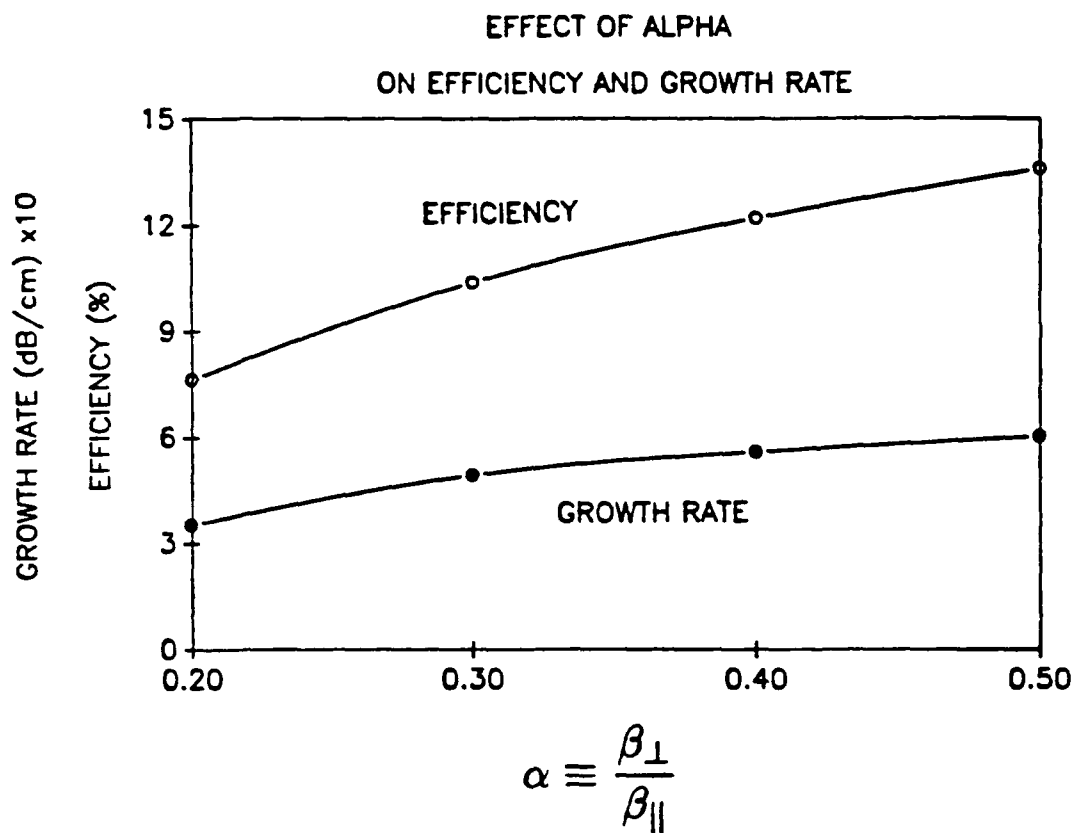
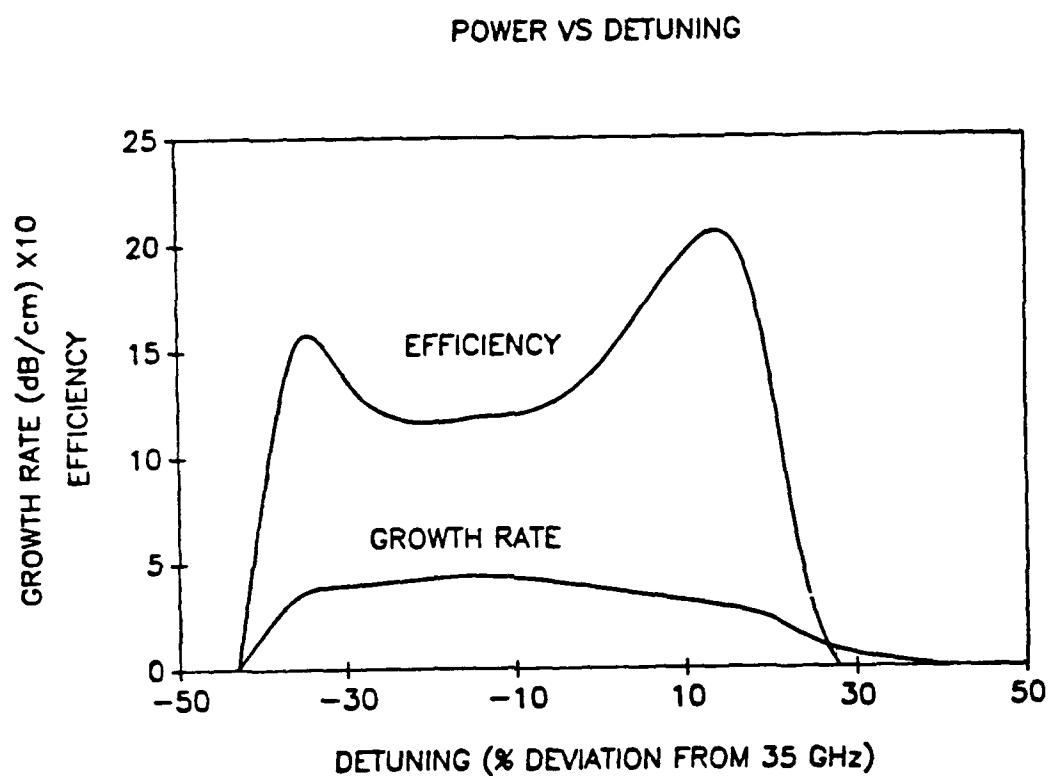
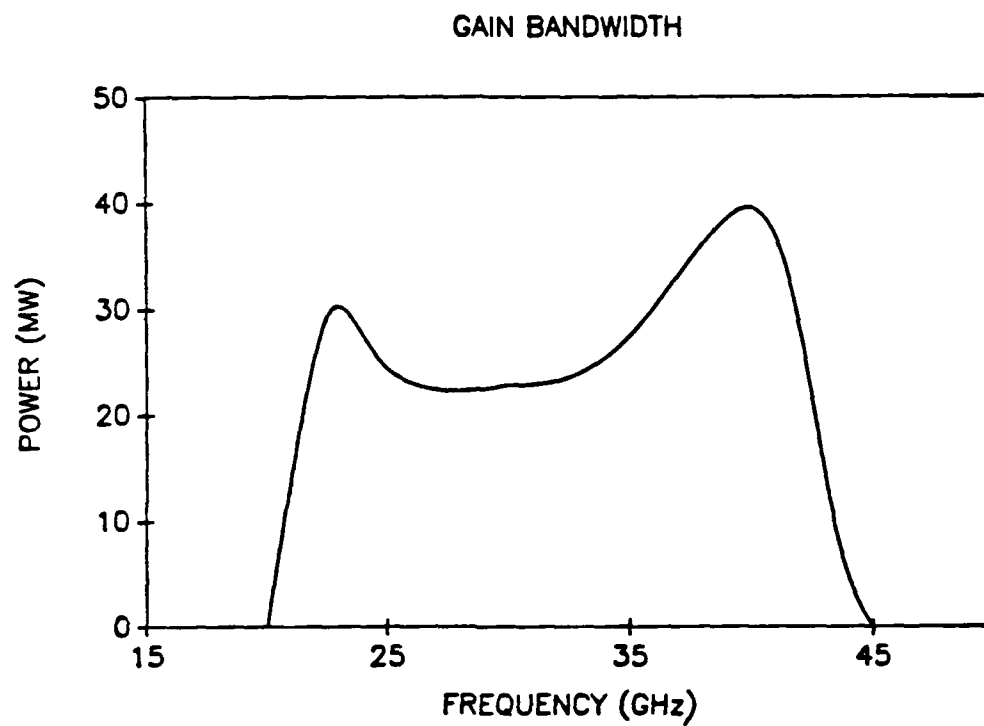


Figure 4-4: Effect of  $\alpha$  on the growth rate and efficiency of the CARM. Parameters are those of table 4.1 except for  $B_z$ , which is the resonant value appropriate to each  $\alpha$  in the figure.



**Figure 4-5: Effect of changing  $\Delta$  on the efficiency and growth rate of the CARM. Parameters used are those of table 4.1.**



**Figure 4-6: Gain bandwidth. Parameters used are those of table 4.1.**

of the CARM is presented. The current is a quantity fixed by the diode aperture, the axial field and the beam energy. Figure 4-7 shows that the efficiency increases dramatically for increased current. This suggests that continued work should be done on high current sources for microwave devices. The present experiment operates in a regime where dc space charge has a negligible effect on the beam dynamics (see chapter 3) and where the onset of an absolute instability is avoided due to large beam-wave coupling constant (which is proportional to  $\omega_p$ ). As beam current density is increased, these effects could become increasingly important.

Having searched the range of parameters of the experiment to establish boundaries in the growth and efficiency available to the CARM, the next step is to produce a simulation of the power as a function of  $z$  in the interaction region. Figure 4-8 shows the growth of the output power as a function of the interaction length. The parameters for this simulation are those of table 4.1. The effect of finite Larmor radius is shown in this figure. Note that taking account of finite Larmor radius into the simulation results in a decrease in expected power from 87 to 21 MW.

After a certain interaction length, the power shown in figure 4-8 ceases to grow as the interaction becomes saturated. The value of the power output then oscillates as a function of  $z$ . As mentioned previously, this is due to the trapping of the beam particles in a ponderomotive wave. This trapping can be seen in figure 4-9, which shows the value of each particles energy ( $\gamma$ ) and phase ( $\psi$ ) in relation to the wave. Four different pictures are presented which correspond to points along  $z$ . (These points are shown as 1-4 in figure 4-10). The parameters of figures 4-9 and 4-10 are those of table 4.1. The distribution of particles is initially uniform, becomes increasingly bunched in the linear growth region, and finally begins to alternate between trapped (power-absorbing) and untrapped (power-releasing) after power saturation in a region where the power oscillates.

As stated in the previous section, the efficiency of the CARM interaction can be increased if the axial magnetic field is tapered beginning at a  $z$  position just prior to the beginning of power saturation. The effect of tapering the axial field is most prominent for a cold beam. The efficiency enhancement of tapering a cold beam, using the parameters of the group I experiment are shown in figure 4-10(a). As can

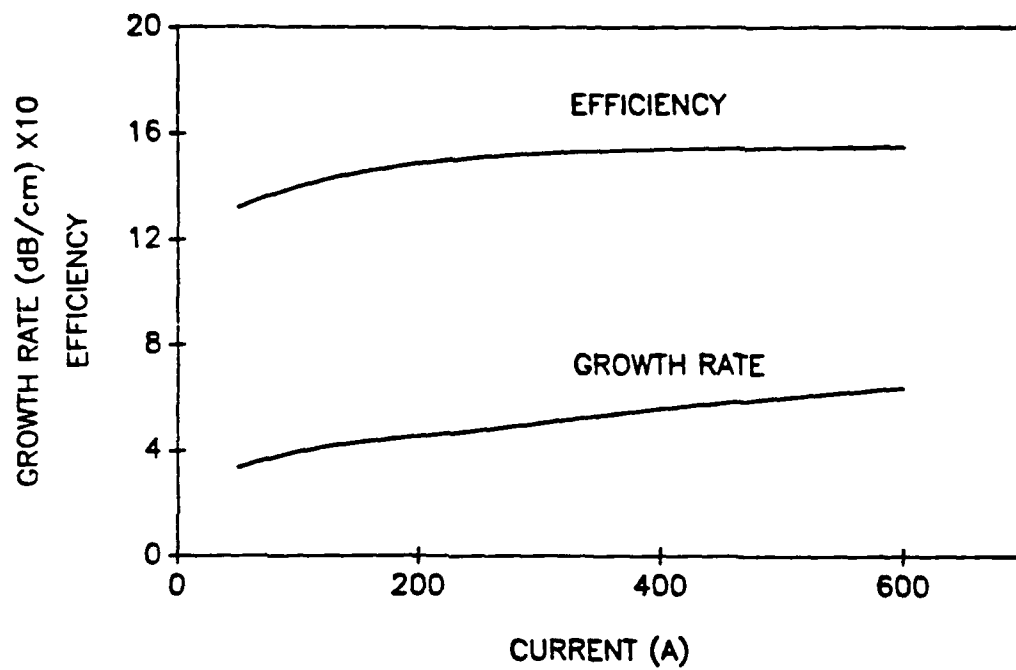


Figure 4-7: Effect of beam current on the efficiency and growth rate of the CARM. Parameters used are those of table 4.1.

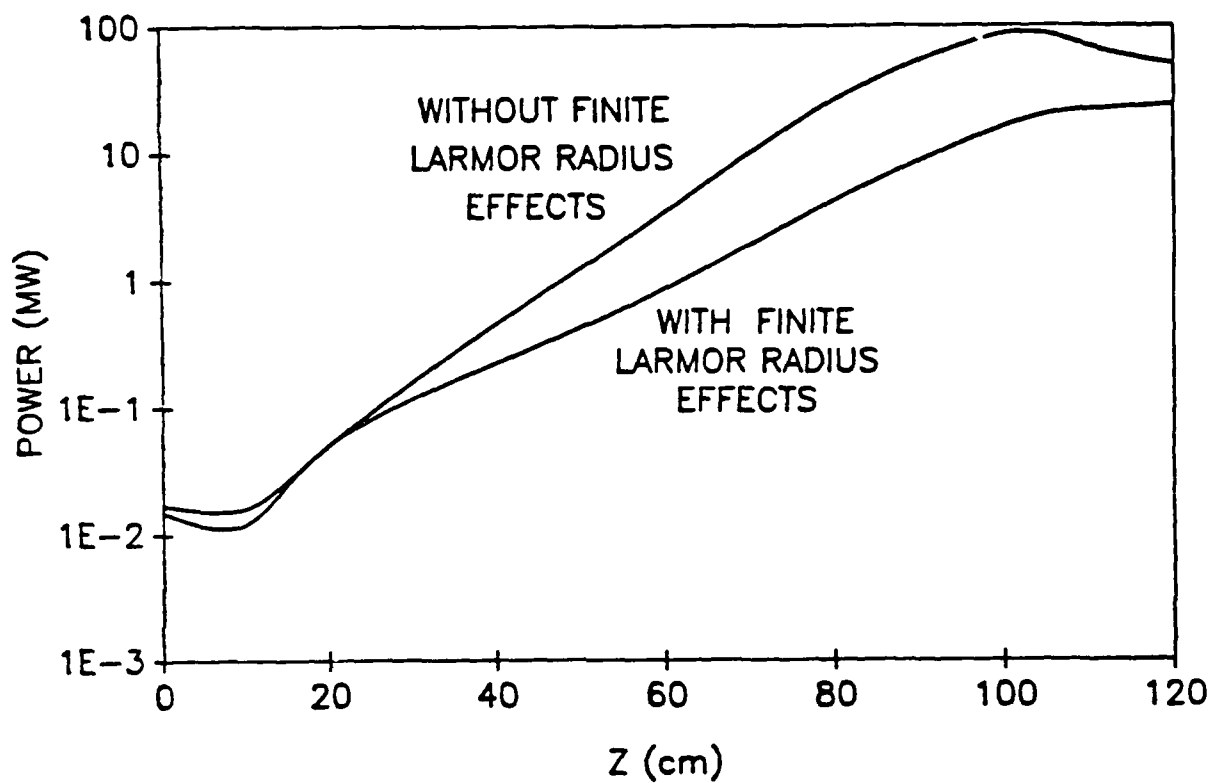


Figure 4-8: Power as a function of interaction length  $z$ . Parameters used are those of table 4.1.



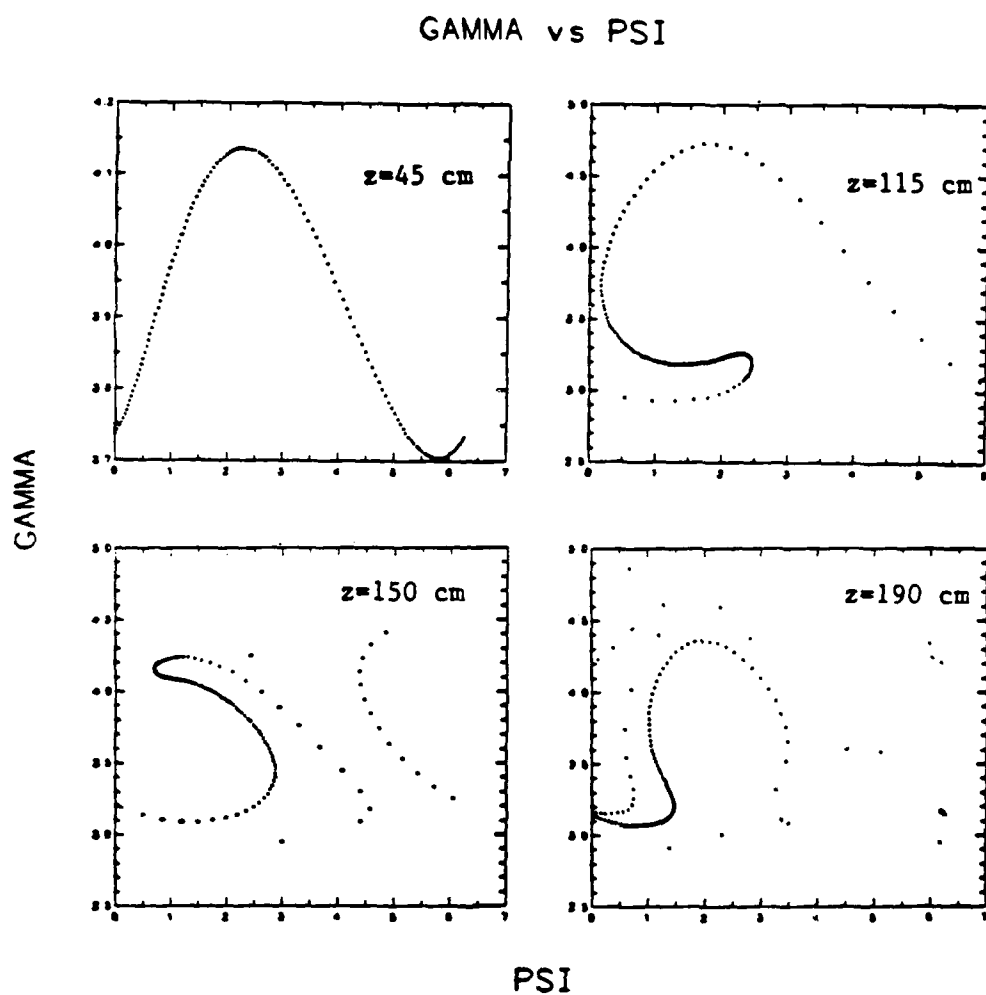


Figure 4-9:  $\gamma$  vs  $\psi$  for various locations in the interaction region. Parameters used are those of table 4.1.

be seen, the output power, at  $z=200$  cm increases from 23 to 95 MW. Tapering the axial field is considerably less effective when a beam with the energy spread present in the experiment is used. Figure 4-10(b) shows the effect of tapering when a warm beam is used ( $\Delta\gamma_{\parallel}/\gamma_{\parallel}=5.6\%$ ). The effect is negligible.

## 4.4 Conclusions

Numerical simulations can only be used as a guide. Physical processes are difficult to model and experimental expectations should not be based simply on simulation results. As mentioned before, there is a disconnect between the output of the beam dynamics model and the CARM interaction model. While the former is used to get an accurate picture of the beam as it enters the CARM region, the latter takes a relatively simple set of particle loading parameters as input. What is currently missing, besides the ability to use the output of one model as input to the other, is the realistic spatial coupling of the beam and wave. As was seen in chapter 3, each electron of the beam can have a different offset guiding center ( $r_g$ ) and Larmor radius ( $r_L$ ). The simulations presented in this chapter use average values for  $r_g$  and  $r_L$ . This results in a beam cross section that is only an approximation of the spatial distribution of the beam as calculated by the trajectory code (chapter 3). The beam cross sectional spatial distribution determines the effective filling factor of the beam in the waveguide which, in turn, determines the ability of the wave to extract power from the beam. The approximation of the filling factor different from that actually present would cause the simulation to incorrectly predict the output of the actual device. These simulations also show that the beam quality is an important factor in the construction of a CARM device. They also show the tradeoffs possible between  $\alpha$ , current, and device configuration that can maximize the output of the device. The models presented do, nevertheless, give a good estimate of an upper bound on the efficiency and growth rate of the CARM. In this manner overly optimistic expectations can be avoided.

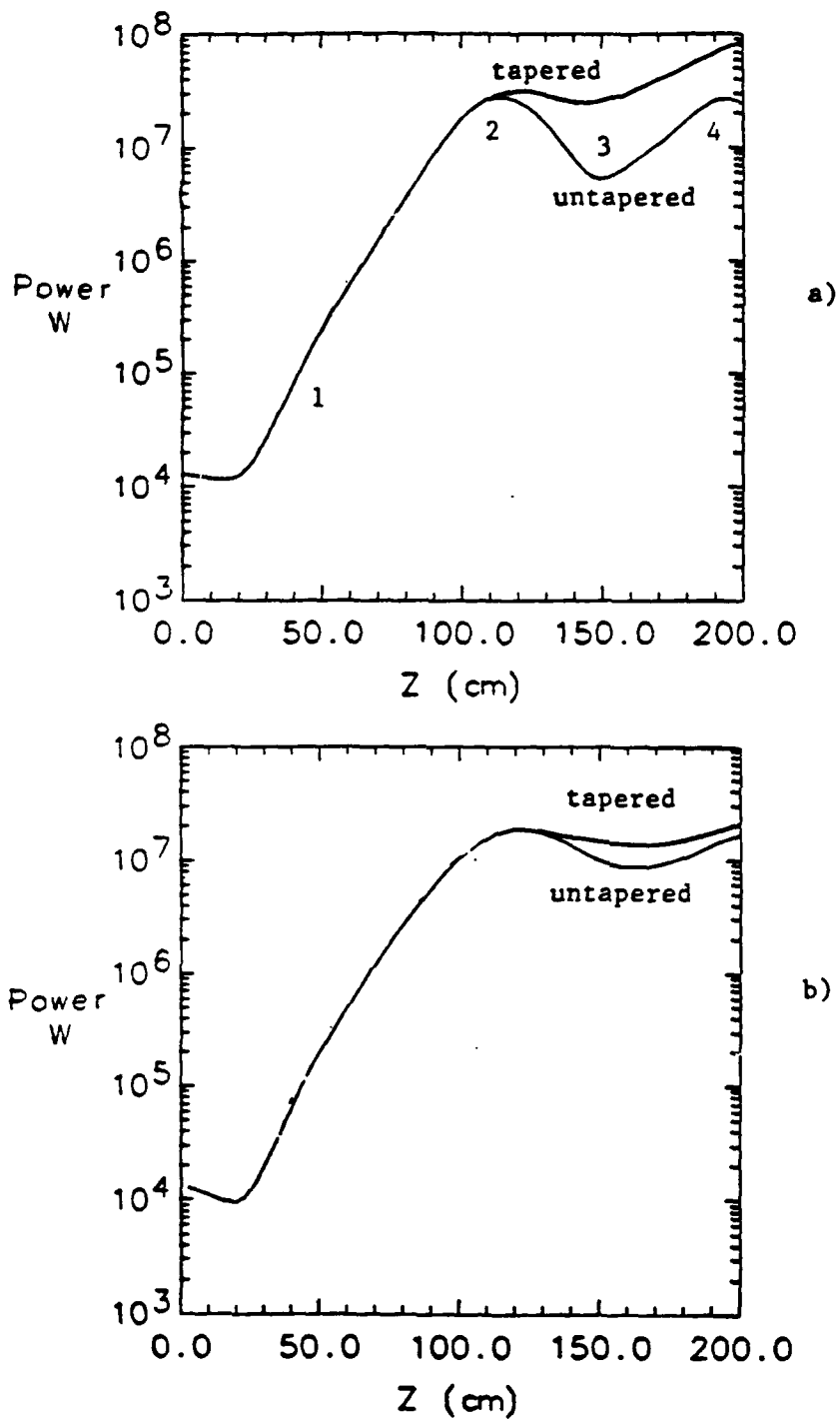


Figure 4-10: The effect on the output power of the CARM interaction after power saturation due to magnetic field tapering. (a) Cold beam (b) Warm beam. Parameters used are those of table 4.1.

# Chapter 5

## Experimental Results

### 5.1 Introduction

This chapter will describe the measurements of the various parameters of the CARM interaction. Successful operation of the CARM has been achieved using both the group I and II orbits to impart perpendicular velocity to the beam. A comparison is made between numerical simulations and experimental results for both the group I and II CARM. The average Larmor radius  $\langle r_L \rangle$  and the average offset guiding center  $\langle r_g \rangle$  are determined from trajectory simulations presented in chapter 3. These  $\langle r_L \rangle$  and  $\langle r_g \rangle$  values, and the beam energy spread  $\Delta\gamma_{\parallel}/\gamma_{\parallel} = 4.4\%$  calculated for the electron beam at the exit of the diode, are used in the simulations of the CARM interaction. This has resulted in an improved method of predicting the outcome of the actual CARM experiment.

As in most experiments, theoretical predictions were used to give a general set of parameters for the experiment such as voltage, current, and axial and wiggler magnetic fields. The individual parameters were then scanned to optimize the resulting power of the CARM device. Since the perpendicular velocity in the beam is a function of the axial field strength in the wiggler region, changes in the axial field strength in the CARM region effect the  $\alpha$  generated in the wiggler. Similarly, the total current generated by the diode is also a function of the axial magnetic field

Table 5.1: Experimental Parameters and Results

Parameter	Group I CARM	Group II CARM
	Measured	
$\gamma$	3.94	3.94
$I$	128 A	128 A
$B_z$	5.4 kG	6.1 kG
$B_w$	840 gauss	490 gauss
$\alpha$	$0.3 \pm .1$	$0.35 \pm .08$
$P_{in}$	17 kW	18 kW
$P_{out}$	12.2 MW	8.7 MW
Efficiency $\eta$	6.3%	4.5%
$\Gamma$ amplifier	50 dB/m	62 dB/m
$\Gamma$ superradiant	42 dB/m	45 dB/m
	Calculated	
$\alpha$	0.27	0.30
$\Delta\gamma_{  }/\gamma_{  }$	5.6%	4.5%
$\langle r_L \rangle$	0.35 cm	0.42 cm
$\langle r_g \rangle$	0.15 cm	0.16 cm

(see chapter 2). Changes in current and  $\alpha$  effect the CARM interaction as well as do changes in the axial magnetic field. Hence, scanning one parameter invariably effects the others which in turn complicate the comparison of the output of the CARM device to theoretical predictions. Table 5.1 is a list of the experimental parameters and results of the CARM experiments presented in this chapter.

## 5.2 The CARM Interaction Utilizing the Group I Orbits

In this section, results of several of the experimental parameter sweeps will be presented. The data that will be presented in the parameter sweeps is for the CARM operating in the amplifier mode with an input signal of 15-24 kW (the value at the beginning of the CARM region) from the fixed frequency magnetron driver. The amplified power as a function of interaction length  $z$  is then presented and compared with numerical simulations. The CARM also is operated in the superradiant mode (defined as amplification of background noise). Power as a function of interaction length  $z$  is presented. Angular radiation patterns are shown for both the amplifier and superradiant case.

The results of the scanning of axial and wiggler fields are presented in figures 5-1 and 5-2. These two figures represent those field settings ( $B_z$  and  $B_w$ ) that generate the most radiation. The first figure (5-1) is a scan of the axial magnetic field while holding the value of the wiggler field fixed at 840 gauss. The next figure (5-2) shows the results of sweeping the wiggler field while keeping the axial field constant. The sweep was done at the maximum value shown on the previous figure ( $B_z = 5.4$  kG). These scans determined the final experimental settings of  $B_z=5.4$  kG and  $B_w=840$  gauss which were used for the experimental determination of power versus interaction length of the CARM device.

An analysis of the beam dynamics at the maximum power ( $B_z=5.4$  kG) and minimum power ( $B_z=6.2$  kG) of figure 5-1 has been shown in figures 3-6 and 3-7. As a result of the increase in energy spread and spatial dispersion of the beam as shown in figures 3-6 and 3-7, one would expect a decrease in the output power of the device. This is demonstrated by the numerical simulations which show a calculated decrease in power of 5.6 dB which compares favorably to the experimental value of 8.9 dB shown in figure 5-1. The discrepancy is due to the fact that the model only takes an average Larmor radius and guiding center radius as input. The more dispersion in the beam, especially at the  $B_z=6.2$  kG point, the less accurate is the

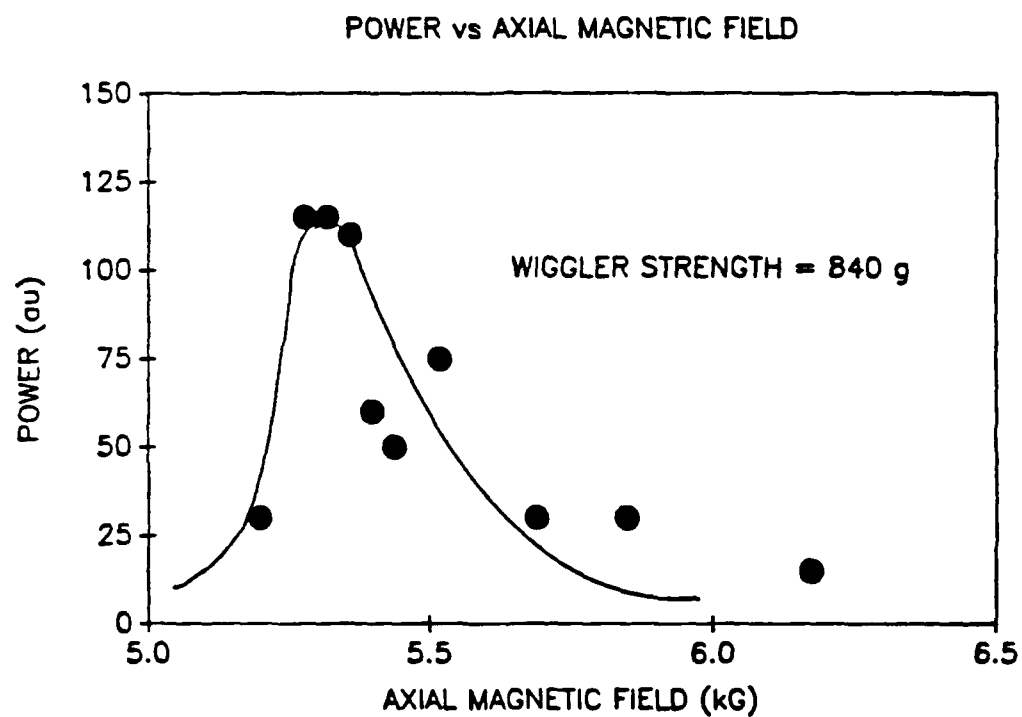


Figure 5-1: CARM power as a function of axial magnetic field.  $B_w=840$  gauss,  $I=128$  A,  $\gamma=3.94$ .

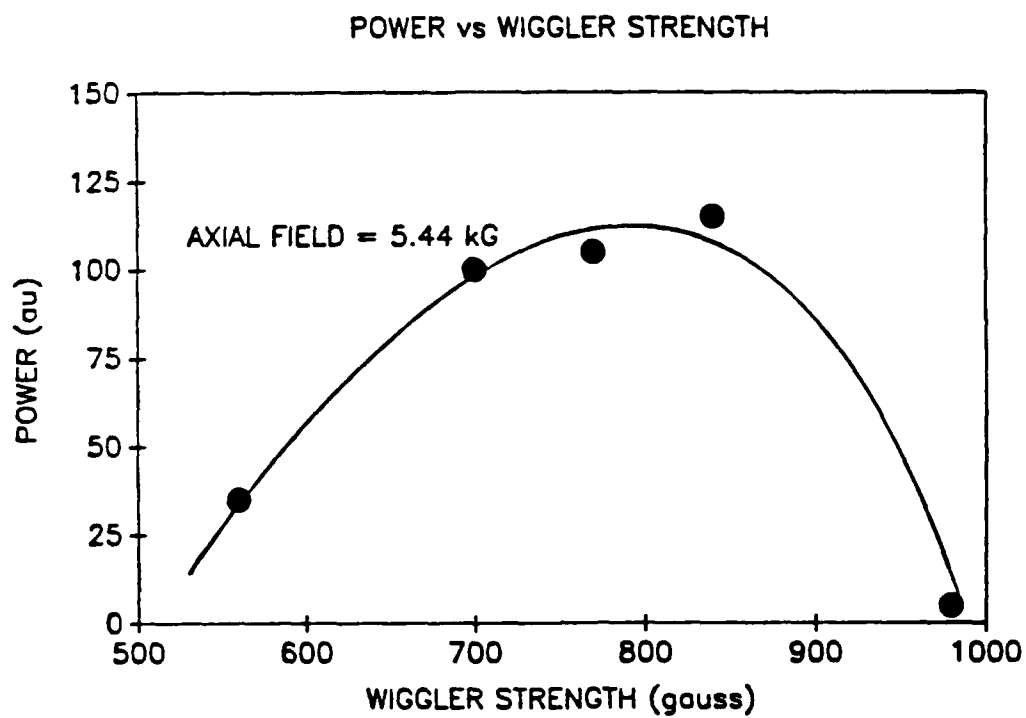


Figure 5-2: CARM power as a function of wiggler strength.  $B_z=5.4$  kG,  $I=128$  A,  $\gamma=3.94$ .

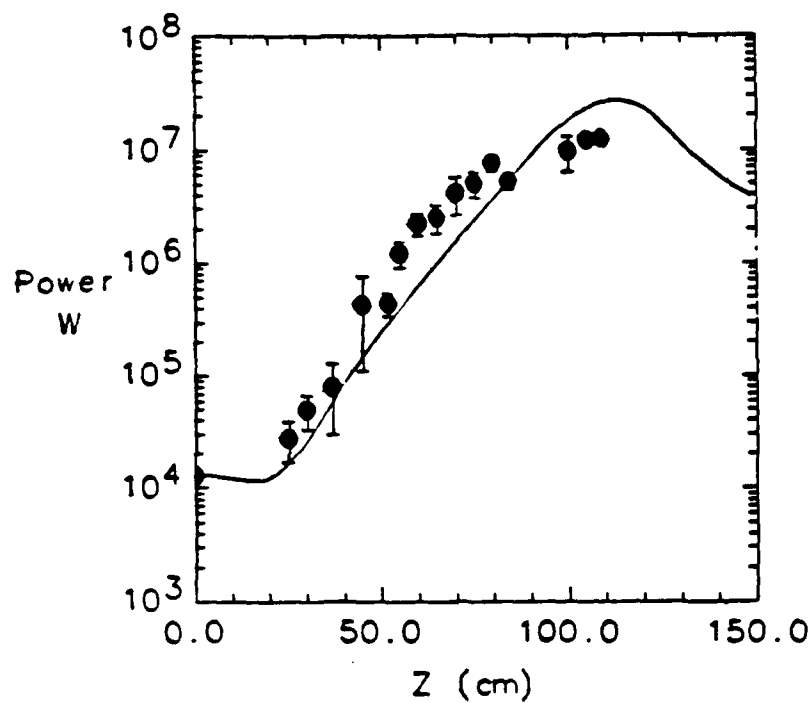


simulation.

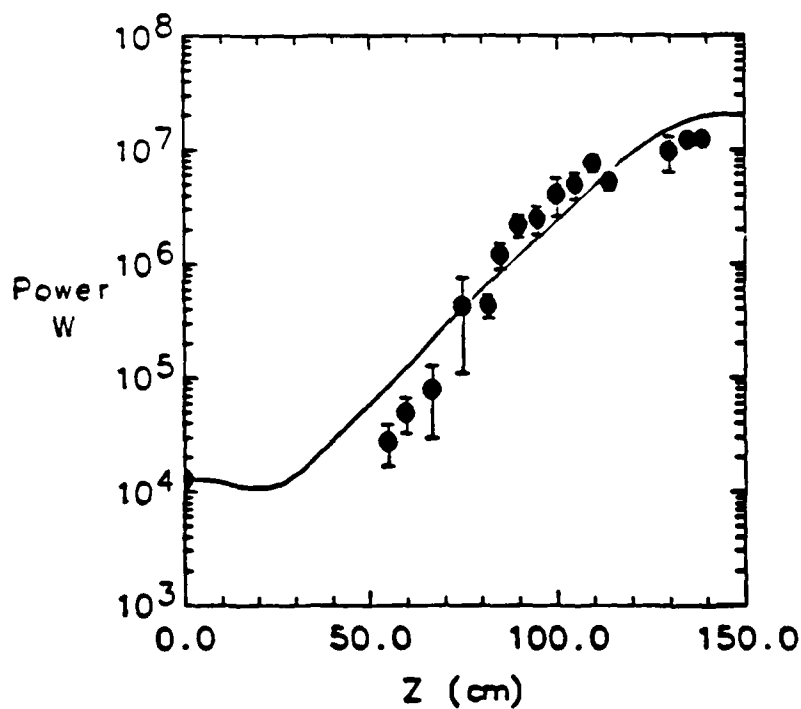
The power versus interaction length is determined in the following manner. The CARM device is operated with a kicker magnet placed at various  $z$  positions. The transversely placed 1-2 kilogauss electromagnet kicks the beam into the waveguide walls at selected positions thereby terminating the interaction at that  $z$  position. For the case of group I orbits in the wiggler, the CARM power versus interaction length is shown in figure 5-3. Two figures are presented. In figure 5-3(a) a comparison is made between the experimental data and the simulation for a cold beam. Notice that the growth rate is initially the same but that the experimental values show a power saturation an order of magnitude lower than that of the simulation. Figure 5-3(b) shows a comparison between the experimental points and the results of numerical simulations with an energy spread determined by the beam trajectory code. The parameters of the simulation are  $\gamma=3.94$ ,  $i=128$  A,  $\alpha=.27$ ,  $\Delta\gamma_{\parallel}/\gamma_{\parallel}=4.4\%$ ,  $\langle r_L \rangle=0.42$  cm, and  $\langle r_g \rangle=0.16$  cm. The CARM code shows much better agreement with experiment when the realistic beam parameters are used than for a cold beam. Note that the experimental power values rise linearly (on the log ordinate) to some point of saturation and then begin an oscillatory motion, consistent with numerical simulation (see section 4.5). After saturation has occurred, the power varies between 5.2 MW and 12.2 MW. The linear growth rate is 50 dB/m.

The CARM was also operated in the superradiant mode in which the power was allowed to grow out of background noise. All of the power measurements were taken through a narrow pass filter ( $34.8 \pm 1.2$  GHz) for the Ka band waveguide. The superradiant power growth for the group I CARM is shown in figure 5-4. The growth rate is 42 dB/m which is somewhat lower than for the case of amplification of an input signal. The fact that the growth rate for the superradiant case is somewhat lower than for the amplifier mode is not fully understood, however, may be attributed to multimoding (same frequency, different wavenumber) in the superradiant case, whereas modes other than the  $TE_{11}$  input mode are suppressed in the high power amplifier case.

Table 5.2 lists the modes and cutoff frequencies,  $\omega_c$ , below 35 GHz that can exist in the waveguide. A qualitative analysis of the electron beam/mode coupling [30]



a)



b)

Figure 5-3: Power as a function of interaction length for the group I wiggler CARM. Comparison of experimental points with simulation of (a) cold beam interaction and (b) warm beam interaction with  $\Delta\gamma_{\parallel}/\gamma_{\parallel}=4.4\%$ . Experimental parameters are shown in table 5.1.

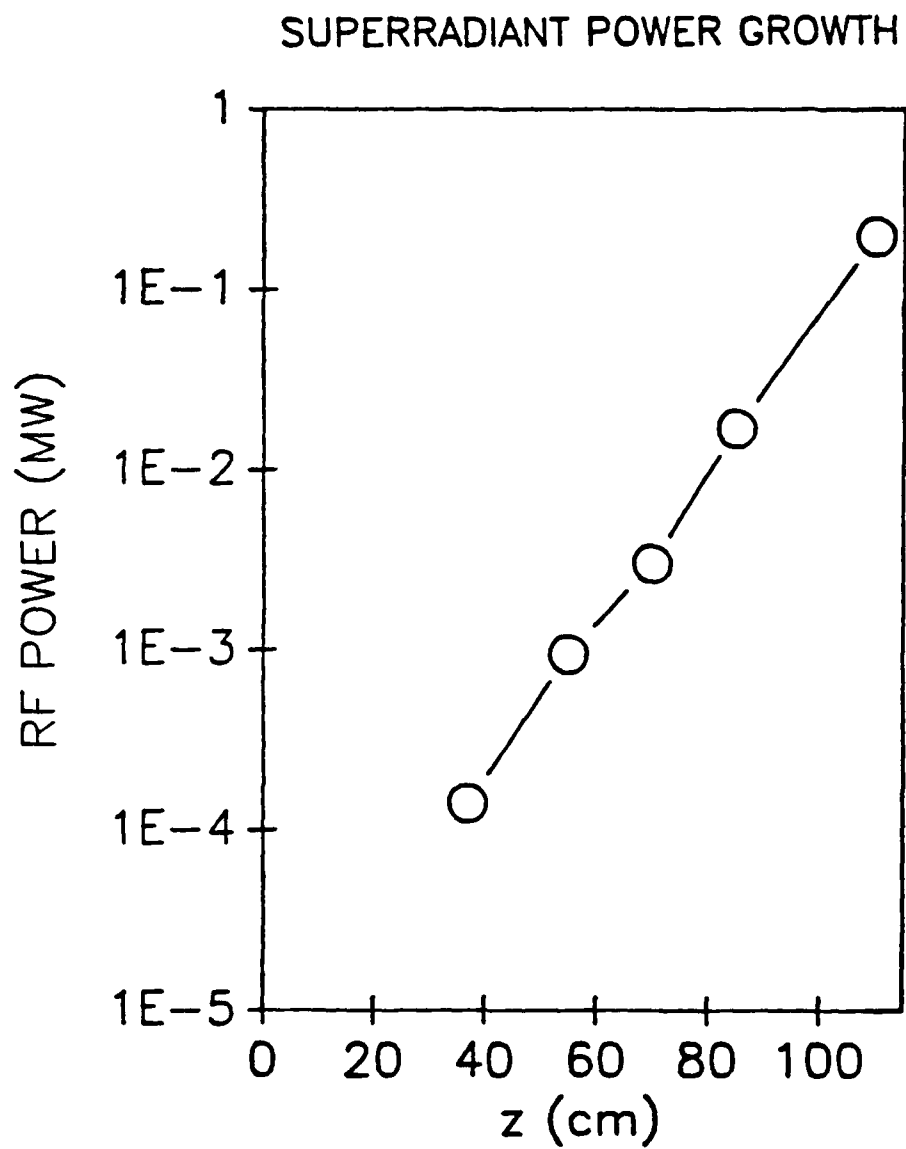


Figure 5-4: Superradiant power as a function of interaction length for the CARM generated by group I orbits in the wiggler. Experimental parameters are shown in table 5.1.

Table 5.2: Waveguide Modes and Cutoff Frequencies

Waveguide Mode	Cutoff Frequency (GHz)
$TE_{11}$	11.07
$TM_{01}$	15.05
$TM_{11}$	22.80
$TE_{01}$	22.80
$TM_{02}$	33.10

Table 5.3: Coupling Between Available Waveguide Modes

MODE	$TE_{11}$	$TM_{01}$	$TM_{11}$	$TE_{01}$	$TM_{02}$
$TE_{11}$	1	0	strong	0	0
$TM_{01}$		1	0	weak	weak
$TM_{11}$			1	0	0
$TE_{01}$				1	weak
$TM_{02}$					1

proceeds as follows. First, the beam location in the waveguide must be determined (as in chapter 3). Second, the modes present in the waveguide that have the correct frequency must be determined (table 5.2). Third, the beam spatial profile and waveguide mode intensity patterns must be compared. Fourth, the coupling between the modes themselves is determined from the selection rules for the modes. (For instance  $TE_{mn}$  modes only couple if  $m$  is the same for both modes.) Assuming azimuthal symmetry of the beam profile ( $\langle r_g \rangle$  small), qualitative judgements of the strength of mode-to-mode coupling for this experiment have been made. Given azimuthal symmetry,  $TE_{mn}$  and  $TM_{mn}$  mode coupling can only occur between modes that possess the same azimuthal number  $m$ . Therefore, the  $TE_{11}$  mode does not couple to the  $TE_{01}$  mode, however it could couple to the  $TM_{11}$  mode. Table 5.3 shows qualitatively the possible coupling between the modes available.

Figure 5-5 presents the uncoupled beam and waveguide modes. Inspection of this figure shows that while the closest mode to the  $TE_{11}$  mode is the  $TM_{01}$  mode, mode coupling analysis suggests that the next nearest mode,  $TM_{11}$  is the most likely candidate for coupling.

Experimental determination of a particular mode type can be made by analyzing the far field angular radiation pattern. The angular scan is presented for both the amplifier and superradiant case of the CARM utilizing group I wiggler orbits. The experiment is designed so that only a  $TE_{11}$  mode is launched into the circular waveguide. In chapter 2 it was confirmed that the radiation pattern resulting from the magnetron signal propagating through the system in the absence of the electron beam was indeed that of the  $TE_{11}$  mode. Figure 5-6 shows the pattern of the magnetron alone (open circles) and the pattern generated by the CARM operating in the amplifier mode (solid circles). The solid line in figure 5-6 represents the calculated horn profile for the  $TE_{11}$  mode as discussed in chapter 2. This confirms the fact that the radiation emitted by the CARM amplifier is only in the  $TE_{11}$  mode.

Figure 5-7(a) shows the radiation pattern of the superradiant radiation (no magnetron). Figure 5-7(b) shows the calculated angular patterns for the  $TE_{11}$  and  $TM_{11}$  modes (see section 2.2.4). Of all the mode patterns available as shown in chapter 2, the experimental superradiant data most closely compares to the summation of these two patterns.

### 5.3 The CARM Interaction Utilizing Group II Orbits

A similar series of parameter scans were performed for the CARM utilizing the group II orbits to spin up the beam. Scans of the radiated power versus axial and wiggler fields separately are shown in figures 5-8 and 5-9 respectively. The numerical simulation of power output versus  $z$  for the group II orbit CARM, based upon the trajectory analysis of figure 3-10 (parameters  $B_z=6.1$  kG,  $B_w=490$  g,

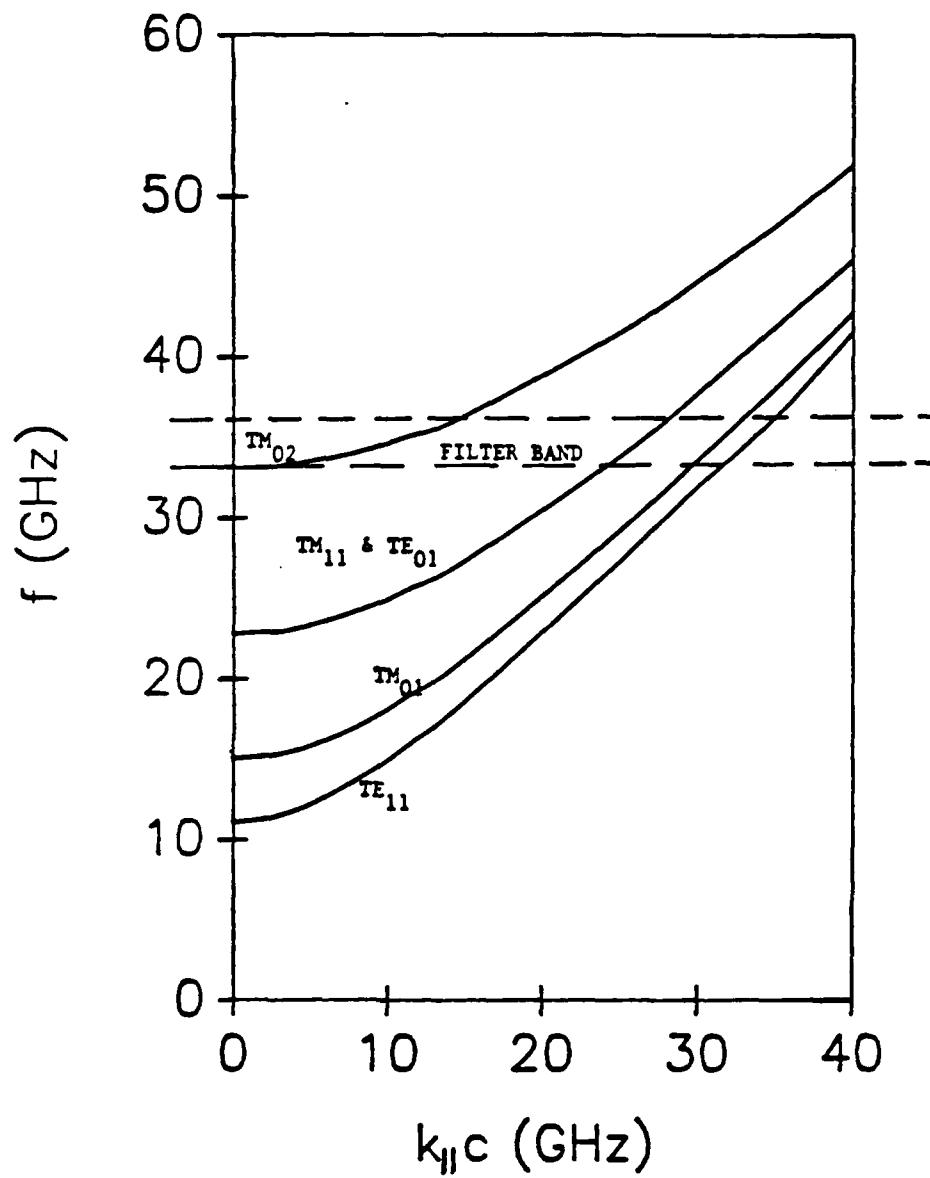


Figure 5-5: Higher order waveguide modes available for coupling to the beam.

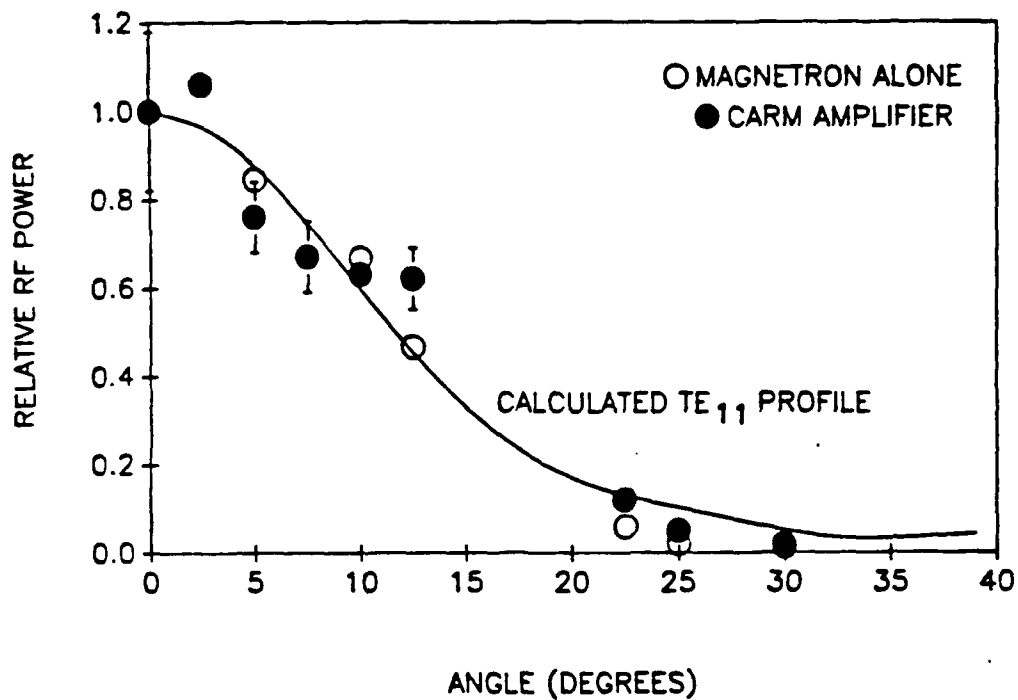
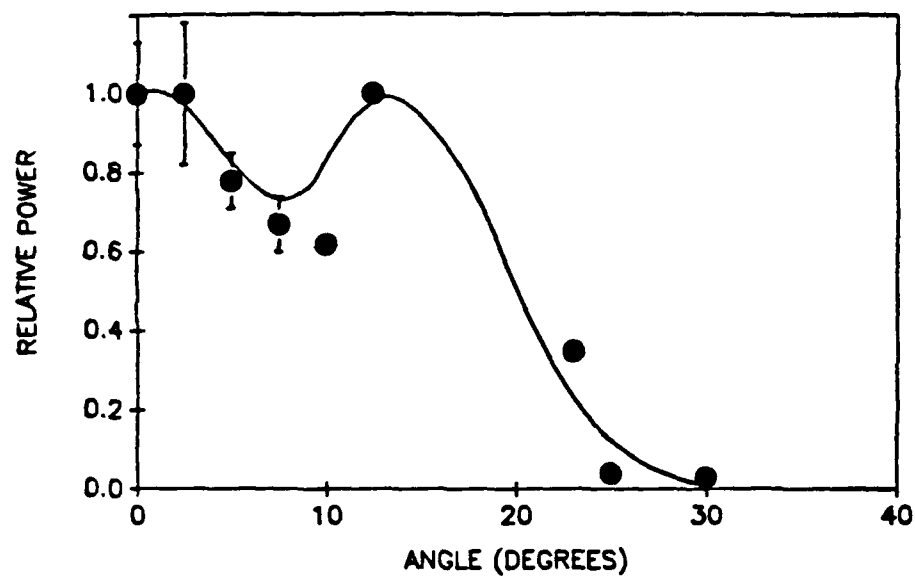
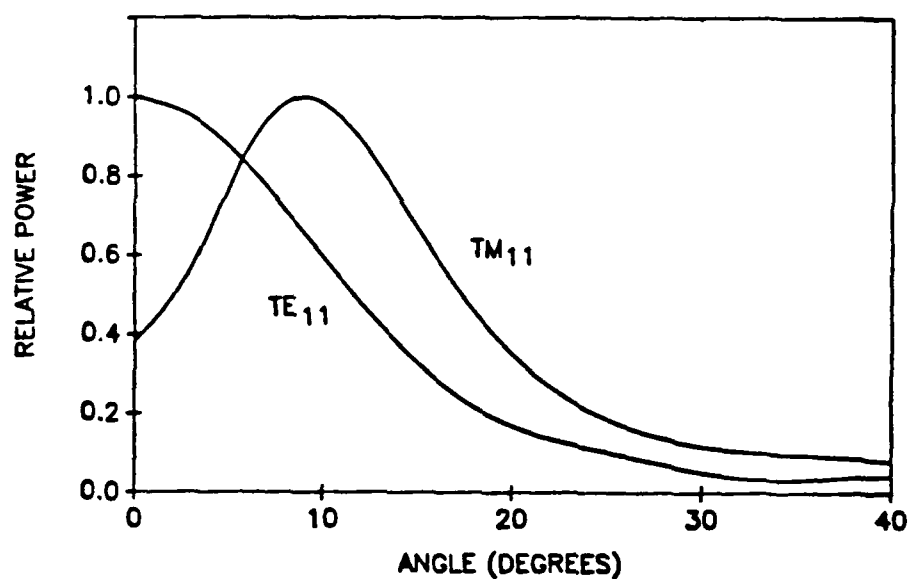


Figure 5-6: Angular scan of amplifier mode radiation. Open circles denote magnetron  $TE_{11}$  mode alone, closed circles are the experimental amplifier data, and the solid line represents the calculated horn pattern for the  $TE_{11}$  mode.



a)

# CALCULATED MODE PROFILES



b)

Figure 5-7: a) Measured radiation pattern during superradiant operation of the CARM. b) Calculated angular profiles for the  $TE_{11}$  and  $TM_{11}$  modes.



$\gamma=3.94$ ,  $\alpha=.30$ ,  $i=128$  A,  $\langle r_L \rangle=0.42$  cm and  $\langle r_g \rangle=0.16$  cm), is shown in figure 5-10. The peak output power is 8.7 MW and the growth rate is 62 dB/m. As in the previous section, a comparison is made between the experimental points and the cold and warm beam. Again, the experimental data has a growth rate similar to the cold beam case (figure 5-10(a)) and saturates an order of magnitude earlier than the simulated cold beam interaction. When compared to the warm beam parameters as generated by the trajectory code (figure 5-10(b)) the difference between the experimental and simulated data drastically decreases.

In chapter 2, mention was made of the necessity to construct a transmitting horn window that had a minimum of reflectivity in order to insure that the CARM device acted a single-pass amplifier as intended and not as an oscillator. Figure 5-11 shows the power as a function of interaction length for the group II CARM and utilizing a plexiglass window. The large growth rate (91 dB/m) is attributed to multipassing in the interaction region. The pulse length of the beam limits the number of passes to two at most.

The single pass growth rate can be calculated as follows assuming 100% reflection at the launcher region. For two passes, the output power  $P_{out}$  is

$$P_{out} = P_{in}(1 - R)[e^{\Gamma L} + Re^{2\Gamma L}] \quad (5.1)$$

where  $R$  is the window power reflection coefficient,  $\Gamma$  is the single pass growth rate, and  $L$  is the length of the system. For the TPX window used in the experiment,  $R \approx 10^{-4}$ ,  $Re^{2\Gamma L} \ll 1$  and thus

$$P_{out} \approx P_{in}e^{\Gamma L}. \quad (5.2)$$

For the plexiglass window with 10% reflectivity,  $Re^{2\Gamma L} \gg e^{\Gamma L}$  and equation 5.1 can be written as

$$P_{out} \approx P_{in}(1 - R)Re^{2\Gamma L}. \quad (5.3)$$

Therefore the slope of the power versus interaction length curve shown in figure 5-11 is approximately  $2\Gamma$ . The single pass gain is therefore  $\approx 45$  dB/m which compares favorably with that for the TPX window.

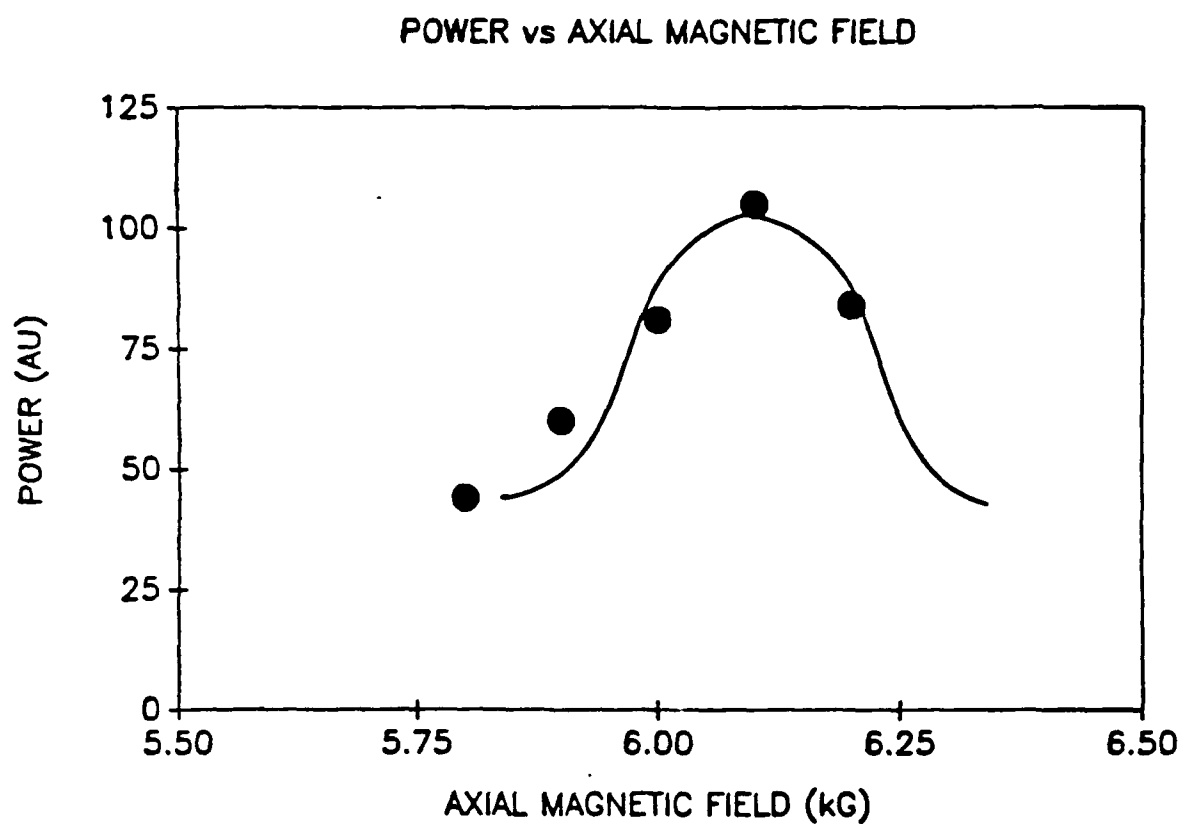


Figure 5-8: CARM power as a function of the axial magnetic field for the group II orbit CARM.  $\gamma=3.94$ ,  $B_w=490$  gauss, and  $I=128$  A.

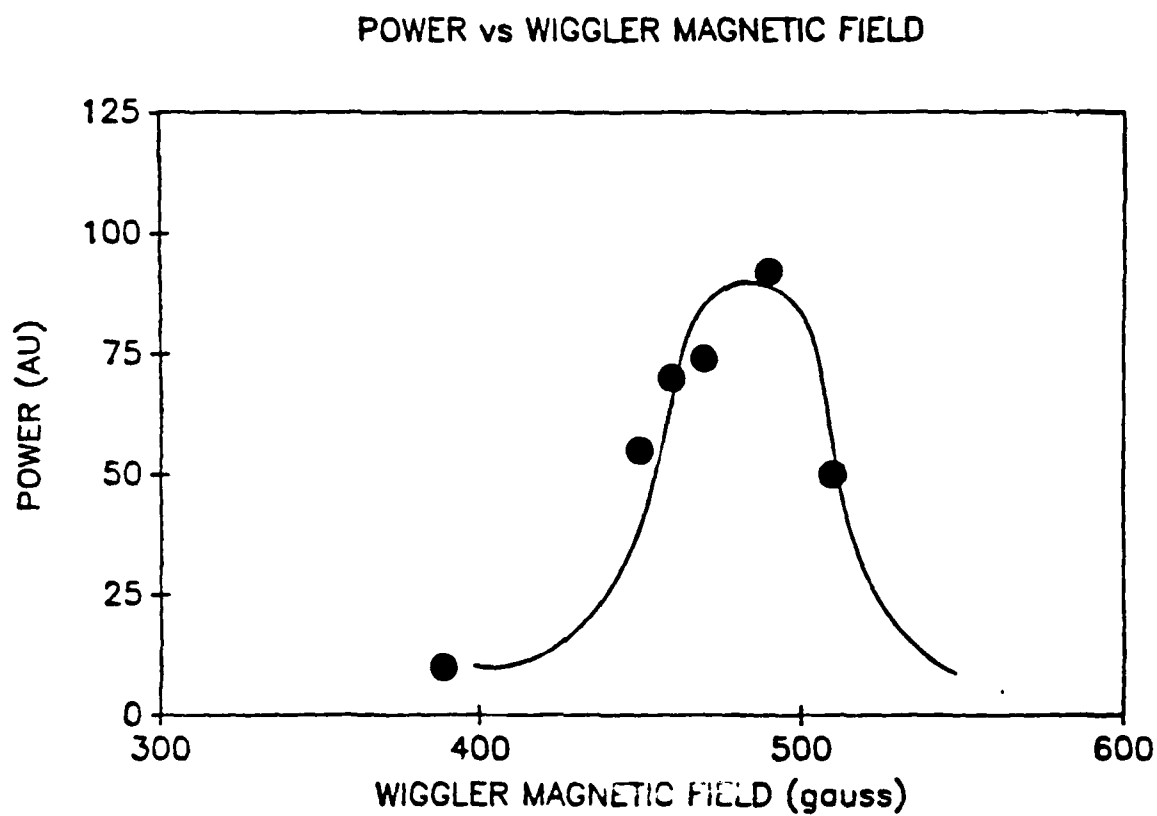


Figure 5-9: Power versus wiggler strength for the group II orbit CARM.  $\gamma=3.94$ ,  $B_z=6.1$  kG, and  $I=128$  A.

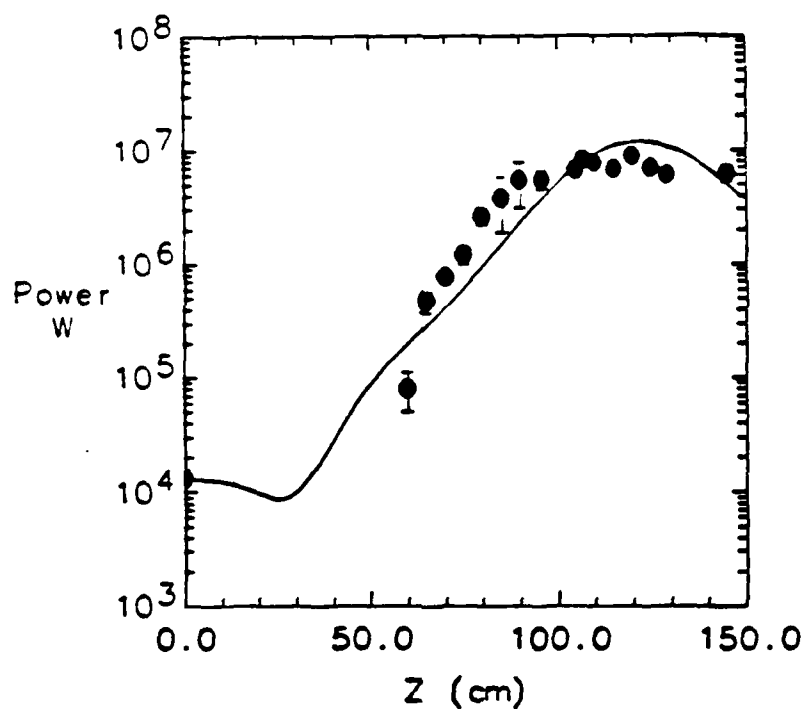
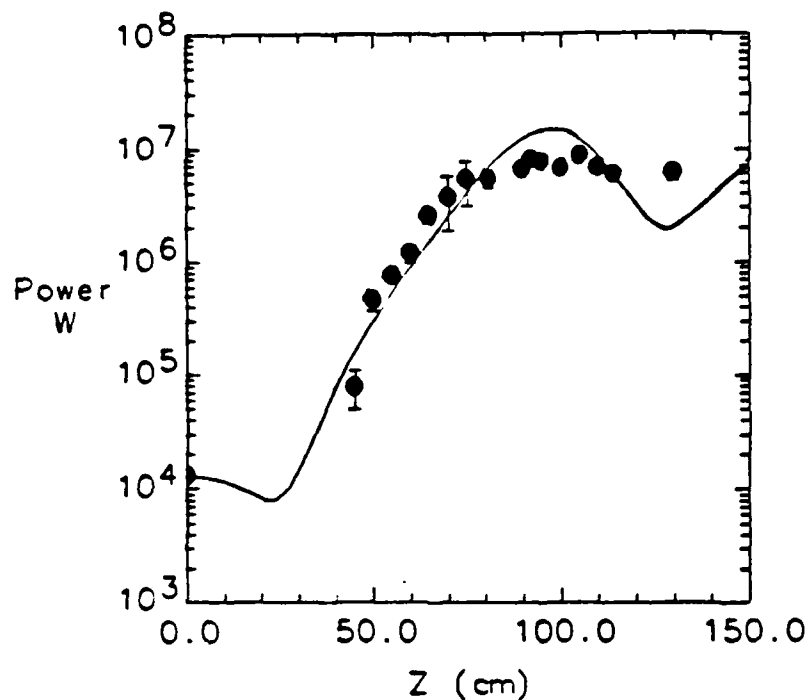


Figure 5-10: Comparison of numerical simulations and experimental data for the group II CARM (a) comparison to the cold beam simulation (b) comparison to the warm beam simulation with  $\Delta\gamma_{||}/\gamma_{||}=4.4\%$ . Experimental parameters are those shown in table 5.1.

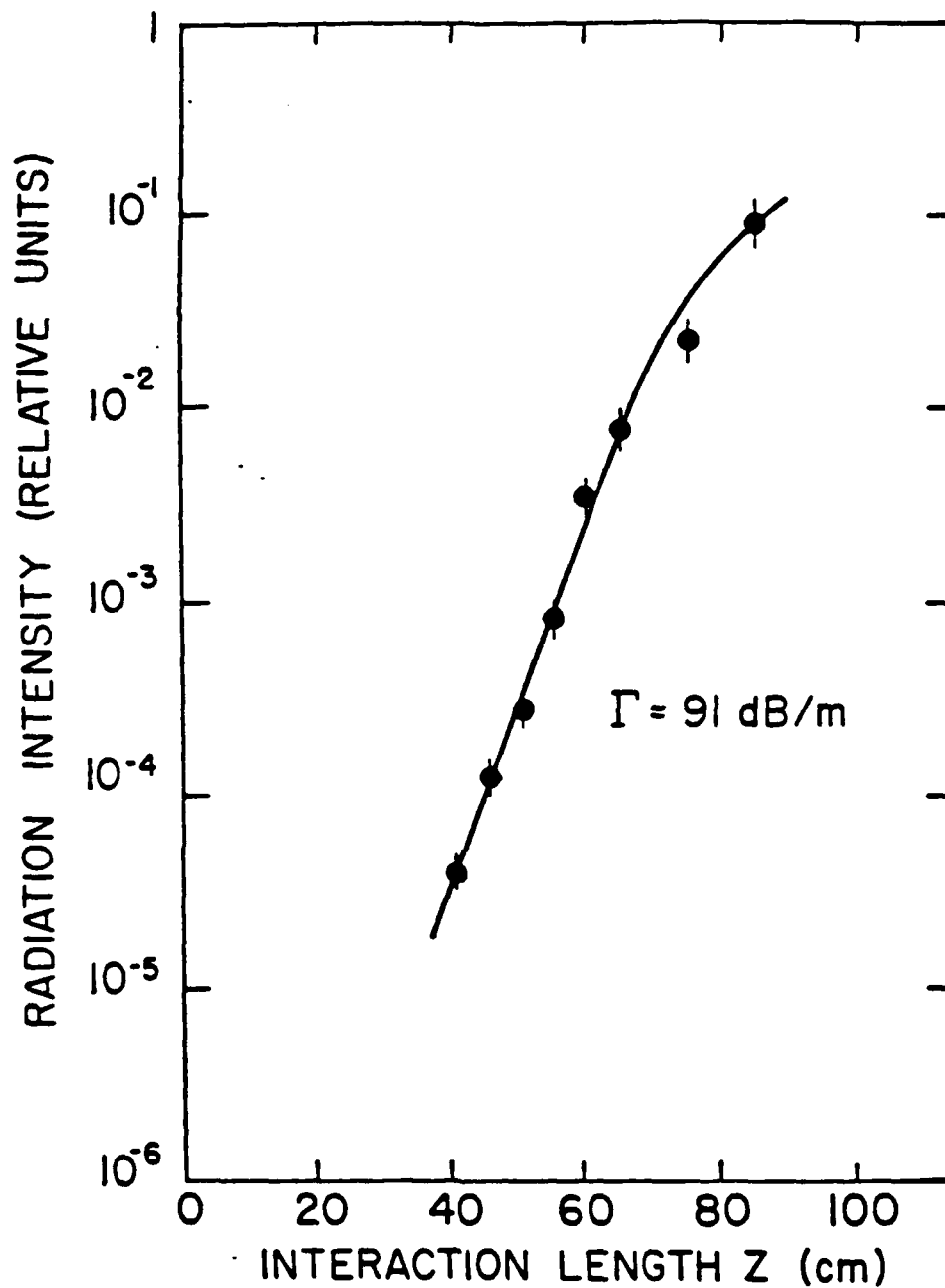


Figure 5-11: Power versus interaction length for the group II orbit CARM operating in the superradiant mode, utilizing a plexiglass window. The single pass gain is calculated to be approximately 45 dB/m.

# Chapter 6

## Conclusion and Summary

This work reports the first successful operation of a cyclotron autoresonance maser single pass amplifier. This initial device operates at a 6% efficiency and with a gain of nearly 30 dB over an input signal of 17 kW. The resulting power from this experiment reaches a maximum of 12.2 MW, a linear growth rate of 50 dB/m, and a pulse duration of 30 ns when the group I orbits are used to spin up the beam. A maximum power of 8.7 MW and a linear growth rate of 62 dB/m is measured when the group II orbits are used. The device is also operated as a superradiant amplifier in which the group I CARM achieved a growth rate of 42 dB/m and the group II CARM achieved a growth rate of 45 dB/m. Power saturation did not occur in either case. In the group I CARM, an angular scan of the emitted radiation shows evidence of interaction with both the  $TE_{11}$  and  $TM_{11}$  modes.

The measurements of the rf power produced by the CARM device show that (1) the power is independent of the method used to spin up the beam, (2) multiple modes can be excited in the superradiant mode, (3) mode suppression occurs in the amplifier case where a high power input signal is used, and 4) as predicted by numerical simulations, energy spreads of the order of 5% significantly degrade efficiency.

The power generated by the device is a function of the beam current, perpendicular velocity, energy and energy spread, waveguide mode, and axial magnetic field. The method of imparting perpendicular velocity to the beam is shown to be

immaterial in so far as spinning up the beam in either group I or II orbits results in a particular set of beam parameters. In this experiment, the experience of utilizing the group I orbits was preferable in that the beam deviated less from the waveguide axis and betatron oscillations in the wiggler region were avoided.

The excitation of multiple waveguide modes is seen in the case of superradiant amplification. Two modes were detected in the experiment: the designed  $TE_{11}$  mode and a side lobe corresponding to the  $TM_{11}$  mode. The theoretical work is incomplete as to the coupling of  $TE$  and  $TM$  modes in the CARM interaction. If each mode is treated separately, present theory predicts rapid growth (within the space of the device) only of the  $TE_{11}$  mode.

In the presence of a high power driver, the multimoding effect is not apparent. The input signal of more than 10 kW suppresses all other modes and the CARM interaction results in the amplification of only the  $TE_{11}$  mode. When a proper analysis is made of the dynamics of the electron beam through the wiggler and into the CARM region, and when the results of the beam analysis are used as input into the CARM simulation, an accurate prediction can be made of the CARM experimental results.

In the course of the experiment several improvements have been made to existing numerical simulations and experimental equipment. First, simulations of the beam dynamics and of the CARM interaction have significantly improved both in terms of modeling the physics and in presentation of results. This work has manually connected the simulations of beam dynamics to the simulations of the CARM interaction with reasonable success as shown by the experimental and simulated power versus  $z$  scans. It has used an improved version of the CARM code that takes into account the effects of finite Larmor radius and offset guiding center into the calculation of the CARM interaction. Secondly, equipment improvements have been made. A microwave input coupler was built that could deliver up to 92% of the power of the magnetron to the CARM region. The diodes used were able to withstand thousands of shots without degrading. An anechoic chamber was constructed that effectively attenuated the multimewatt power output to reasonable levels for detection. The group I and II wigglers were sturdily constructed in a manner

that eliminated harmonic and termination effects. The experimental device was as simplified as possible in order to be able to study the CARM interaction as much as possible.

There are things that can be improved in future CARM experiments. The first is the mating of the trajectory code and the CARM interaction code. While having them as distinct entities allows for the piecemeal analysis of the device and the interaction, mating the two codes could eliminate some of the averaging that must take place to allow the CARM code to use data of the trajectory code. The trajectory code itself does not account for the self electric and magnetic fields of the beam. In the present experiment these are believed to have a small effect, however, the fact that the CARM interaction efficiency is strongly dependent upon beam temperature, calls for greater accuracy in the determination of beam temperature. Second, further efforts should be taken to increase the current emitted by the diode since the efficiency of the interaction is such a strong function of the current. This can be accomplished by a separate 12 kG field over the diode. Action of this sort would also benefit the attempt to decrease beam temperature. Third, accurate and redundant methods must be emplaced for calibration of the attenuation between the output of the device and the detector.

The motivation for construction of the CARM operating at 35 GHz, besides the fact that it had not been successfully accomplished previously, is the fact of the large Doppler upshift in the frequency as compared to the gyrotron. The alternative source of 35 GHz radiation could easily be a free electron laser, however, the CARM eliminates the need for a wiggler in the interaction region and can be considered a more simple device. The growth rate can be increased by operating the device as an oscillator resulting in a source of rf power that can occupy a relatively small space.

The CARM as a source of rf power has several applications. This work has proven the CARM to be an effective alternative to the free electron laser and the gyrotron as a source of rf power. The device has the potential to be a power source for tokamak plasma heating. The Naval Research Laboratory's 35 GHz gyrotron, at an output power of 340 kW, has been used for this purpose [18]. The 30-fold



increase in power of the device in this experiment over the NRL gyrotron is a step in the this direction. The CARM can also be a power source for experimental high gradient linear accelerators that may achieve up to 500 MeV/m. When used as the initial stage of a two beam accelerator (TBA), where the CARM interaction provides high power to accelerate a beam that drives a free electron laser, the design requirements of the TBA can be reduced since only a guide field is needed in the CARM interaction.

The CARM also has the potential to be a source of a high power signal for  $K_a$  band radar and communications. Atmospheric absorption is minimal at 35, 94, 220, and 325 GHz, all of which are within the range of a CARM device. The large bandwidth of the CARM would enhance the resistance to interference or jamming and permit high range resolution [18]. The key advantage of the CARM over the gyrotron is its ability to generate radiation at a particular frequency at a lower magnetic field than the gyrotron which, at subcentimeter wavelengths, requires superconducting magnets and high field strengths.

This work shows that the CARM is an effective alternative to the free electron laser and gyrotron for millimeter wavelength radiation. A simple, sturdy, high power device has been constructed in this experiment and any application of the CARM to those uses mentioned above would be significant. Still, it is best to expect the unexpected in the search for new uses of emerging technologies.

# Bibliography

- [1] A. DiRienzo, G. Bekefi, C. Leibovitch, and B. Danly. Cyclotron autoresonance maser experiments. In *FEL '89 Conference Digest*, pages 175–176, August 1989.
- [2] G. Bekefi, A. C. DiRienzo, C. Leibovitch, and B. G. Danly. 35 ghz cyclotron autoresonance maser amplifier. *Applied Physics Letters*, 54(14):1302–1304, April 1989.
- [3] A. C. DiRienzo, G. Bekefi, C. Leibovitch, and B. G. Danly. Radiation measurements from a 35 ghz cyclotron autoresonance maser (CARM) amplifier. In *Proceedings of the International Society for Optical Engineering*, pages 238–242, January 1989.
- [4] G. Bekefi, A. C. DiRienzo, C. Leibovitch, and B. G. Danly. A 35 ghz cyclotron autoresonance maser amplifier. *Nuclear Instruments and Methods in Physics Research*, A285:230–232, 1989.
- [5] A. C. DiRienzo and G. Bekefi. The M.I.T. 35 ghz cyclotron autoresonance maser (CARM) amplifier. In *Proceedings of the international society for optical engineering*, pages 209–214, january 1990.
- [6] B. G. Danly, K. D. Pendergast, and R. J. Temkin. Theory and design of a high power, 140 GHz CARM amplifier. *Proceedings S.P.I.E.*, 873, January 1988.
- [7] B. G. Danly, K. D. Pendergast, and R. J. Temkin. Millimeter wave CARM amplifier experiment. In *15th International Conference on Infrared and Millimeter Waves*, Honolulu HI, December 1988.

- [8] R. M. Gilgenbach, J. G. Wang, et al. Frequency tunable, high power microwave emission from cyclotron autoresonance maser oscillators driven by microsecond, intense electron beams. In *FEL '89 Conference Digest*, pages 54-55, August 1989.
- [9] V. L. Bratman, G. G. Denisov, N. S. Ginzburg, and M. I. Petelin. Fel's with bragg reflection resonators: cyclotron autoresonance masers versus ubitrons. *IEEE Journal of Quantum Electronics*, QE-19(3):282-296, March 1983.
- [10] V. L. Bratman, N. S. Ginzburg, G. S. Nusinovich, M. I. Petelin, and P. S. Strelkov. Relativistic gyrotrons and cyclotron autoresonance masers. *International Journal of Electronics*, 51:541-567, 1981.
- [11] I. E. Botvinnik, V. L. Bratman, A. B. Volkov, et al. Free electron masers with distributed feedback. *Pis'ma Zh. Eksp. Teor. Fiz.*, 35:418-420, 1982.
- [12] I. E. Botvinnik, V. L. Bratman, et al. The cyclotron autoresonance maser operated at a wavelength 2.4 mm. *Pis'ma Zh. Eksp. Teor. Fiz.*, 8:1376-1378, 1982.
- [13] N. S. Ginzburg, I. G. Zarnitsyna, and G. S. Nusinovich. Theory of cyclotron resonance maser amplifiers. *Radiophysics Quantum Electronics*, 24:331-338, 1981.
- [14] A. T. Lin. Doppler shift dominated cyclotron masers. *International Journal of Electronics*, 57:1097-1108, 1984.
- [15] A. W. Fliflet. Linear and nonlinear theory of the Doppler shifted cyclotron resonance maser based on TE and TM waveguide modes. *International Journal of Electronics*, 61:1049-1080, 1986.
- [16] J. L. Hirshfield, K. R. Chu, and S. Kainer. Frequency upshift for cyclotron wave instability on a relativistic electron beam. *Applied Physics Letters*, 33(10):847-848, November 1978.

- [17] R. Shefer. *Millimeter wave emission from an intense relativistic electron beam in a rippled magnetic field*. PhD thesis, M.I.T., June 1981.
- [18] P. Sprangle and T. Coffey. New sources of high power coherent radiation. *Physics Today*, 44-51, march 1984.
- [19] A. T. Lin, K. R. Chu, and A. Bromborsky. The stability and tunability of a carm amplifier. *IEEE Transactions on Electron Devices*, ED-34(12):2621-2624, December 1987.
- [20] J. K. Lee, W. D. Bard, S. C. Chiu, R. C. Davidson, and R. R. Goforth. Self-consistent nonlinear evolution of the cyclotron autoresonance maser. *Physics of Fluids*, 31(6):1824-1826, June 1988.
- [21] A. T. Lin and C. C. Lin. Competition of electron cyclotron maser and free electron laser modes with combined solenoidal and longitudinal wiggler fields. *Physics of Fluids*, 29(5):1348-1351, May 1986.
- [22] P. H. Yoon and R. C. Davidson. Closed-form analytical model of the electron whistler and cyclotron maser instabilities in relativistic plasma with arbitrary energy anisotropy. *Physical Review A*, 35(6):2619-2639, March 1987.
- [23] P. Sprangle, C. M. Tang, and P. Serafim. Induced resonance electron cyclotron quasi-optical maser in an open resonator. *Applied Physics Letters*, 49(18):1154-1156, November 1986.
- [24] A. Fruchtman. *A comparative study of the gyrotron, the free electron laser and the wiggler free free electron laser*. Technical Report WIS-87/54, Weizmann Institute of Science, July 1987.
- [25] R. C. Davidson. *Physics of Nonneutral Plasmas II*. Technical Report, M.I.T. Plasma Fusion Center, 1989.
- [26] K. R. Chu, A. T. Drobot, H. H. Szu, and P. Sprangle. Theory and simulation of the gyrotron travelling wave amplifier operating at cyclotron harmonics. *IEEE Transactions on Microwave Theory and Technique*, 28:313-317, 1980.

- [27] K. R. Chen, J. M. Dawson, A. T. Lin, and T. Katsouleas. Unified theory and comparative study of carms, icls and fels. 1990. Draft Report.
- [28] R. C. Davidson and P. H. Yoon. Stabilization of the cyclotron autoresonance maser (CARM) instability by axial momentum spread. *Physical Review A*, 39(5), March 1989.
- [29] K. D. Pendegast, B. G. Danly, R. J. Temkin, and J. S. Wurtele. Self consistent simulation of cyclotron autoresonance maser amplifiers. *IEEE Transactions on Plasma Science*, April 1988.
- [30] C. Chen. Private Communication.
- [31] R. H. Jackson et al. Design and operation of a collective millimeter wave free electron laser. 1981. Draft Report.
- [32] R. B. Miller. *An introduction to the physics of intense charge particle beams*. Plenum Press, 1982.
- [33] D. Prosnitz and E. T. Scharlemann. *Beam quality definitions*. Technical Report ATA Note 229, Lawrence Livermore National Laboratory, February 1984.
- [34] E. T. Scharlemann. *The phase space accepted by the ELF emittance selector*. Technical Report ELF Note 90, Lawrence Livermore National Laboratory, February 1984.
- [35] C. G. Montgomery, R. H. Dicke, and eds. E. M. Purcell. *Principles of Microwave Circuits*. McGraw-Hill Book Company, 1948.
- [36] ed. Samuel Silver. *Microwave Antenna Theory and Design*. McGraw Hill Book Company, 1949.
- [37] Arthur C. Ludwig. Radiation pattern synthesis for circular aperture horn antennas. *IEEE Transactions on Antenna Propagation*, AP-14:434-440, July 1966.

- [38] J. M. Buzzi, K. Felch, and L. Vallier. *Etude du champ magnetique produit par une double helice*. Technical Report , Laboratoire de Physique des Milieux Ionises, Ecole Polytechnique, France, 1980.
- [39] J. Fajans. *Radiation measurements of an intermediate energy free electron laser*. PhD thesis, M.I.T., august 1985.
- [40] M. Abramowitz and I. Stegun. *Handbook of Mathematical Functions*. Dover Publications, 1964.
- [41] K. D. Pendergast. Private Communication.
- [42] D. A. Kirkpatrick. *Experimantal observations of millimeter and submillimeter wave emission from a free electron laser*. PhD thesis, M.I.T., January 1988.
- [43] L. Friedland. Electron beam dynamics in combined guide and pump magnetic fields for free electron laser applications. *Physics of Fluids*, 23(12):2376-2382, December 1980.
- [44] Paul Diamant. Electron orbits and stability in realizable and unrealizable wigglers for free electron lasers. *Physical Review A*, 23(5):2537-2552, May 1981.
- [45] J. Fajans, D. A. Kirkpatrick, and G. Bekefi. Off axis electron orbits in realistic helical wigglers for free electron laser applications. *Physical Review A*, 32(6):3448-3453, December 1985.
- [46] J. Fajans. End effects of a bifilar magnetic wiggler. *Journal of Applied Physics*, 55(1):43-50, January 1984.
- [47] K. R. Chu and Anthony T. Lin. Gain and bandwidth of the gyro-TWT and CARM amplifiers. *IEEE Transactions on Plasma Science*, 16(2):90-104, April 1988.
- [48] R. J. Briggs. *Electron Stream Interaction with Plasma*. M.I.T. Press, 1964. Chapters 2 and 3.

[49] A. Bers. Waves and instabilities. 1988. Class notes.

[50] Y. Y. Lau. Simple macroscopic theory of cyclotron maser instabilities. *IEEE Transactions on Electronic Devices*, 29:320–335, 1982.